EXPERIMENTAL AND THEORETICAL STUDIES ON ELECTRON-BEAM FOCUSING USING ACTIVE PLASMA LENSES

Dissertation Zur Erlangung der Würde des Doktors der Naturwissenschaften des

Fachbereichs Physik, der Fakultät für Mathematik, Informatik und Naturwissenschaften,
der Universität Hamburg

Vorgelegt von
Jan-Hendrik Röckemann (geb. Erbe)
aus Bad Oldesloe

Januar 2020

Gutachter der Dissertation:
Dr. Jens Osterhoff
Prof. Dr. Brian Foster

Zusammensetzung der Prüfungskommision:
Prof. Dr. Brian Foster
Prof. Dr. Dieter Horns
Prof. Dr. Gudrid Moortgat-Pick
Dr. Jens Osterhoff
Dr. Klaus Flöttmann

Vorsitzender der Prüfungskommision:
Prof. Dr. Dieter Horns

Datum der Disputation:
25.02.2020

Vorsitzender Fach-Promotionsausschusses PHYSIK:	Prof. Dr. Günter H. W. Sigl
Leiter des Fachbereichs PHYSIK:	Prof. Dr. Wolfgang Hansen
Dekan der Fakultät MIN:	Prof. Dr. Heinrich Graener

ABSTRACT

This work assesses the potential of active plasma lenses to deliver stable, quality-preserving focusing for high energy electron beams. It first provides a theoretical framework for understanding the focusing mechanisms of active plasma lenses. It then presents experimental results of direct electric field measurements inside of an active plasma lens as well as beam emittance measurements after passage through it.

Recent advances in particle accelerator design aim for a paradigm shift away from cavity based accelerator modules towards smaller structures such as plasma-based accelerators allowing for orders of magnitude higher electric field gradients. These novel accelerator designs share a challenge intrinsic to their compact size: The capturing of beams after acceleration. Since beams have to be matched to the accelerating plasma wave, they are typically on the order of a few micrometer wide transversely. In combination with a common emittance of 0.5 mm mrad, the beams are released with a relatively high divergence (~ mrad). Additionally, the energy spread of these beams typically lies on the percent-level. Beams with the combination of high divergence and energy spread will suffer loss of beam quality in a drift and in beam optics up to the point where the divergence is eliminated. So there is high demand for a capturing beam optic that mitigates this deteriorating effect. The active plasma lens provides a solution to this problem by focusing rapidly and azimuthally symmetric. This is a significant advantage over other focusing beam optics since the beam quality can be preserved in both horizontal and vertical direction simultaneously.

The experimental results presented in this work show that active plasma lenses are capable of delivering stable, tunable, kT/m focusing gradients, an order of magnitude stronger than conventional electromagnetic quadrupole magnets. They also confirm the theoretical predictions in terms of nonlinearity and emittance degradation. They constitute a combination of magnetic field and beam emittance measurements in an active plasma lens that provide a gauge for the theoretical framework. Using this framework, the path towards beam quality preserving, high-gradient and tunable active plasma lenses for applications is shown.

ZUSAMMENFASSUNG

Die vorliegende Arbeit befasst sich mit der Frage, ob aktive Plasmalinsen verlässlich Strahlqualitäterhaltende Fokussierung für Elektronenstrahlen liefern können. Zuerst führt sie einen theoretischen Rahmen ein, der es ermöglicht den Fokussiermechanismus von aktiven Plasmalinsen zu verstehen. Anschließend werden experimentelle Ergebnisse einer direkten Messung sowohl des elektrischen Feldes in einer aktiven Plasmalinse als auch der Strahlemittanz nach der Fokussierung mit derselben vorgestellt.

Die jüngeren Entwicklungen auf dem Feld der Teilchenbeschleuniger zielen auf einen Paradigmenwechsel hin, weg von Hohlraumresonatorbasierten Beschleunigerelementen hin zu kleineren Strukturen, die höhere Gradienten des elektrischen Feldes erlauben. Diese neuen Beschleunigerdesigns verbindet eine Herausforderung, die mit ihrer Größe einhergeht: Das Einfangen der Strahlen nach der Beschleunigung. Da die Teilchenstrahlen um effektiv beschleunigt werden zu können in ihrer Größe der beschleunigenden Plasmawelle angepasst sein müssen, ist ihre transversale Ausdehnung typischerweise wenige Mikrometer. Dies zusammen mit einer typischen Emittanz von 0.5 mm mrad führt dazu, dass die Strahlen mit einer relativ hohen Divergenz das Plasma verlassen (~ mrad). Zusätzlich haben diese Strahlen typischerweise eine Energieunschärfe im Prozentbereich. Strahlen mit dieser Kombination erleiden einen Qualitätsverlust während der Driftstrecke und in Strahloptiken nach der Beschleunigung, der erst kompensiert wird, wenn die Divergenz eliminiert wird. Aus diesem Grund werden Einfangoptiken benötigt, die diesen nachteiligen Effekt abschwächen können. Aktive Plasmalinsen bieten eine Lösung für dieses Problem, da sie schnell und rotationssymmetrisch fokussieren können. Dies stellt einen deutlichen Vorteil gegenüber anderen Fokussieroptiken dar, da die Strahlqualität so in horizontaler und vertikaler Richtung gleichzeitig erhalten werden kann.

Die experimentellen Ergebnisse zeigen, dass Plasmalinsen stabil und zuverlässig einstellbare Fokussiergradienten im Bereich von kT/m liefern können, eine Größenordnung stärker als elektromagnetische Quadrupollinsen ist. Die Messungen der Strahlemittanz stimmen ebenfalls sehr gut mit den theoretischen Vorhersagen der Nichtlinearität der Plasmalinse überein. Die Ergebnisse stellen eine Kombination aus direkter Feldmessung und Emittanzmessung des passierenden Elektronenstrahls dar, was eine Überprüfung der vorgestellten Theorie zu Plasmalinsen ermöglicht. Mit Hilfe dieser Theorie wird anschließend der Pfad zu Strahlqualitätserhaltenden, starken und einstellbaren Plasmalinsen für Anwendungen aufgezeigt.

CONTENTS

INTRODUCTION

Many of the rapid advances of the natural sciences during the last century have been fueled by ultra-relativistic particle beams from particle accelerators. Their development went along with leaps in the understanding of the building blocks of the universe, the rise of the standard model of particle theory [1]. Today, electron beams with small energy spreads are used routinely to produce X-ray pulses for medical applications such as tomography of human tissue [2, 3] or structural analysis of complex molecules in biochemstry [4, 5]. Using these electron beams to drive ultra-fast free-electron-laser sources [6] will allow time-resolved single-shot single-molecule imaging [7, 8].

Conventional particle accelerators are based on radio-frequency resonators [9] which are limited in their electric-field strength by material breakdown to $\sim 100\,\mathrm{MV/m}$. With applications in need of particle energies ranging from the several hundred MeV to TeV range, this technique struggles to deliver beams in a facility of reasonable cost and size. A novel particle accelerator scheme involving large-amplitude plasma waves promises a large reduction in the investment necessary for theses facilities due to their very high accelerating electric field ($\sim$100 GV/m). These plasma waves are driven either by particle beams in the case of beam driven wakefield acceleration (PWFAs) [10] or intense laser pulses in the case of laser-driven wakefield acceleration (LWFAs) [11].

While plasma-based acceleration schemes are capable of delivering outstanding peak currents, low transverse emittance [12, 13], and femtosecond pulse length, they lag behind in shot-to-shot stability as well as repetition rate. Another drawback of these plasma-based schemes is the fact that beams are released highly divergent after acceleration ($\sim$ mrad) and with a relatively high energy spread($\sim$10%), leading to chromatic emittance growth in the drift following the accelerator [14]. In order to preserve the low emittance, strong focusing immediately behind the accelerating structure is needed. Active plasma lenses (APLs) have the potential to be a key technology in this. They can focus charged particle beams azimuthally symmetrically with high strength (kT/m), setting them apart from conventional beam-optics elements such as quadrupole magnets (QMs) and solenoid magnets. Thus they are a prime candidate for the capturing of beams accelerated in plasma-based accelerators (PBAs).

An APL has recently been used to focus an electron beam from an LWFA and couple it into a second, independent LWFA stage [15]. This shows that the APL is capable of focusing highly divergent relativistic electron beams with a significant energy spread within cm distances. It represents a significant step towards PBAs for applications in photon science such as free-electron lasers (FELs).

This work aims at probing the APL's capability of delivering reliable focusing while preserving beam quality. This task is more challenging in APLs than in conventional beam optics. Owing to the small size of the structure as well as the nature of the plasma discharge, no Hall probes can be inserted safely into the plasma channel, preventing direct magnetic-field quality measurements. A well-studied and reliable beam has to be used in order to gauge the APL's quality by letting the beam interact with the APL and subsequently measuring the effect on the beam. This is discussed in Sections 2 and 3.

It is crucial for any application of the APL to ensure that the emittance of beams traversing the APL is preserved. This work offers a comprehensive theoretical description followed by the analysis of experimental campaigns aimed at probing APLs for their capabilities regarding both delivering high focusing gradients as well as preserving beam quality.

1

THEORETICAL FOUNDATIONS

An azimuthally symmetric plasma channel conducting a high current density can be used to focus highly relativistic charged-particle beams. This chapter introduces the theoretical framework that is necessary to understand this process and the following chapters.

The first section provides a formalism for describing the motion of charged-particle beams. It introduces commonly used beam optics elements and expands the list by the aforementioned plasma-channel-based focusing device called an active plasma lens (APL).

The second section gives an introduction to the properties of plasma. Plasma created in high-voltage discharges are of particular interest for the functionality of APLs. It also provides a brief introduction to plasma wakefield acceleration which is a field of particle accelerator physics for which APLs are of particular interest. This is needed for the reader to understand the benefits an APL has over conventional focusing optics when used in combination with a plasma-based accelerator.

1.1 DYNAMICS OF CHARGED-PARTICLE BEAMS

While it is theoretically possible to solve the equations of motion of every single charged particle in an accelerator, it is favorable to define a *beam* as an assembly of particles and treat their collective behavior. In order to form a particle beam an assembly needs to fulfill the condition $\langle p_z \rangle \gg \langle p_{x,y} \rangle$ - the mean forward momentum of a beam is much larger than its transverse momenta. In particle accelerators beams are usually 'bunched' longitudinally. Therefore, a set of particles in the beam that is longitudinally separated from other particle sets is referred to as a *bunch*. This is commonly found in accelerators owing to the alternating nature of the accelerating fields, be it in radio-frequency (RF) based accelerators as well as plasma-based accelerators. The behavior of charged-particle beams is studied in the following.

1.1.1 *Transfer matrix formalism*

The motion of charged particles along an accelerator beam line can be described by a matrix formalism. A detailed description can be found in [16]. The canonical six-dimensional *phase space* for particles in an accelerator is given by the spatial coordinates $\mathbf{x} = (x, y, s)$ and the momenta $\mathbf{p} = (p_x, p_y, p_s)$ spanning a canonical basis $\hat{\mathbf{X}} = (\mathbf{x}, \mathbf{p})$. This is only canonical as long as there is no transverse vector potential in the beam path (e.g. no solenoid field). Fig. 1 shows the definition of the spatial coordinates used above. The phase-space is typically divided into the three planes $x - p_x$, $y - p_y$, and $s - p_s$. It is also common in accelerator physics to consider the geometrical phase space - the so called *trace space* - coordinates in the $x - x'$ and $y - y'$

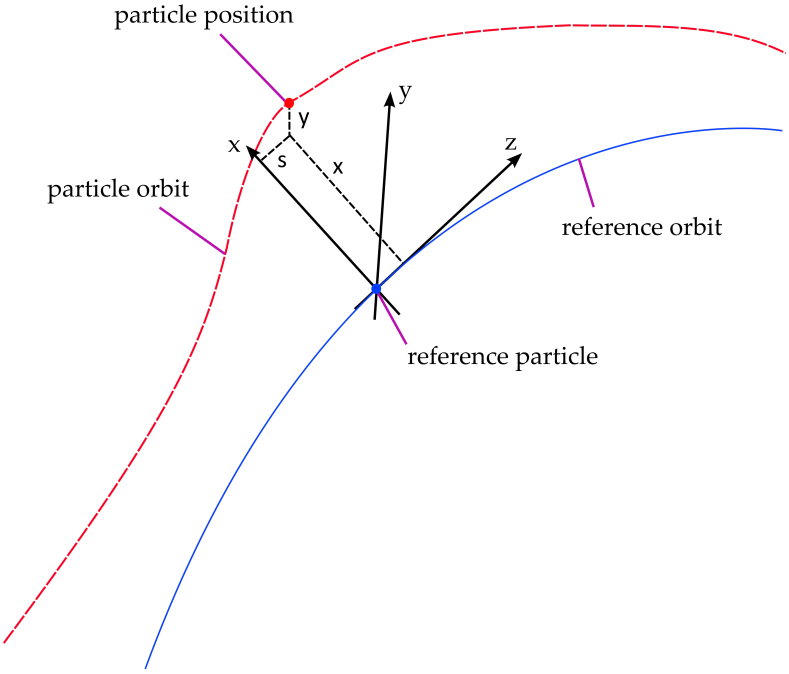

Figure 1: Schematic of the accelerator coordinate system.

planes with the identities $x' = p_x/p_s$ and $y' = p_y/p_s$ instead of the canonical phase space. The longitudinal coordinates of the trace space are defined by the $s - \delta$ plane, with s being the longitudinal displacement and $\delta = \Delta p/p$, the relative momentum deviation from the reference momentum p. They span the trace space vector $\mathbf{X} = (\mathbf{x}, \mathbf{x}')$ with $\mathbf{x}' = (x', y', \delta)$. These coordinates are only canonically conjugated if the momentum is constant.

$$\mathbf{X}(s) = \begin{pmatrix} x \\ x' \\ y \\ y' \\ s \\ \delta \end{pmatrix} \tag{1}$$

All relevant beam manipulation in an accelerator is achieved by using the *Lorentz force*

$$\mathbf{F} = q \cdot (\mathbf{E} + v \times \mathbf{B}), \tag{2}$$

where q is the charge of a particle, v is its velocity, and **E** and **B** are the electric and magnetic field vectors. Beam optics usually rely on the magnetic field while the electric field is used for acceleration. For the acceleration this can readily be seen in Eq.(2) since the magnetic part of the Lorentz force is always perpendicular to the velocity of the charged particle, preventing change of the absolute value of the velocity. On the other hand, the magnetic field is multiplied by velocity which helps when the charged particle is relativistic. The relativistic mass growth of the particle by the relativistic Lorentz factor $\gamma = 1/\sqrt{1-(\frac{v}{c})^2}$ means a greater force has to be exerted to achieve a given change in momentum.

In the following we will concentrate on particle interactions with the magnetic field since this work primarily deals with beam optics for relativistic beams. In order to enable explicit solutions to the particle's equations of motion we assume the beam line consists only of *drift space*, *dipole* and *quadrupole* magnets, and *active plasma lenses* (APLs). In quadrupoles and APLs, the magnetic field depends linearly on the deviation of the particle from the reference orbit. The equations of motion are for this case given by

$$u''(s) + K_u(s) \cdot u(s) = \frac{\delta}{\rho_u(s)}, \tag{3}$$

$\rho_u(s)$ is the bending radius of the reference orbit at s, and $K_u(s)$ is the quadrupole focusing parameter. Here and in the following, $u(s)$ is used as a representation of $x(s)$ or $y(s)$. In the following, we will set the bending radius to infinity. This is done for the sake of the argument convenience here without loss of generality. So Eq. (3) can be simplified to

$$u''(s) + K_u(s) \cdot u(s) = 0. \tag{4}$$

The quadrupole focusing parameter is defined as

$$K_x(s) = -k(s), \tag{5}$$

$$K_y(s) = k(s), \tag{6}$$

and for an APL

$$K_{x,y}(s) = -k(s), \tag{7}$$

with

$$k(s) = \frac{qg(s)}{p}, \tag{8}$$

and $g(s)$ the magnetic-field gradient. Here the *hard-edge model* for magnets is used, which means that the magnetic field starts abruptly at the magnet's front, is constant inside, and ends abruptly at the rear end. Note that the difference between a quadrupole and an APL can be seen in the different definitions of $K_u(s)$ in Eq. (6) and (7). The quadrupole has a focusing effect in one plane and a defocusing one in the other, while the APL is radially symmetric and focuses or defocuses in both planes. Since the focusing mechanism in the focusing plane is the same for APLs and quadrupoles,we will use the term quadrupole-like to include APL fields in all definitions in the following.

u_0 and u'_0 are the initial parameters of the particle trajectory. The solution of Eq. (4) can be written in the form of a matrix equation

$$\begin{pmatrix} x \\ x' \\ y \\ y' \end{pmatrix} = \begin{pmatrix} R_{11} & R_{12} & R_{13} & R_{14} \\ R_{21} & R_{22} & R_{23} & R_{24} \\ R_{31} & R_{32} & R_{33} & R_{34} \\ R_{41} & R_{42} & R_{43} & R_{44} \end{pmatrix} \begin{pmatrix} x_0 \\ x'_0 \\ y_0 \\ y'_0 \end{pmatrix} = \mathbf{R} \begin{pmatrix} x_0 \\ x'_0 \\ y_0 \\ y'_0 \end{pmatrix}. \tag{9}$$

The trace space vector $\mathbf{X}(s)$ can be calculated throughout the entire beamline of an accelerator by multiplying the initial trace space vector $\mathbf{X}(s_0)$ with the transfer matrices $\mathbf{R}_n$ of all n elements in between the two points s_0 and s, i.e.,

$$\mathbf{X}(s) = \mathbf{R}_n \cdot ... \cdot \mathbf{R}_1 \cdot \mathbf{X}(s_0). \tag{10}$$

To find the transfer matrix elements, we need to find the principal solutions to Eq. (3). It simplifies to the form of a harmonic oscillator inside a quadrupole-like field. The principal solutions of this homogeneous equation are

$$\left.\begin{aligned} C_u(s) &= \cos(\sqrt{K_u} s) \\ S_u(s) &= \frac{1}{\sqrt{K_u}} \sin(\sqrt{K_u} s) \end{aligned}\right\} \text{for } K_u > 0$$

$$\left.\begin{aligned} C_u(s) &= \cosh(\sqrt{K_u}s) \\ S_u(s) &= \frac{1}{\sqrt{K_u}}\sinh(\sqrt{K_u}s) \end{aligned}\right\} \text{for } K_u < 0. \tag{11}$$

They are called the sine- and cosine-like solutions. Using a special solution u_i of the inhomogeneous equation we can write the general solution of Eq. (3)

$$u(s) = u_0 C_u(s) + u'_0 S_u(s) + \delta\eta_u(s) \tag{12}$$

$$u'(s) = u_0 C'_u(s) + u'_0 S'_u(s) + \delta\eta'_u(s). \tag{13}$$

We can now replace the elements in Eq.(9) with the appropriate solutions, so that

$$\mathbf{R} = \begin{pmatrix} C_x & S_x & 0 & 0 \\ C'_x & S'_x & 0 & 0 \\ 0 & 0 & C_y & S_y \\ 0 & 0 & C'_y & S'_y \end{pmatrix}. \tag{14}$$

The transfer matrices of elements used in the scope of this work are provided in Sec. 1.1.5.

1.1.2 *Phase space and Courant-Snyder parameters*

Writing a general solution for Eq. (4) yields

$$u(s) = a\sqrt{\beta_u(s)}\cos(\psi_u(s) - \psi_{u,0}), \tag{15}$$

in which the amplitude is given by the constant a and the so-called *beta function* $\beta_u(s)$. a is an invariant of motion under the influence of conservative forces due to *Liouville's theorem* [16]. It is called *Courant-Snyder invariant* and is linked to the beam emittance (cf. Sec. 1.1.3). The beta function fulfills the differential equation

$$\frac{1}{2}\beta_u(s)\beta''_u(s) - \frac{1}{4}\beta'^2_u(s) + K_u(s)\beta^2_u(s) = 1. \tag{16}$$

The arguments of the cosine in Eq. (15) are called phase with a constant term $\psi_{x,0}$ [16] and the phase function is given by

$$\psi_u(s) = \int_0^s \frac{d\hat{s}}{\beta_u(\hat{s})}. \tag{17}$$

Taking Eq. (15) and its derivative we can write

$$a^2 = \hat{\epsilon} = \left(\frac{1 + \beta_u'^2(s)/4}{\beta_u(s)}\right) u^2(s) - \beta_u'(s)x(s)x'(s) + \beta_u(s)u'^2(s), \tag{18}$$

in which $\hat{\epsilon}$ is called the beam emittance (cf. Sec. 1.1.3). Introducing the Courant-Snyder parameters

$$\alpha_u(s) = -\frac{1}{2}\beta_u'(s), \text{and} \tag{19}$$

$$\gamma_u(s) = \frac{1 + \alpha_u^2(s)}{\beta_u(s)} \tag{20}$$

Eq. (18) simplifies to

$$a^2 = \gamma_u(s)u^2(s) + 2\alpha_u(s)u(s)u'(s) + \beta_u(s)u'^2(s), \tag{21}$$

the equation of an ellipse. This ellipse, the *beam ellipse*, is shown in Fig. 2 together with the corresponding Courant-Snyder (also called *Twiss*) parameters. The parameters determine the shape and orientation of the ellipse. A particle following Eq. (15) undergoes so called *betatron motion* and encircles the phase-space ellipse. Since the motion of a particle following Eq. (15) is called *betatron motion*, the Twiss parameters are sometimes referred to as *betatron functions*. The area of this *trace space ellipse* is πa^2. Any particle within the area of the trace space ellipse will always stay inside the ellipse. Thus one can consider the motion of an entire bunch of particles within this trace space area instead of just a single particle. The area will remain constant while the bunch moves through a beamline.

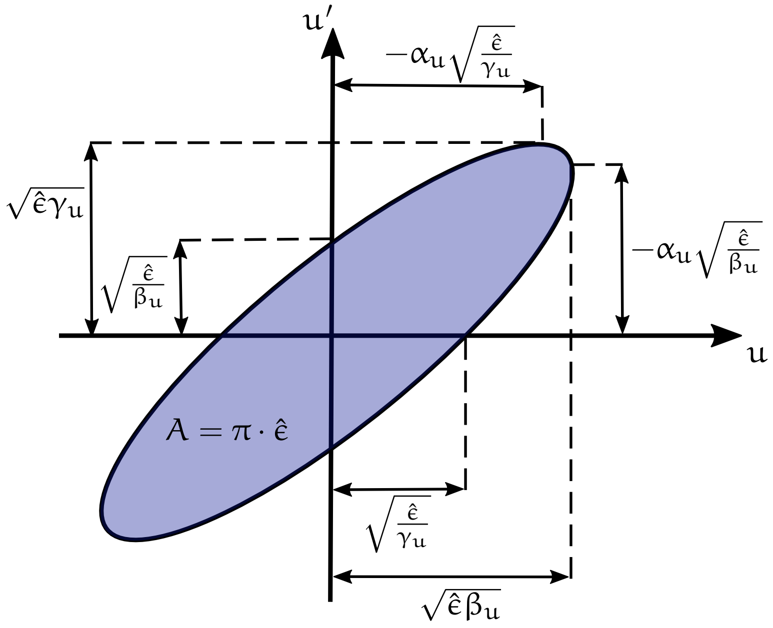

Figure 2: Schematic of the beam ellipse and Courant-Snyder parameters.

1.1.3 *Beam emittance*

The area of the phase-space ellipse of a particle bunch is a crucial figure of merit for charged-particle beams. Divided by π it is referred to as transverse emittance $A/\pi = \hat{\epsilon} = a^2$ (see Fig. 2). Using Eq. (21) we can write

$$\hat{\epsilon}_u = \gamma_u u^2 + 2\alpha_u u u' + \beta_u u'^2. \tag{22}$$

For the emittance definition in accelerator physics the emittance calculation is usually restricted to the high-density region. The most general definition is via the root-mean-square width of a particle distribution $\rho(x, x', y, y')$. Since the transverse emittance is reduced by acceleration because the ratio p_u/p shrinks with increasing p, it is convenient to define the normalized root-mean-square trace-space emittance as

$$\epsilon_u = \sqrt{\langle u^2 \rangle_u \langle \beta^2 \gamma^2 u'^2 \rangle_u - \langle u \beta \gamma u' \rangle_u^2}, \tag{23}$$

where $\beta = \frac{v}{c}$ and $\gamma = \frac{1}{\sqrt{1-\beta^2}}$ are the relativistic β- and γ-factors respectively, and c is the speed of light in vacuum. Here and in the following $\langle \sim \rangle = \langle\langle\langle\langle \sim \rangle_x \rangle_{x'} \rangle_y \rangle_{y'}$, and $\langle \sim \rangle_x = \frac{\int \sim \rho(x) dx}{\int \rho(x) dx}$. So the mean value of a random variable u with the probability function ρ is defined as

$$\langle u \rangle = \mu = \frac{\int u\rho(x, x', y, y') dx dx' dy dy'}{\int \rho(x, x', y, y') dx dx' dy dy'}, \tag{24}$$

and the second moment $\langle uv \rangle$ is defined as

$$\langle uv \rangle = \frac{\int (u - \langle u \rangle)(v - \langle v \rangle)\rho(x, x', y, y') dx dx' dy dy'}{\int \rho(x, x', y, y') dx dx' dy dy'}. \tag{25}$$

The square root of Eq. (25) for the case of $v = u$ is the root-mean-square (rms) of the particle distribution ρ, i.e.

$$u_{\mathrm{rms}} = \sqrt{\langle u^2 \rangle}. \tag{26}$$

Physical measurements typically do not provide a continuous function but discrete values in time or space. For beam size measurements for example this means that deriving the rms width of a distribution requires the calculation of a sum of discrete bins in space so that

$$x_{\mathrm{rms}} = \sqrt{\frac{\sum_{i=1}^{n} \rho(x_i)(x_i - \mu)^2}{\sum_{i=1}^{n} \rho(x_i)}} = \sqrt{\frac{\sum_{i=1}^{n} \rho(x_i)(x_i)^2 - \mu^2}{\sum_{i=1}^{n} \rho(x_i)}}, \tag{27}$$

where the expected value

$$\mu = \frac{\sum_{i=1}^{n} \rho(x_i) x_i}{\sum_{i=1}^{n} \rho(x_i)}. \tag{28}$$

The pixels of a camera chip are one example of these discrete bins in space. Owing to electric noise in camera chips, low signal pixels might be regarded as noise during the image analysis process. The rms-value as defined in Eq. (26) is highly susceptible to intensity far from the mean of the particle distribution. Since typical particle beams have a negligible portion of their charge in this region, measurements of the emittance typically ignore these particles. So in reality, measurements will represent the emittance of a certain percentage of charge.

Monitoring for charge loss is therefore an important aspect of emittance measurements, since one might end up comparing different percentages of charge in the beam.

1.1.4 *Transverse emittance measurement*

For the reconstruction of the transverse emittance it is convenient to rewrite the equation for the phase-space ellipse using a symmetric *beam matrix*

$$\boldsymbol{\sigma} = \begin{pmatrix} \sigma_{11} & \sigma_{12} \\ \sigma_{21} & \sigma_{22} \end{pmatrix} = \epsilon_u \begin{pmatrix} \beta_u & -\alpha_u \\ -\alpha_u & \gamma_u \end{pmatrix}, \tag{29}$$

, with $\sigma_{12} = \sigma_{21}$ so that $\epsilon_u = \sqrt{\det \boldsymbol{\sigma}} = \sqrt{\sigma_{11}\sigma_{22} - \sigma_{12}^2}$. Using the definitions of the moments from Eq. (24) and (25) we can give a statistical definition of the beam matrix

$$\boldsymbol{\sigma}_u u = \begin{pmatrix} \langle u^2 \rangle & \langle uu' \rangle \\ \langle uu' \rangle & \langle u'^2 \rangle \end{pmatrix}. \tag{30}$$

For the transformation of the beam matrix through the beamline the identity

$$(uu') \begin{pmatrix} \sigma_{11} & \sigma_{12} \\ \sigma_{21} & \sigma_{22} \end{pmatrix}^{-1} \begin{pmatrix} u \\ u' \end{pmatrix} = 1, \tag{31}$$

where the coordinate vector $(uu') = \mathbf{U}^\mathsf{T}$ as well as $\mathbf{R}^{-1}\mathbf{R} = \mathbf{R}^\mathsf{T}\mathbf{R}^{\mathsf{T}-1}$ are used and the transformation can be written as

$$\mathbf{U}_0^\mathsf{T}\mathbf{R}^\mathsf{T}\mathbf{R}^{\mathsf{T}-1}\boldsymbol{\sigma}_0^{-1}\mathbf{R}^{-1}\mathbf{R}\mathbf{U}_0 = 1$$

$$(\mathbf{R}\mathbf{U}_0)^\mathsf{T}(\mathbf{R}\sigma_0\mathbf{R}^\mathsf{T})^{-1}\mathbf{R}\mathbf{U}_0 = 1$$

$$\mathbf{U}^\mathsf{T}(\mathbf{R}^\mathsf{T}\boldsymbol{\sigma}_0\mathbf{R}^\mathsf{T})^{-1}\mathbf{U} = 1,$$

so the beam matrix $\boldsymbol{\sigma}$ at position s is calculated from the beam matrix $\boldsymbol{\sigma}_0$ at position s_0 with the transfer matrix from position s_0 to s by

$$\boldsymbol{\sigma} = \mathbf{R}\boldsymbol{\sigma}_0\mathbf{R}^T. \tag{32}$$

Determining the transverse emittance requires the reconstruction of the beam matrix. With known linear transformations $\mathbf{R}_i$ within a section from a fixed position s_0 to another position s it is possible to determine the (2D) projected emittance by measuring the second moments $\langle u^2 \rangle_i$. The $\mathbf{R}_i$ can for example be changed by changing the position s. This can therefore be used as one approach to scanning. Another approach is to vary transport elements in the beamline in between s_0 and s and while keeping both positions fixed. This is usually achieved by choosing a beamline section with quadrupoles and varying their strength - a quadrupole scan. Combinations of both approaches can also be used. In the scope of this work only pure quadrupole scans in x were performed.

The transformation for the second moment $\langle x^2 \rangle$ of x is given by

$$\langle x^2 \rangle = R_{11}^2 \langle x_0^2 \rangle + R_{12}^2 \langle x_0'^2 \rangle + 2R_{11}R_{12}\langle x_0 x_0' \rangle, \tag{33}$$

and the three initial beam matrix $\boldsymbol{\sigma}_0$ elements can be obtained through three measurements with different transfer matrices $\mathbf{R}_i$. Taking more measurements than required will decrease the fit's sensitivity to errors. The preferred method for finding the solution for the beam matrix elements with the highest probability of representing the measurements is the χ^2-method, or the method of least-squares. In this method the expression

$$\chi^2 = \sum_{i=1}^{n} \left(\frac{\langle x_i^2 \rangle - f_i(\langle x_0^2 \rangle, \langle x_0 x_0' \rangle, \langle x_0'^2 \rangle)}{\sigma_{\langle x_i^2 \rangle}} \right)^2 \tag{34}$$

is minimized, where n is the number of measurements, $\sigma_{\langle x_i^2 \rangle}$ is the error of $\langle x_i^2 \rangle$, and

$$f_i(\langle x_0^2 \rangle, \langle x_0 x_0' \rangle, \langle x_0'^2 \rangle) = R_{11,i}^2 \langle x_0^2 \rangle + R_{12,i}^2 \langle x_0'^2 \rangle + 2R_{11,i}R_{12,i}\langle x_0 x_0' \rangle. \tag{35}$$

1.1.5 *Relativistic beam optics*

In order to transport and focus high-energy particle beams, different kinds of optics are employed. They use the Lorentz force Eq. (2) to change the particle's path as described in Sec. 1.1.1. Depending on beam parameters, there are several options on how to produce a magnetic field **B** with focusing characteristics.

Active plasma lens

The APL was first proposed in 1950 [17]. It was routinely used in Ion accelerators and has recently attracted the attention of the PBA community when it was used for the first time to focus electrons from one LWFA stage into another, enabling staged acceleration [15]. A fundamental difference to all other focusing schemes is that the particle beam crosses a current carrying region and not vacuum (see Fig. 3). The current acts as a source for a magnetic field and allows for symmetric first-order focusing, in contrast to other schemes [18]. This also means that the particle beam might interact with the plasma which serves as the conducting material during passage. This interaction has to be considered when designing an APL in particular when deciding on gas species and density used in the capillary.

As a fundamental consequence of the axial symmetry of the APL, the magnetic field is purely azimuthal. The magnetic induction

$$\nabla \times \mathbf{A} = \mathbf{B} \tag{36}$$

of an axially symmetric vector potential $\mathbf{A}(r, z) = A_r \mathbf{e}_r + A_z \mathbf{e}_z$ yields

$$(\nabla \times \mathbf{A})_r = \frac{1}{r}\frac{\partial A_z}{\partial \varphi} - \frac{\partial A_\varphi}{\partial z} = 0 \quad \Rightarrow \quad B_r = 0 \tag{37}$$

and

$$(\nabla \times \mathbf{A})_z = \frac{1}{r}\frac{\partial}{\partial r}(r A_\varphi) - \frac{1}{r}\frac{\partial A_r}{\partial \varphi} = 0 \quad \Rightarrow \quad B_z = 0. \tag{38}$$

This condition holds for arbitrary current distributions as long as axial symmetry is assumed. Employing Ampére's law

$$\oint \mathbf{B} \cdot d\mathbf{s} = \mu_0 I_{enc}, \tag{39}$$

where μ_0 is the vacuum permeability and I_{enc} is the current inside the closed line integral. Assuming a uniform current distribution over the entire cylindrical plasma discharge gives

$$I_{enc} = \left(\frac{\pi r^2}{\pi R^2}\right) I_0, \tag{40}$$

where R is the discharge (capillary) radius and I_0 is the total current flowing in the capillary. The magnetic field inside the discharge capillary can be derived to be

$$\oint \mathbf{B} \cdot d\mathbf{s} = B_\varphi 2\pi r = \mu_0 I_0 \left(\frac{2\pi r^2}{2\pi R^2}\right) \quad \Rightarrow B_\varphi = \frac{\mu_0 I_0}{2\pi} \frac{r}{R^2}. \tag{41}$$

The magnetic field gradient can be obtained by differentiating (41) with respect to r, i.e.,

$$g = \partial B_\varphi / \partial r = \mu_0 I_0 / (2\pi R^2). \tag{42}$$

In a 250 μm-radius capillary with a current of 1 kA, the field gradient reaches >3000 T/m which is orders of magnitude stronger than the strongest electro-magnetic quadrupole lenses used in state-of-the-art accelerators.

Outside the current-carrying discharge region, Eq. (39) yields $B_\varphi = \mu_0 I / 2\pi r$. Fig. 4 shows the magnetic field strength inside and outside the APL. One can see that the magnetic field gradient is constant over the entire lens. This is due to the assumption that the current density is uniform in Eq. (40). The consequences of nonuniform current densities in APLs were described in [19, 20]. A detailed description of the underlying physics is given in Sec. 1.2.1.

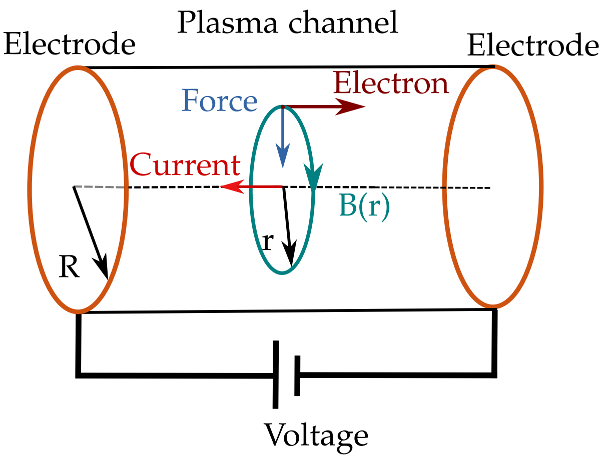

Figure 3: Schematic of the focusing mechanism in an APL.

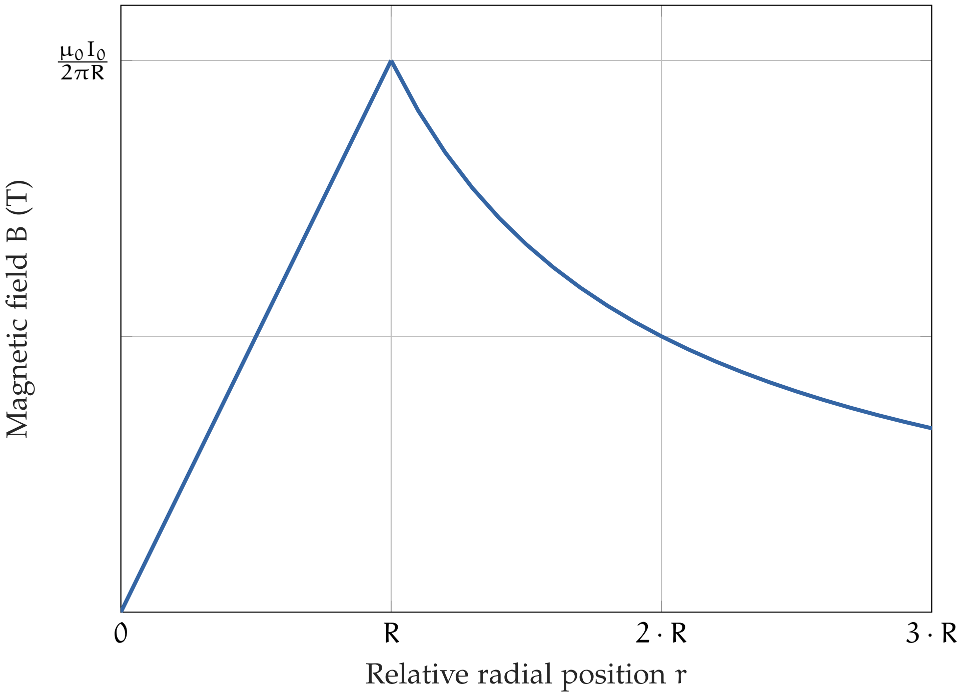

Figure 4: Qualitative plot of the magnetic field strength in- and outside a plasma discharge channel of radius R and uniform current density.

The azimuthal Mmetic field exerts a Lorentz force on electrons moving through the current-carrying region. This force is focusing if the current is antiparallel to the electron velocity. One can define a focusing parameter k as in Eq. (8) for APLs. It depends on the magnetic field gradient $g = \partial B_\varphi / \partial r$ and the particle's charge q and momentum p. Together with the APL's effective length L the focal length can be derived via the thin-lens approximation

$$f = 1/kL. \tag{43}$$

This approximation holds for lenses that have a significantly longer focal length f than their own length L. Eq. (8) and Eq. (43) yield the focal length

$$f = p/\left(qLg\right). \tag{44}$$

The transfer matrix of an APL with uniform current density is

$$\mathbf{R}^{\text{APL}}(k,l) = \begin{pmatrix} \cosh(l\sqrt{|k|}) & \frac{\sinh(l\sqrt{|k|})}{\sqrt{|k|}} & 0 & 0 \\ \sqrt{|k|}\sinh(l\sqrt{|k|}) & \cosh(l\sqrt{|k|}) & 0 & 0 \\ 0 & 0 & \cosh(l\sqrt{|k|}) & \frac{\sinh(l\sqrt{|k|})}{\sqrt{|k|}} \\ 0 & 0 & \sqrt{|k|}\sinh(l\sqrt{|k|}) & \cosh(l\sqrt{|k|}) \end{pmatrix}, \tag{45}$$

for $k > 0$. Usually the identity $\phi = l\sqrt{|k|}$ is used. For $k < 0$ the transfer matrix becomes

$$\mathbf{R}^{\text{APL}}(k,l) = \begin{pmatrix} \cos(\phi) & \frac{\sin(\phi)}{\sqrt{|k|}} & 0 & 0 \\ -\sqrt{|k|}\sin(\phi) & \cos(\phi) & 0 & 0 \\ 0 & 0 & \cos(\phi) & \frac{\sin(\phi)}{\sqrt{|k|}} \\ 0 & 0 & -\sqrt{|k|}\sin(\phi) & \cos(\phi) \end{pmatrix}. \tag{46}$$

Quadrupole

Quadrupole magnets (QMs) are the most commonly used focusing optics in particle accelerators. A schematic drawing of a quadrupole magnet is shown in figure 5. In QMs the area of the particle beam is current free. This is a practical advantage of the QM over the APL. The vacuum beam pipe can be inserted in the gap between the pole shoes and no gas is inserted into the accelerator vacuum. Since the beam path is current free, no closed magnetic-field

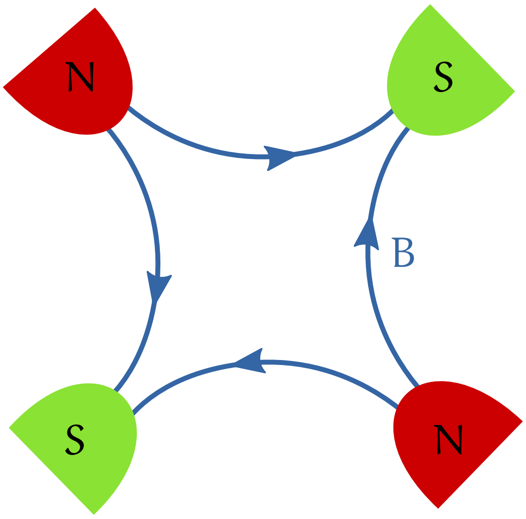

Figure 5: Schematic concept of a quadrupole magnet.

loops can be achieved in QMs ($\nabla \times \mathbf{B} = 0 \rightarrow \partial/\partial\varphi = 0$). This means QMs cannot focus radially symmetrically, but defocus in one plane. Apart from that, QMs employ the same mechanism for focusing as APLs. Equation (44) still applies for the focusing dimension. To achieve net focusing in all dimensions, multiple QMs have to be combined. A circular focal spot, for example, can be achieved by using three quadrupoles of equal maximum strength and combining them in the optimized configuration $\pm(2f, -f, f)$ of [21], where each QM is placed a distance $s = f_0$ behind the preceding. Here f_0 denotes the minimal focal length of each element for a design energy. The effective focal length of such a quadrupole triplet is

$$F = 2s + (2f^3 - fs^2)/(f^2 + fs - s^2). \tag{47}$$

This leads to a longer overall length of the focusing setup in comparison to an APL of equal magnetic-field gradient, g.

Solenoid

A solenoid magnet is a focusing magnet that consists of a coil wound into a helix of a diameter significantly smaller than the length. Solenoid lenses are a compact solution with azimuthally symmetric focusing but have a limited application range. They suffer from a unfavorable scaling of their focusing strength with $1/\gamma^2$ (see (48)). This is why they are often used near the cathode in conventional accelerators. There, the most important issue is rapid focusing while the particles are not yet relativistic. Relativistic particle beams with a significant energy spread will suffer significant aberration in a solenoid.

$$f = (m_0 \gamma c/e)^2/(B^2 L). \tag{48}$$

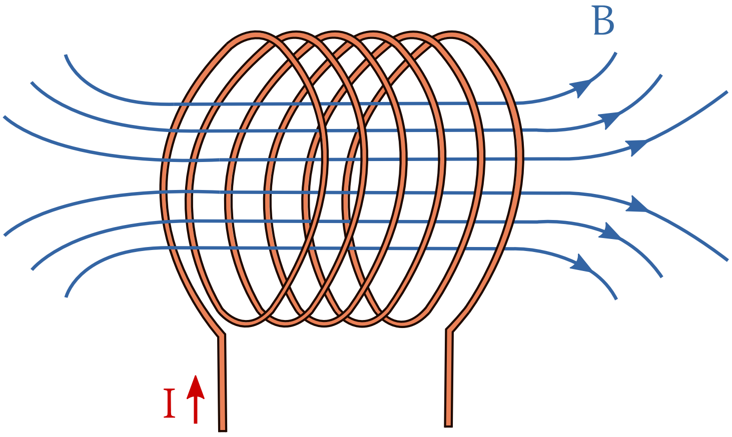

Figure 6: Schematic drawing of a solenoid magnet.

1.1.6 *Quality degradation effects*

Although Liouville's theorem states that the phase-space density or emittance is a constant of motion for charged particles, there are mechanisms that will increase or decrease it. One example is acceleration which will decrease the emittance of a beam by decreasing the ratio p_u/p_z. Likewise, there are beams that are not subject to Liouville's theorem, for example, beams with an energy spread. This Section discusses the most relevant mechanisms for emittance degradation.

Nonlinear beam optics

Charged-particle beams passing an azimuthal magnetic field with a nonlinear gradient will experience emittance degradation. In the following, this effect is estimated analytically using the field behavior $B_\phi(r) = c_1 \cdot r + c_3 \cdot r^3 + c_5 \cdot r^5$ as described in detail in 1.2.1, specifically Eq. (80). Since the field is radially symmetric, the following estimation is done in the horizontal plane but also applies for the vertical plane. To compare the results to particle tracking simulations, the beam is assumed to be Gaussian, such that

$$\langle \sim \rangle_r = \frac{1}{\sqrt{2\pi} r_{\mathrm{rms}}} \int_{-\infty}^{\infty} \sim e^{\frac{-r^2}{2r_{\mathrm{rms}}^2}} dr, \tag{49}$$

with $r = x, y$ and $\langle 1 \rangle_r = 1$, $\langle r^2 \rangle_r = r_{\mathrm{rms}}^2$, $\langle r^3 \rangle_r = 0$, $\langle r^4 \rangle_r = 3 \cdot r_{\mathrm{rms}}^4$, $\langle r^5 \rangle_r = 0$, $\langle r^6 \rangle_r = 15 \cdot r_{\mathrm{rms}}^6$, $\langle r^7 \rangle_r = 0$, $\langle r^8 \rangle_r = 105 \cdot r_{\mathrm{rms}}^8$, $\langle r^9 \rangle_r = 0$ and $\langle r^{10} \rangle_r = 945 \cdot r_{\mathrm{rms}}^{10}$.
Charged particles passing through the field described above will experience a radial force of the form

$$F_r = [-e\mathbf{v} \times \mathbf{B}]_r = -e(-v_z B_\phi) = ev_z(g \cdot r + c_3 \cdot r^3 + c_5 \cdot r^5). \tag{50}$$

They will pick up the additional momentum

$$p_x = \int_{-\infty}^{\infty} F_r dt = e \int_0^L (g \cdot r + c_3 \cdot r^3 + c_5 \cdot r^5) dz. \tag{51}$$

Using the thin lens approximation, which means radial particle positions are assumed constant during the passage of the magnetic field thus do not depend on z, the integration can be performed and the momentum can be written as

$$p_x = eL(g \cdot r + c_3 \cdot r^3 + c_5 \cdot r^5) dz. \tag{52}$$

The emittance growth is caused by the higher-order terms of the field and not by the linear gradient g, thus the slope of the linear correlations $\langle r \cdot p_r \rangle$ that do not contribute are subtracted from the transverse momentum.

$$\bar{p}_r = p_r - \frac{\langle r \cdot p_r \rangle}{\langle r^2 \rangle} r, \tag{53}$$

in which

$$\begin{aligned} \langle r \cdot p_r \rangle &= eL \langle g \cdot r^2 + c_3 \cdot r^4 + c_5 \cdot r^6 \rangle \\ &= eL(g \cdot r_{\mathrm{rms}}^2 + 3 \cdot c_3 \cdot r_{\mathrm{rms}}^4 + 15 \cdot r_{\mathrm{rms}}^6). \end{aligned} \tag{54}$$

The corrected transverse momentum then reads

$$\begin{aligned} \bar{p}_r &= eL[gr + c_3 \cdot r^3 + c_5 \cdot r^5 - \frac{r}{r_{\mathrm{rms}}^2}(g \cdot r_{\mathrm{rms}}^2 + 3 \cdot c_3 \cdot r_{\mathrm{rms}}^4 + 15 \cdot r_{\mathrm{rms}}^6)] \\ &= eL[c_3 \cdot (r^3 - 3 \cdot r \cdot r_{\mathrm{rms}}^2) + c_5 \cdot (r^5 - 15 \cdot r \cdot r_{\mathrm{rms}}^4)]. \end{aligned} \tag{55}$$

With this the variance of p_r can be calculated to be

$$\begin{aligned} \langle \bar{p}_r^2 \rangle &= (eL)^2 \langle [c_3(r^3 - 3rr_{\mathrm{rms}}^2) + c_5(r^5 - 15rr_{\mathrm{rms}}^4)]^2 \rangle \\ &= (eL)^2 (6c_3^2 r_{\mathrm{rms}}^6 + 720 c_5^2 r_{\mathrm{rms}}^{10} + 120 c_3 c_5 r_{\mathrm{rms}}^8). \end{aligned} \tag{56}$$

Emittance growth by higher-order magnetic-field effects is additive. The added normalized emittance $\epsilon_{n,APL}$ is quadratically added to the initial normalized emittance $\epsilon_{n,i}$, so the final normalized emittance $\epsilon_{n,f}^2 = \epsilon_{n,i}^2 + \epsilon_{n,APL}^2$, with

$$m_0^2 c^2 \epsilon_{n,APL}^2 = \langle r^2 \rangle \langle \bar{p}_r^2 \rangle = r_{\mathrm{rms}}^2 \cdot (eL)^2 \cdot (6 \cdot c_3^2 \cdot r_{\mathrm{rms}}^6 + 720 \cdot c_5^2 \cdot r_{\mathrm{rms}}^{10} + 120 \cdot c_3 \cdot c_5 \cdot r_{\mathrm{rms}}^8), \tag{57}$$

and

$$m_0^2 c^2 \epsilon_{n,i}^2 = \langle r_i^2 \rangle \langle p_{r,i}^2 \rangle = r_{\mathrm{rms}}^2 p_{rms,i}^2, \tag{58}$$

in which $p_{rms,i}$ is the initial rms of the transverse momentum distribution. Since the thin lens approximation is applied, the initial and final beam sizes are assumed to be equal: $r_{rms,i} = r_{rms,f} = r_{\mathrm{rms}}$. The relative normalized emittance growth introduced by the APL reads

$$\frac{\epsilon_{n,f}}{\epsilon_{n,i}} = \sqrt{1 + \left(\frac{eL}{p_{rms,i}}\right)^2 \cdot \left(6 \cdot c_3^2 \cdot r_{\mathrm{rms}}^6 + 720 \cdot c_5^2 \cdot r_{\mathrm{rms}}^{10} + 120 \cdot c_3 \cdot c_5 \cdot r_{\mathrm{rms}}^8\right)} \tag{59}$$

As an example one might take the nonlinearity factors c_3 and c_5 from the $J \sim T^{3/2}$-model described in Sec. 1.2.1 with a cold-wall boundary condition in Eq. (80), $I_0 = 400\,\mathrm{A}$ total current, a radius of $R = 0.5\,\mathrm{mm}$, and a length of $L = 15\,\mathrm{mm}$. Now a beam with a relatively low normalized emittance of $\epsilon_{n,i} = 0.5\,\mathrm{mm\,mrad}$ traversing this field, the final emittance is shown in Fig. 7. The high dependence of the emittance growth on the beam size from Eq. (59) can clearly by seen there.

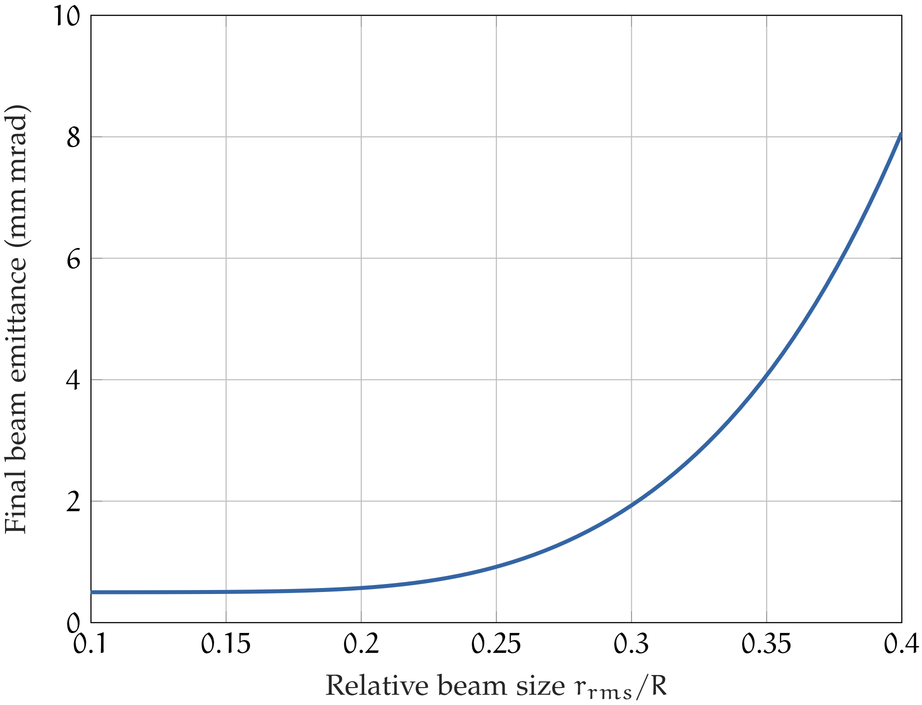

Figure 7: Final emittance of a beam of initial emittance $\epsilon_{n,i} = 0.5\,\mathrm{mm\,mrad}$ traversing an APL of $R = 0.5\,\mathrm{mm}$ diameter, $L = 15\,\mathrm{mm}$ length, $I_0 = 400\,\mathrm{A}$ following the $J \sim T^{3/2}$-model.

Chromatic effects

Apart from nonlinear effects in beam optics, there is an intrinsic quality degradation effect for particle beams with a significant energy spread. Beams from PBAs typically have an intrinsically high energy spread - ranging from a few to ~100 % depending on the injection mechanism - and large divergence (~ 1 mrad). A significant part of this energy spread can stem from electrons being accelerated in different phases of the plasma wave which may lead to a correlated energy spread. Recent experimental results from FLASHForward at DESY show that this kind of energy spread can be reduced by dechirping [22]. The remaining uncorrelated energy spread might still lead to degradation but has yet to be measured.

Two major degradation effects take place during the transport of such beams. Firstly a normalized emittance growth arises from chromatic effects [14, 23]. This effect can be illustrated by cutting the beam into the different 'energy slices'. The phase-space ellipses of these slices will shear at different speeds in a drift section. Secondly a bunch elongation due to path-length differences between particles in the central part of the beam and those further out. In the following, the normalized emittance degradation will be discussed.

Deploying the definition of the normalized emittance from Eq. (23) and considering the fact that the correlation between the energy and the transverse position is negligible, one finds

$$\epsilon_u^2 = \langle \beta^2\gamma^2 \rangle \langle u^2 \rangle \langle u'^2 \rangle - \langle \beta\gamma \rangle^2 \langle uu' \rangle^2. \tag{60}$$

Now taking the general definition of a relative energy spread σ_E

$$\sigma_E^2 = \frac{\langle \beta^2\gamma^2 \rangle - \langle \beta\gamma \rangle^2}{\langle \gamma \rangle^2}, \tag{61}$$

and assuming relativistic energies ($\beta = 1$), (61) yields

$$\epsilon_u^2 = \langle \gamma \rangle^2 \cdot (\sigma_E^2 \cdot u_{\mathrm{rms}}^2 \cdot u'^2_{\mathrm{rms}} + \hat{\epsilon}), \tag{62}$$

in which $\hat{\epsilon}$ is the geometric emittance. This means that the normalized emittance $\hat{\epsilon}_n$ grows during a drift s depends on the energy spread σ_E, the beam size u_{rms} and the beam divergence u'_{rms}. For beams with high divergence, the beam size is dominated by the divergence after a short drift. So (62) can be rewritten to be

$$\epsilon_u^2 \approx \langle \gamma \rangle^2 \cdot (\sigma_E^2 \cdot u'^4_{\mathrm{rms}} \cdot s^2 + \hat{\epsilon}). \tag{63}$$

For beams with a small initial geometric emittance $\hat{\epsilon}$ - as is the case with plasma-accelerated electrons - (63) can be simplified further to

$$\epsilon_u \approx \langle \gamma \rangle \cdot \sigma_E \cdot u'^2_{\mathrm{rms}} \cdot s. \tag{64}$$

This shows that minimizing energy spread and divergence of plasma-accelerated beams is of paramount importance for the quality preservation of plasma accelerated beams. Also capturing the beam after the shortest possible drift will have a significant impact on the emittance. Capturing the beam with an APL has another advantage over quadrupoles, namely the symmetry in vertical and horizontal focusing. Quadrupoles can focus beams only in one dimension and will always defocus equally strongly in the other. APLs can capture in both dimensions, which circumvents the increased emittance degradation in the plane that the first quadrupole would defocus in.

Other effects

Besides nonlinear beam optics and chromatic effects, there are more mechanisms that can lead to emittance degradation, such as plasma wakefields and scattering of the beam with gas and plasma. These effects are discussed in Sections 1.2.2 and 1.2.3 respectively.

Comparison

The beam optics discussed in Sec. 1.1.5 all have their distinct areas of application. Beams exiting PBAs are highly relativistic and typically have a percent-level energy spread. Thus solenoids are not suitable for capturing, owing to their high chromatic dependence and relatively weak focusing strength. They are useful for reducing the energy spread of beams and focusing low-energy beams and are routinely used in the earliest stages of conventional accelerators near the cathode. QMs have a higher field strength and $1/\gamma$-dependence of their focal length but the effective focal length F is dominated by the fact that at least 2 elements of opposite strengths need to be combined to achieve focusing in both planes [21]. For a symmetric focusing scheme, this will yield the overall focal length as described in Eq. (47). APLs can achieve extremely high focusing fields (on the order of several kT/m) utilizing the same focusing mechanism as QMs. APLs and QMs have the same single-element relative chromatic dependence $|\Delta F|/F_0$ in the focusing plane of the QM. The absolute chromaticity is better for elements with a shorter focal length, so the APL produces better results, asdemonstrated in the top part of Fig. 8. Using a triplet, however, is better in terms of relative chromatic dependence, as seen in the bottom part. It should be noted, however, that APLs may also be combined into a triplet as well, yielding an even better overall beamline in terms of emittance preservation. This has recently been shown in [24], where beamlines with APLs are compared to beamlines with QMs. It shows that beamlines with APLs can be tailored to yield focusing with low chromatic dependence. Using APLs instead of quadrupoles is advantageous for this because of the APL's azimuthal symmetry, resulting in lower chromatic dependence of the β at a given point in the beam line.

In terms of emittance preservation, it is of paramount importance to use an optics setup that reduces the beam divergence as quickly as possible in order to tackle the chromatic emittance growth. The active plasma lens has two advantages over QMs in this regard. First, it is a single element that does not defocus in one dimension. It reduces the emittance growth, where the QM increases the divergence in one dimension even further. Secondly, it can deliver kT/m-level field gradients. This opens up the possibility of capturing beams close to the source and consequently lowering the emittance growth. APLs also have a tunable field gradient which makes them easier to use than permanent QMs, APLs and QMs may be prone to emittance degradation through nonlinear magnetic-field gradient as described in Sec. 1.2.1 and Sec. 1.1.6. In order to assess whether APLs are a viable alternative to QMs for beam capture or beamline design, a good understanding of the nonlinearity and its effect on a traversing beam is necessary. The present work focuses on probing APLs experimentally for their nonlinear magnetic fields and their impact on a passing electron beam's quality.

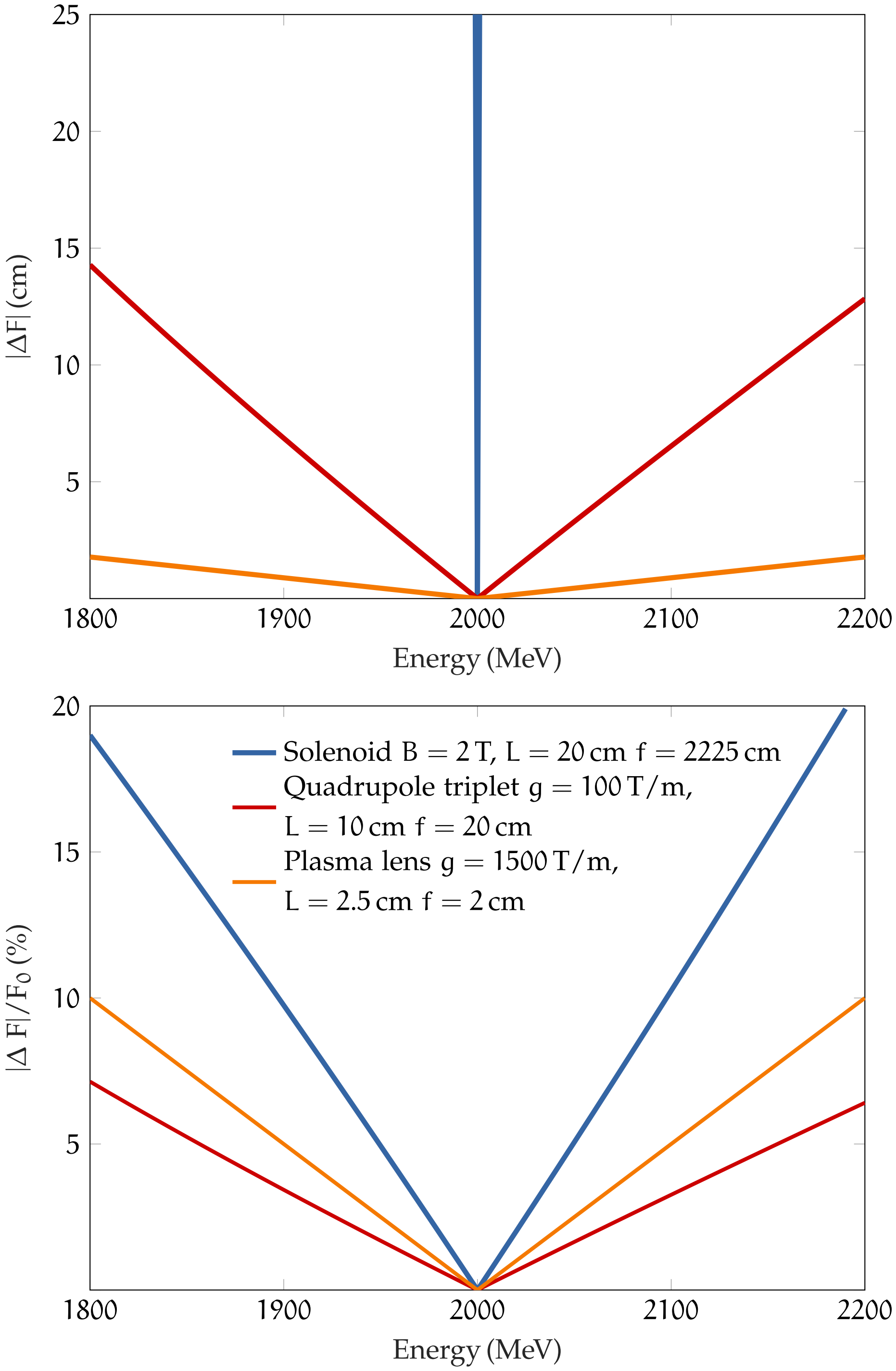

Figure 8: Top: absolute chromaticity of focusing elements with typical strength and length parameters. Bottom: relative chromaticity of the same elements. The upper graph was used in [25] but was mislabeled with relative chromaticity.

Plasma is the most common state of visible matter in the universe both by volume and mass. Perhaps the most prominent examples of plasma are the sun's corona, the one created by lightning, and fire. The plasma in the scope of this work is created by applying a high voltage to a neutral gas, similar to lightning strikes. The term plasma refers to ionized matter with a wide range of densities and temperatures. In the scope of this work, for matter to be considered plasma the following criteria must be met:

1 Plasma is spatially quasi neutral. The Debye screening length $\lambda_D = \sqrt{\epsilon_0 k_B T_e / n_e e^2}$ - the length over which the electric potential of a charge carrier is reduced by $1/e$ - has to be small in comparison to the boundaries of the plasma volume and the process in question. Here ϵ_0 is the vacuum permittivity, k_B the Boltzmann constant, T_e the electron temperature, n_e the electron density, and e the elementary charge.

2 The plasma frequency $\omega_p = \sqrt{4\pi n_e e^2 / m_e}$ has to be larger than a characteristic frequency of the process. This means that plasma is temporally neutral over periods of time much larger than the processes in question.

3 Collective electrostatic effects have to dominate over binary particle interactions. This means the plasma parameter $\Lambda = n_e \lambda_D^3$ has to be much larger than 1.

These are referred to as ideal plasma conditions.

1.2.1 *Capillary discharge*

An APL for electron focusing as discussed in this work typically consists of a few cm long, round, gas-filled capillary of $\sim 0.1 - 1\,\text{mm}$ diameter [25]. A high voltage ($\sim 25\,\text{kV}$) is applied to the capillary so that a Townsend discharge ionizes the gas and a current density forms inside the capillary. The magnetic field behavior in the capillary discharge depends on the radial dependence of the current density. This section introduces an analytical model for the current density behavior inside a capillary discharge following the work in [19, 26]. In accordance with these works, this model will in the following be referred to as $J \sim T^{3/2}$-model. In the following description, no azimuthal dependence is taken into account because of the radial symmetry of the capillary discharge setup. The effect that the behavior explained in the following has on a charged particle beam will be discussed later in Sec. 1.1.5 and 1.1.6.

In a Spitzer collisional model of plasma, the conductivity σ depends on the plasma density n_e and temperature T_e via

$$\sigma = \frac{32\epsilon_0^2}{\ln\Lambda} \cdot \frac{(k_B T_e)^{3/2}}{e^2 m_e^{1/2}}, \tag{65}$$

with k_B the Boltzmann constant, ϵ_0 the vacuum permittivity, $-e$ the electron charge, and m_e the electron mass. This shows that the scaling of σ is dominated by T_e since n_e appears only logarithmically in Λ. With typical plasma temperatures ranging from 1 eV or 10^4 K and wall temperatures near 300 K, a radial temperature gradient forms, leading to a radial dependence of the conductivity. The static heat-flow equation is

$$\Delta \cdot (\kappa \Delta T) = -J \cdot E, \tag{66}$$

where κ is the thermal conductivity, E the field of the applied discharge, $T = T_i = T_e$ is the temperature. Here, a thermal equilibrium between electron temperature T_e, and ion temperature T_i is assumed. In reality, this equilibrium is only reached after a 4-step process [27]. First, a cold plasma is formed. Secondly, the electron temperature rises due to Joule heating. However, the heat transfer from electrons to the wall is hindered by a thin, virtually electron-free sheath near the wall. So the third step is heat transfer from the electrons to the ions. The timescale of this step is dominated by the electron-ion heat conductivity which is inversely proportional to the ion mass. Lastly, the ions transfer heat to the capillary wall. This leads to a colder plasma temperature near the wall and a temperature gradient. This temperature gradient reaches a steady-state on a timescale that varies between gas species, since the ion thermal conductivity is also inversely proportional to the ion mass. The steady-state solution found in [26] is described in the following.

The current is given by Ohm's law

$$J = \sigma E. \tag{67}$$

Neglecting the weak logarithmic scaling, the conductivity becomes $\sigma = \sigma_0 T^{3/2}$ and the current density is

$$J = (\sigma_0 E) T^{3/2}. \tag{68}$$

The static heat-flow equation can then be rewritten as

$$\frac{1}{r}\frac{\partial}{\partial r}\left(r T^{5/2}\frac{\partial T}{\partial r}\right) = -(\sigma_0/\kappa_0)E^2 T^{3/2}. \tag{69}$$

With a scaling function for the heat flow equation [26]

$$T_e(x) = A u(x)^{2/7}, \tag{70}$$

with

$$A = (7\sigma_0 R^2 E^2 / 2\kappa_0)^{1/2}, \tag{71}$$

and $x = r/R$, where R is the capillary radius, one can write $T = [(7\sigma_0/2\kappa_0)^{1/2} RE] u^{2/7} = A u^{2/7}$. Using this scaling function, the static heat flow-equation becomes

$$u'' + \frac{1}{x} u' = -u^{3/7}. \tag{72}$$

Two boundary conditions are needed to solve this differential equation. Continuity at the axis demands the solution must satisfy $\partial_r T(r = 0) = 0$, or $u'(0) = 0$, providing the first boundary condition. The second boundary condition can be found by assuming a fixed electron temperature at the wall, for example a cold wall with $T_e(r = R) = T^* = 0\,\mathrm{eV}$ [19, 26]. There is ongoing research into models for the plasma-wall interaction which result in a temperatures between 0 and 1 eV [27], with some models suggesting that a sheath may form at the wall that acts as a form of transition region with even higher temperatures. The fixed boundary condition translates into a fixed $u(1)$ dependent on the scaling factor A. This provides a means of optimization since σ_0/κ_0 is a material dependent property. Choosing a gas species with a high thermal conductivity in comparison to its electric conductivity is beneficial. It may allow the plasma to transport the heat to the wall, yielding a more uniform conductivity. Eq. (68) can be rewritten as $J = J_0 u^{3/7}$, and J_0 can be determined from the applied current

$$I_0 = \int_0^R 2\pi J dr = 2\pi R^2 J_0 \int_0^1 u^{3/7} x dx. \tag{73}$$

Defining the integral $\int_0^1 u^{3/7} x dx = m_I$ the current density becomes

$$J = \frac{I_0}{\pi R^2} \left(\frac{u^{3/7}}{2m_I} \right). \tag{74}$$

For a cold-wall boundary condition $T_* \simeq 0$, the numerical solution of Eq. (72) yields the case of maximal nonlinearity, since $u(0, T_*)$ is a monotonically rising function of the wall temperature. Since J follows the behavior of $T^{3/2}$, a warmer wall will naturally lead to more uniform current density behavior. In the cold-wall case, the peak current density on axis is enhanced by 48%

in comparison relative to the uniform case $J(r=0) \simeq 1.48\left(\frac{I_0}{\pi R^2}\right)$.
Using Ampère's law $\Delta \times B = \mu_0 J$, the magnetic field is $B = \frac{\mu_0}{r}\int rJdr$, or

$$B = \frac{\mu_0 I_0}{2\pi R m_I}\frac{1}{x}\int x u^{3/7} dx. \tag{75}$$

Now consider a polynomial expansion of the current density J normalized to the peak current on axis J_p,

$$\hat{J} = \frac{J}{J_p} = \frac{u^{3/7}}{u(0)^{3/7}} = 1 + a_1 x + a_2 x^2 + a_3 x^3 + a_4 x^4 ... \tag{76}$$

The solution must satisfy $\hat{J}'(0) = 0$, hence $a_1 = 0$. Rewriting equation (72) we find

$$\frac{4}{3}\hat{J}^{1/3}\hat{J}'^2 + \hat{J}^{4/3}(\hat{J}'' + \hat{J}'/x) = -\frac{3}{7}u(0)^{-4/7}\hat{J}. \tag{77}$$

Substituting the polynomial expansion Eq.(76) yields

$$\frac{4}{3}\left(1 + \frac{1}{3}a_2 x^2 + ...\right)(4a_2^2 x^2) + \left(1 + \frac{4}{3}a_2 x^2 + ...\right)(4a_2 + 9a_3 x + 16 a_4 x^2 ...) \tag{78}$$

$$= \frac{3}{7}u(0)^{-4/7}(1 + a_2 x^2 + ...).$$

Taking the two leading orders in the current density and magnetic field, we can write

$$J = \frac{I_0}{\pi R^2}\left(\frac{u(0)^{3/7}}{2m_I}\right)\left[1 - \frac{3}{28}u(0)^{-4/7}x^2 - \frac{15}{3136}u(0)^{-8/7}x^4\right], \tag{79}$$

and using Ampère's law $B = \frac{\mu_0}{r}\int rJdr$, the magnetic field

$$B_\phi = \frac{\mu_0 I_0}{2\pi R}\left(\frac{u(0)^{3/7}}{2m_I}\right)x\left[1 - \frac{3}{56}u(0)^{-4/7}x^2 - \frac{5}{3136}u(0)^{-8/7}x^4\right]. \tag{80}$$

Following the work of [26], the wall temperature is fixed at a finite temperature, resulting in a temperature gradient. This model describes the plasma in its equilibrium condition. A boundary condition of $T_e(r = R) = 0.5\,\text{eV}$ will yield the solution $u(0) \simeq 0.067$, $mI \simeq 0.106$ and the behavior shown in Fig. 9. With these values, the magnetic field at the wall will not be the same as in the ideal case. In fact, $B_\phi(x = 1)/B_{\phi,\text{ideal}}(x = 1) = 1.10$. This is a violation of Ampère's law for the outer most region. For the sake of modeling the region relevant for beam focusing which is close to the core, however, the model provides a good approximation [19].

Introducing the core gradient increase factor

$$\Delta g = (\partial B/\partial r)_{r=0}/(\partial B/\partial r)_{\mathrm{uniform}} = \frac{u(0)^{3/7}}{2m_I}, \tag{81}$$

one can derive $\Delta g = 1.38$ for the above boundary condition and $\Delta g = 1.48$ for a cold wall boundary condition. In [28] a plasma sheath at the wall 1 eV is assumed, leading to a much more linear behavior. The plasma-wall interaction in capillary discharges has not been thoroughly studied for APLs. This is also not the scope of this work, however the measurements performed may shed some light on which of the above assumptions is more accurate.

Another important aspect for APLs concerning the discharge behavior is the formation of fringe fields at the capillary exits. This has recently been described in [29]. The fringe field length as well as its longitudinal characteristics are of interest for the APL since the effective length may be underestimated were only capillary length accounted for. Simulation results using the capillary design used in the scope of this work are provided in Sec. 4.2.

The discharge voltage necessary for breakdown U_B varies with the gas species used as described by Paschen's law [30]

$$U_B = \frac{Bpd}{\ln(Apd) - \ln(\ln(1 + 1/\gamma_{se}))}. \tag{82}$$

The coefficients A and B are gas-species specific and can be found in Tab. 1 for some typical gas species. The secondary electron emission coefficient at the cathode γ_{se} varies with cathode material. A plot of Paschen's law for gas species commonly used in plasma experiments and a fixed $\gamma_{se} = 0.1$ can be found in Fig. 10.

1.2.2 *Plasma wakefields*

When a high intensity laser pulse or a relativistic high-density charged-particle beam is focused into a plasma, plasma waves can be excited. Those waves follow the driving laser or beam, which produce electric field gradients of GV/m. The field following the driver is called plasma wakefield and can be used to accelerate or manipulate charged-particle beams. Conventional radio-frequency (RF) cavities are limited in their electric field gradient to ~100 MV/m due to material breakdown. So particle accelerators with energies of >100 MeV

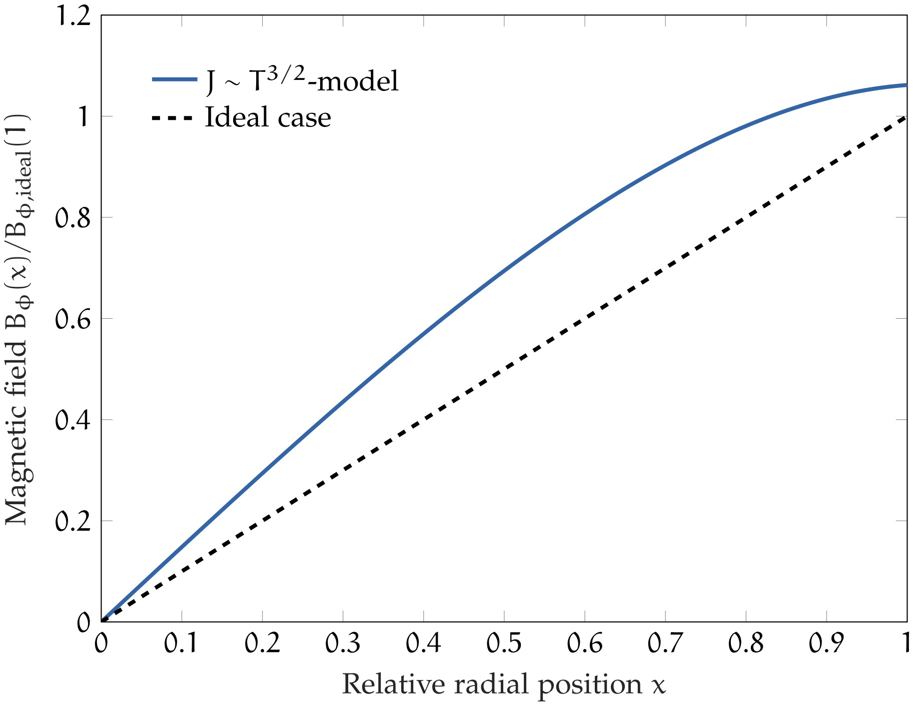

Figure 9: Magnetic field behavior according to the $J \sim T^{3/2}$-model for $u(0) = 0.067$ and $mI = 0.106$ and the uniform or ideal case. Here, the fact that the $J \sim T^{3/2}$-model does not necessarily fulfill $B_\phi(x = 1) = B_{\phi,\mathrm{ideal}}(x = 1)$ can be seen.

Table 1: Paschen's law coefficients of difference gas species.

Gas species	A ($\mathrm{cm^{-1}\,Torr^{-1}}$)	B ($\mathrm{V\,cm^{-1}\,Torr^{-1}}$)	Range of E/p ($\mathrm{V\,cm^{-1}\,Torr^{-1}}$)
He	2.8	77	30-250
Ne	4.4	111	100-400
Ar	11.5	176	100-600
Kr	15.6	220	100-1000
Xe	24	330	200-800
H_2	4.8	136	15-600
N_2	11.8	325	100-600

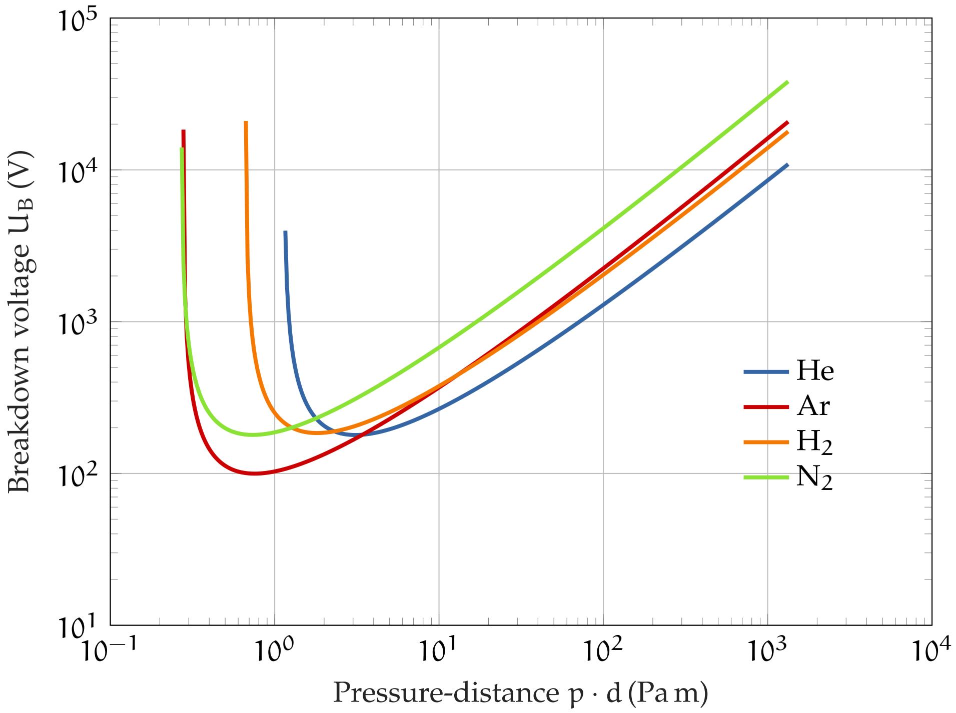

Figure 10: Paschen curves for typical gas species and a common secondary electron emission coefficient $\gamma_{se} = 0.1$.

have to use a longer section of accelerating structures or use the same accelerating structures multiple times as in circular accelerators. In the ongoing endeavor of increasing acceleration gradients and shrinking the size and cost of accelerator facilities, plasma-based acceleration (PBA) facilitates are therefore a promising candidate.

While this field is interesting and complex, for the scope of this work we will concentrate on the focusing fields in plasma waves. We will use these to evaluate whether a beam traversing the an APL will perturb the plasma strongly enough so that the electric field from the plasma wave can no longer be neglected in comparison with the focusing field of the APL. The following follows the work in [31].

In the pertubative linear regime, the plasma density perturbation is given by

$$\delta n(z,r) = -k_p \int_z^\infty n_b(z',r) \cdot \sin(k_p(z-z'))dz', \tag{83}$$

in which

$$k_p = \sqrt{\frac{n_0 e^2}{\epsilon_0 m_e c^2}} \tag{84}$$

is the plasma wave number, and

$$n_b(z, r) = -\frac{N \cdot exp(-r^2/2 \cdot r_{\mathrm{rms}}^2 - z^2/2 \cdot z_{\mathrm{rms}})}{(2\pi)^{3/2} r_{\mathrm{rms}}^2 z_{\mathrm{rms}}}, \tag{85}$$

with N particles in the bunch. We consider the long bunch regime, where $k_p z_{rms} \gg 1$ since this is the regime in which all experiments were performed. The bunch length used was of the order of $z_{rms} \simeq 1\,\mathrm{cm}$ - see Appendix B. With plasma density $n_e = 2 \cdot 10^{17}\,\mathrm{cm}^{-3}$, this is well in the long-bunch regime $k_p z_{rms} \simeq 600$. Following [32], the focusing gradient in the plasma wave is

$$g_{\mathrm{wave}}(z, r) = \frac{1}{c} \frac{\delta E_r(z, r)}{\delta r}, \tag{86}$$

normalized by c to make it comparable to the magnetic focusing field in the APL. In the long bunch regime the maximum focusing gradient becomes

$$g_{\mathrm{max,wave}} = \frac{ec\mu_0 N k_p^2 z_{\mathrm{rms}}}{2\pi r_{\mathrm{rms}}^2 (1 + \frac{k_p^2 r_{\mathrm{rms}}^2}{2})(1 + \sqrt{8\pi} k_p^2 z_{\mathrm{rms}}^2)}. \tag{87}$$

Now we can compare the wakefield gradient with the lowest magnetic-field gradient used in the scope of this work, $g_{\mathrm{min,APL}} \sim 200\,\mathrm{T/m}$ - see Sec. 3 -

$$\frac{g_{\mathrm{min,APL}}}{g_{\mathrm{max,wave}}} \simeq 5 \cdot 10^6. \tag{88}$$

This shows that the focusing fields from plasma waves can be neglected here.

In the endeavor to capture plasma accelerated beams with as little emittance degradation as possible, another type of plasma-wave focusing is of interest: the passive plasma lens (PPL)[33]. This technique relies on the nonlinear or blowout regime of plasma waves. The blowout regime can be reached when the drive beam's density is greater than the plasma density and the beam is transversely matched. Matching means that the envelope of a beam in a focusing channel with the focusing parameter K does not oscillate. This means that the matched Courant-Snyder parameters are $\beta_m' = 0 = \alpha_m$. In a constant focusing channel, (16) has the solution [18]

$$\beta(z) = \beta_0 \cos^2(\sqrt{K}z) + \frac{1}{\beta_0 K} \sin^2(\sqrt{K}z). \tag{89}$$

With this we can find the condition $\beta_m = \beta_0 = K^{-1/2}$. The matched Courant-Snyder parameters of a beam in a constant focusing channel then read

$$\alpha_m = 0, \beta_m = \frac{1}{\sqrt{K}}, \gamma_m = \sqrt{K}. \tag{90}$$

A detailed description of matched and unmatched beams in focusing plasma channels can be found in [34]. The focusing in the blowout regime acts as the constant focusing channel mentioned above. The focusing force is linearly dependent on the displacement [35]

$$F_r = -\frac{m_e c^2 k_p^2}{2} r. \tag{91}$$

A beam driving a blowout regime or being accelerated in one will not experience emittance degradation from the focusing force. As discussed in Sec. 1.1.6, beams from plasma accelerators with a significant energy spread will experience emittance growth in the drift following their acceleration stage. This is due to their high divergence in combination with the energy spread. The blowout regime focusing parameter K_{wake} in Eq. (4) can be defined as

$$K_{\text{wake}} = \frac{k_p^2}{2\gamma}. \tag{92}$$

Because k_p depends on the plasma density as in Eq. (84), K will also depend on it. It has been proposed to use a tapered plasma density to match the beam to lower divergence in [36]. With the definition of the Twiss parameters in Eq. (20) and Eq. (4), this yields

$$\beta\beta'' - \frac{1}{2}\beta'^2 + 2K_{\text{wake}}\beta^2 - 2 = 0. \tag{93}$$

The fact that the focusing strength is proportional to the plasma density provides a means of shaping the focusing characteristics longitudinally. Since the condition $n_b \gg n_e$ needs to be met, but with focusing present $n_b(s)$ will increase with the longitudinal coordinate s, it is possible to slowly ramp up the plasma density n_e leading to increasingly stronger focusing. If this ramp is slow enough so that the beta-function of the beam can adjust to the new equilibrium, it is called adiabatic. In an adiabatic focusing channel, the emittance of the beam is preserved, while divergence and beam size can be manipulated. The normalized emittance growth due to a large divergence and energy spread is discussed in Sec. 1.1.6. Using an adiabatic ramp at the plasma-to-vacuum transition in a PBA can help to mitigate this emittance growth [36]. A more detailed discussion is given in Chapter 4.4.

While the ideal blowout regime does not introduce emittance degradation, it has been shown that it does introduce longitudinal aberration [37]. It has to be noted, that the passive plasma lens has the potential to deliver even stronger focusing gradients than the APL. For a typical plasma density of $n_0 = 10^{17}\,\mathrm{cm}^{-3}$, the linear focusing field is on the order of $900\,\mathrm{TeV/m^2}$, equivalent to $3\,\mathrm{MT/m}$ [38].

Linear wakefields on the other hand do introduce emittance degradation owing to their nonlinear focusing - see Eq. (87). While the effect is negligible here [31], for other applications, especially with higher beam density, particular care has to be taken when choosing gas species and density in the APL in order to mitigate wakefields.

1.2.3 *Beam-plasma scattering*

A detrimental mechanism in all plasma-based focusing and acceleration techniques is beam-plasma scattering. The emittance growth from collisions of beam particles with plasma particles can be estimated for:

1. Multiple scattering in neutral background gas [18],
2. Bremsstrahlung [9, 39],
3. Stopping power effects in plasma from collisions with free, bound and screened electrons [9, 40].

Owing to the low beam current ($\sim 100\,\mu\mathrm{A}$) and the relatively low plasma density ($\sim 10^{17}\,\mathrm{cm}^{-3}$), these effects can be ignored in the work described here. Their combined effect on the beam is neglible compared to the effect of the nonlinear focusing force of the APL [20].

2

PLASMA LENS CHARACTERIZATION SETUP

This chapter illustrates the design of experimental campaigns designed to probe the magnetic-field quality of an APL. The first section provides all relevant details on the experiments performed at the Mainz Microtron in the scope of this work. The second section illustrates another campaign at the CLEAR facility at CERN performed in collaboration with the Universities of Oslo and Oxford.

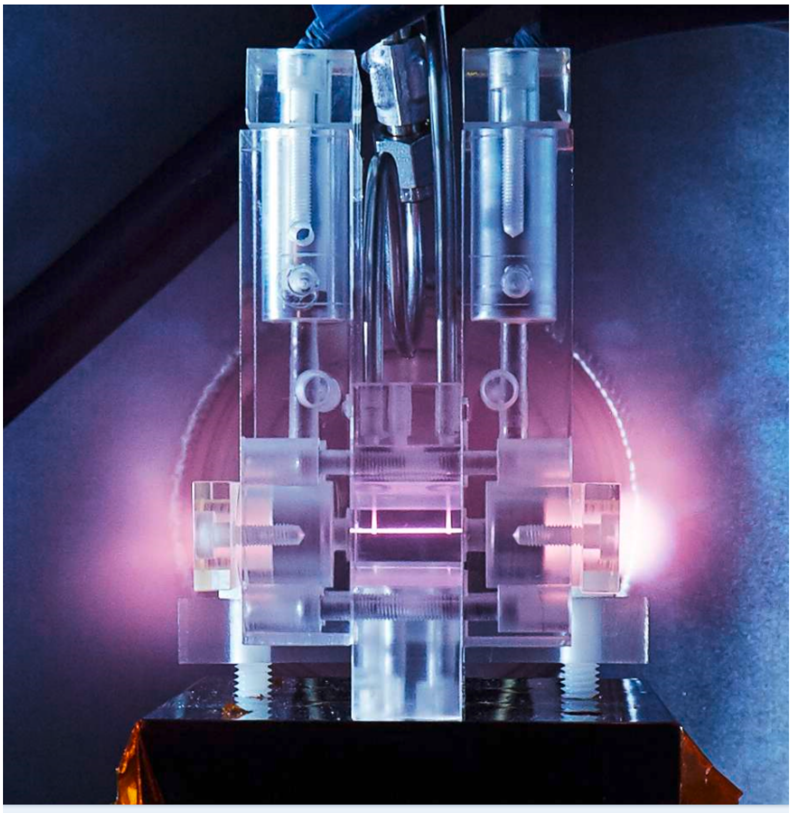

Figure 11: Picture of the APL setup during a discharge. The sapphire block with the plasma channel (shaped like in inverted π) can be seen in the lower centre.

2.1 MAINZ MICROTRON PLASMA-LENS EXPERIMENT

One way of probing the magnetic field in an APL is by letting a well controlled and stable relativistic electron beam interact with it. The Mainz Microtron B (MaMi-B) which is operated by the Institute for Nuclear Physics at the University of Mainz can deliver such a beam [41]. The most important characteristics of the beam are its variable energy between $E = 180 -$

855 MeV (in steps of 15 MeV), with an energy spread of $\sigma_E = 13\,\text{keV}$ at 855 MeV, its low normalized vertical emittance that was measured during the experimental campaign to be $\epsilon_{n,y} = 1.37 \pm 0.01\,\text{mm mrad}$ and its low current of $100\,\mu\text{A}$. For a more detailed description of the accelerator, refer to Appendix B.

2.1.1 *Capillary and gas supply*

The capillary used in all measurements at MaMi-B had the same general setup shown in Fig. 11. The central part consists of two sapphire slabs measuring 15 mm x 20 mm x 4 mm with a half-cylindrical channel machined into the surface as seen in Fig. 12. Two rectangular channels coming from the top are connected to the gas supply and work as inlets. The length of the actual capillary in Fig. 13 is 7 mm with a diameter of 1 mm. In the setups for longer APLs, the same sapphire plates were used but the pockets for the electrodes on both ends were smaller or left out (Fig. 11 shows a 15 mm setup). The electrodes for the 7 mm setup can be seen in Fig. 14. A picture of the setup during discharge can be seen in Fig. 11. The sapphire machining process is described in detail in [42], an image of the 7 mm APL sapphire slab is shown in Fig. 13. A microscopic picture of the channel from the beam's point of view can be seen in Fig. 15.

To estimate the behavior of the current density near the capillary exit and the inlets, several simulations were employed. The results can be found in Sec. 4.2. The hydrogen gas was supplied by a gas system consisting of a mass-flow controller, a buffer volume of 1 l, and a fast shutter. The fast shutter was left open in normal operation and was build in between the buffer volume and the capillary as a safety measure in case one of the turbo molecular pumps were under too much load from the hydrogen. The mass-flow controller was used to fill the buffer volume to the desired pressure. The buffer volume and the capillary are directly connected, so that a constant flow into the capillary is maintained. The mass flow controller was slowly opened during the beamtimes in order to avoid high-pressure shock fronts propagating into the vacuum and damaging the turbo-molecular pumps. The pressure in the buffer volume was set to $p = 5.6\,\text{mbar}$. Taking a pressure drop in the gas supply pipe to the capillary into account, this leads to a gas density of up to $n_0 = 10^{17}\,\text{cm}^{-3}$. For complete ionization of the hydrogen molecules, this results in a plasma density of $n_e = 2 \cdot 10^{17}\,\text{cm}^{-3}$ and a plasma wave number of $k_p = 3 \times 10^4\,\text{m}^{-1}$. The passive plasma focusing (cf. Sec. 1.2.2) for the MaMi-B diagnostic mode beam can be neglected owing to the low beam density in the APL. The shortest substructure of the MaMi-B bunches is $\sigma_z \simeq 10\,\text{cm}$ long due to the RF-frequency, its transversal size is $\sigma_u \simeq 300\,\mu\text{m}$, resulting in a beam density of $n_b = 1.5 \times 10^2\,\text{m}^{-3}$. The ratio between APL focusing gradient and passive plasma focusing is given in equation Eq. (88). Furthermore, the bunch length is much greater than the plasma wavelength, so the effective charge capable of driving a wakefield is reduced even further.

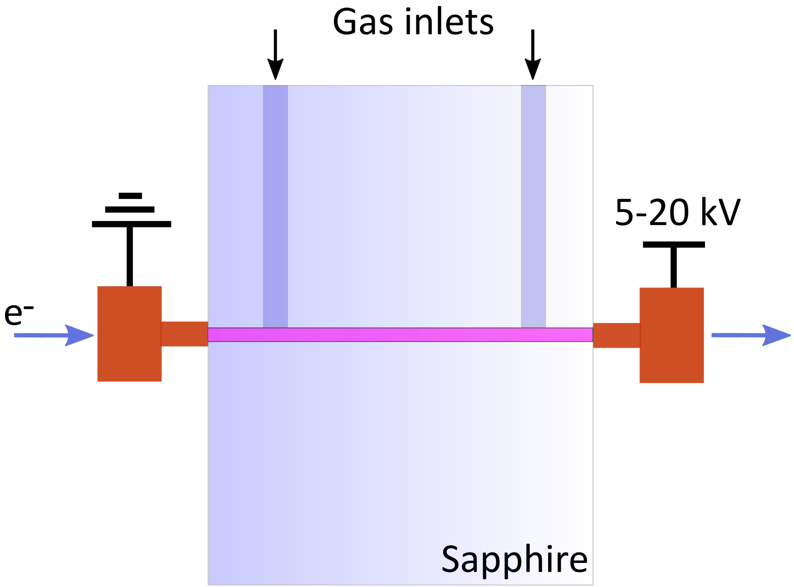

Figure 12: Schematic cross section of the capillary discharge setup.

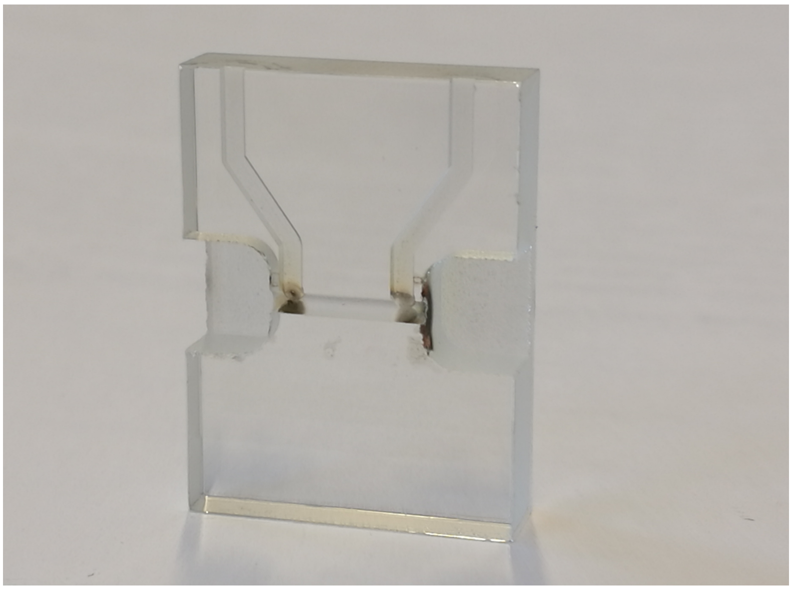

Figure 13: Image of the sapphire plate used for the 7 mm long APL setup. This setup was used during the third measurement campaign for three days of beamtime with some 10^4 discharges fired. The blackening at the ends of the capillary originates from sputtering of the copper electrodes and subsequent coating of the sapphire.

Figure 14: Image of the electrodes used for the 7 mm long APL setup.

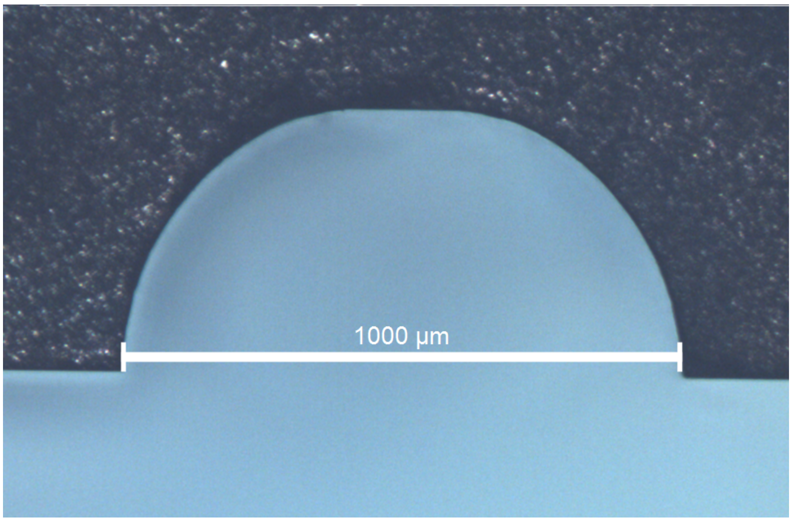

Figure 15: Front view microscopic image of the plasma lens used during the campaigns at the MaMi-B. The sapphire was drilled using diamond-coated drill bits. For more information on sapphire machining refer to [42].

2.1.2 *Discharge*

The pulser used to drive the gas discharge and supply the current forming the APL was designed by the DESY-MIN group as a kicker-magnet driver. The setup consists of a high-voltage (HV) generator charging a pulse-forming network (PFN) [43]. It was optimized for plasma discharge [44]. It is capable of delivering a stable current plateau over ~250 ns - depending on the specific setup. The PFN consists of coaxial cables* that are connected in parallel with 50 Ω impedance each. These coaxial cables serve as capacitors. Depending on the number of cables used as capacitors currents of up to 1 kA can be delivered. Longer cables will result in longer discharge times due to the higher capacity thus higher energy stored and tus longer time constant. The discharge is switched on using a thyratron that can switch with a speed of $\sim 10^{12}$ A/s. The discharge current is connected to the plasma cell using another set of coaxial cables of the same impedance and the same number of cables connected in parallel. To match the impedance of the coaxial cables to the plasma cell, DC resistors are used that have the same resistance as the coaxial cables have impedance, so that R_M=50 Ω/N, where N is the number of cables used. After the resistors, single-wire cables are used to transport the current to the electrodes at the plasma cell which has a resistance of ~5 Ω during the discharge [44]. Before the discharge process the resistance of the plasma cell is nearly infinite, leading to reflection of the initial current pulse. As an additional safety, a bypass resistor R_g=10 MΩ was installed. Owing to the nature of the PFN, the voltage drop on the plasma cell is half the voltage on the DC power supply. The current through the plasma lens is measured via

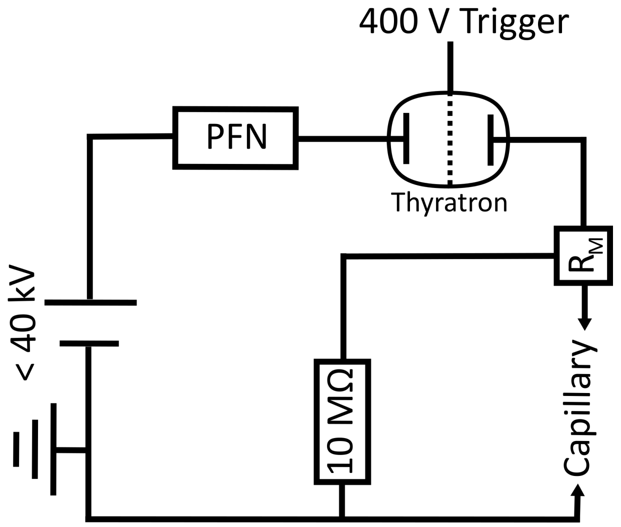

Figure 16: Schematic of the discharge circuit. A DC power supply charges the PFN with up to 40 kV through a bypass current limiting resistor (10 MΩ). Supplying a 400 V trigger voltage to the thyratron relays half the potential difference to the capillary, causing high-voltage breakdown. The DC resistance R_M is used for impedance matching between the PFN and the capillary.

---

* Philips HF-Impulskabel 4.9/17.3 FRNC-Mtl.; C/l~101 pF, Z=50 ± 1 Ω

a Rogowski coil[†] around the ground side of the cable after the impedance matching resistors supplying the current to the APL. The signal from this coil is monitored on an oscilloscope[‡]. A typical discharge current is shown in Fig. 17.

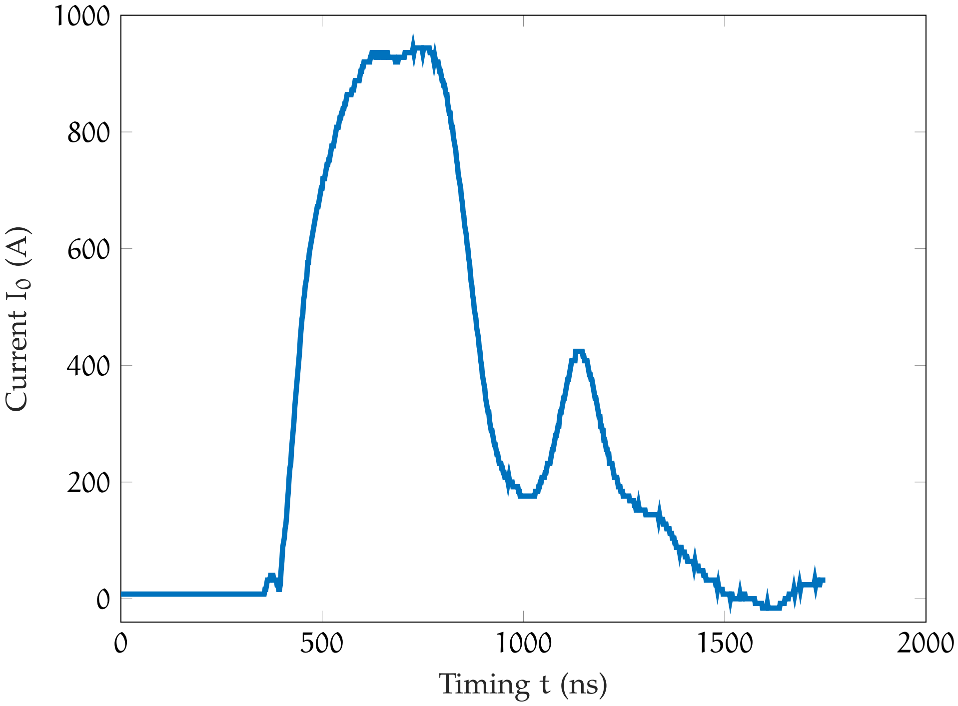

Figure 17: Discharge current profile for a voltage of 30 kV at the PFN and 15 kV at the capillary and three coaxial cables resulting in an overall resistance of $\simeq 17\,\Omega$.

2.1.3 *Beam diagnostics*

The beam diagnostics for all measurements consisted of Lutetium-yttrium oxyorthosilicate (LYSO) plates of 100 or 200 µm thickness respectively that served as scintillators, a telephoto zoom lens[§] for imaging, and an sCMOS camera[¶] for recording. Tab. 2 lists the parameters of LYSO that are of interest. It was chosen for its high light yield and low granularity. The optical setup was designed so that a demagnification of ∼ 2 was realized, leading to each pixel integrating over a space of $\sim 10\,\text{x}\,10\,\mu\text{m}^2$ of the LYSO screen. The resolution of the entire optical setup was ∼ 20 µm. This was sufficiently small so that all beam spots of the measurements in the scope used in this work could be resolved.

The most important features of the chosen camera are its peak quantum efficiency of up to 82% and LYSO-suited spectral range, small pixel size of $6.5\,\text{x}\,6.5\,\mu\text{m}^{2}$, high dynamic range of

---

[†] Pearson current monitor 6595; 2.5 ns rise time, 1 kA maximum current, 0.5 V/A output
[‡] LeCroy WaveSurfer 104MXs-B
[§] Canon 100-400 mm 1:4.5-5.6 EF L IS II USM
[¶] pco.edge 4.2 https://www.pco.de/camera-selector/pcoedge-42/

Table 2: Important parameters of LYSO.

Peak emission (nm)	428
Light Yield (Relative BGO = 100%)	190
Index of refraction (@ 428 nm)	1.82
Decay constant (ns)	40-44

16 bit, and low readout noise of 0.9 e^- per pixel median noise. All of those features enable a good resolution of the relatively small and dim beam spot on the LYSO screen.

2.1.4 *Alignment procedure*

The APL was placed on two linear and two rotational stages to ensure alignment. The two linear stages provided the possibility of transverse movement. The rotational stages allowed for rotation around x and y axes. Due to the rotational symmetry of the APL, no rotation around the beam axis s was necessary.

A first alignment was performed using a laser beam on the electron beam axis. The stray light from the capillary walls was minimized by rotating and translating the APL. Afterward, the electron beam was switched on with the APL in position. The scintillation light from the sapphire was used as another alignment indicator. Driving the APL horizontally and vertically with some remnant angular misalignment would produce scintillation light at one end of the capillary. This was used to further align the capillary with respect to the beam. Afterward, the electron beam clipping was used as an indicator while driving the APL horizontally and vertically, providing a zero transverse position.

Since a linear transverse offset of the APL yields a constant dipole component in the magnetic field B_ϕ, the final alignment was achieved by observing the center of mass (COM) of the electron beam with various APL settings. Here, the two-dimensional (2D) COM is defined as the two mean values of the two intensity distributions of the beam spot integrated over one dimension respectively as defined in Eq. (24). The dipole component will kick an electron beam in the direction of the offset. As long as the lens was misaligned, a dipole kick was introduced. Using a varying current also made sure that no residual angular misalignment was falsely interpreted as a linear offset.

2.1.5 *Direct gradient measurement*

A LYSO-screen placed $\sim 20\,\mathrm{cm}$ behind the APL served as a scintillating screen - see Section 2.1.3. The same mechanism as in the alignment procedure was used to probe the magnetic field dependence with the radial position r. By introducing transverse offsets r_0 to the APL with respect to the beam a COM-shift $\Delta\langle x\rangle$ is achieved. The introduced shift can be written using the Lorentz force from Eq. (2) as

$$\Delta\langle x\rangle = \frac{q\cdot d}{p}\int_0^L B_\phi(r_0)z\mathrm{d}z = \frac{e\cdot d}{p}B_\phi(r_0)\cdot L, \tag{94}$$

in which L is the effective length of the APL, d the distance between the APL center and the screen, $q = e$ the electron's charge, and p its momentum. Here the assumption of paraxial motion in the APL is used, which assumes that there is no significant change in particle position over the length of the lens, but rather a change in momentum (direction). Additionally $\int_0^{L_{\mathrm{mag}}} B_\phi(r,z) = \int_0^L B_\phi(r)$ is used, so the longitudinal magnetic field evolution is replaced with a box-shaped magnetic field. The length of this box is chosen so that the integrated field is the same in both cases. This is why L is not the actual, but rather the *effective* length.

2.1.6 *Emittance measurement*

In order to measure the transverse emittance change of the MaMi-B beam introduced by an APL, a quadrupole scan was performed. The beamline used for this measurement can be seen in Fig. 18. The QMs in front of the APL were supplied by Bruker. The QMs after the APL and the dipole magnet were previously used in a positron system at the University of Mainz and were build by MPI. They have been measured and tested in [45]. The relevant features of both types of QMs can be found in Tab. 8 in Appendix B. The dipole in the beamline is also refurbished and is a sector dipole with a design bending angle of 30°. It is used as a 44° bending dipole, therefore introducing edge-focusing - see Appendix A. All scans were performed in vertical direction, avoiding the dispersion introduced by the dipole. Since the energy spread of MaMi-B is on the 10^{-5}-level, little horizontal beam size increase was introduced at the screen position by the dispersion. This is also an indication for the absence of wakefields. Wakefields introduce an energy modulation that would have broadened the beam size in the dispersive plane significantly.

To probe differences in emittance degradation depending on the incoming beam size and divergence, two settings for the beamline quadrupoles were used. For one setting, the quadrupoles were turned off. The beam coming from MaMi-B has a divergence of $y'_{\mathrm{rms}}x'_{\mathrm{rms}} \leqslant 0.1$ mrad and a beam size of $x_{\mathrm{rms}} = 151^{+2}_{-12}$ µm and $y_{\mathrm{rms}} = 154^{+5}_{-15}$ µm rms. For the second setting, the QMs were tuned so that the beam was focused in both dimensions inside the plasma lens itself. This resulted in a beam size of $x_{\mathrm{rms}} = 88^{+2}_{-12}$ µm and $y_{\mathrm{rms}} = 114^{+5}_{-15}$ µm rms.

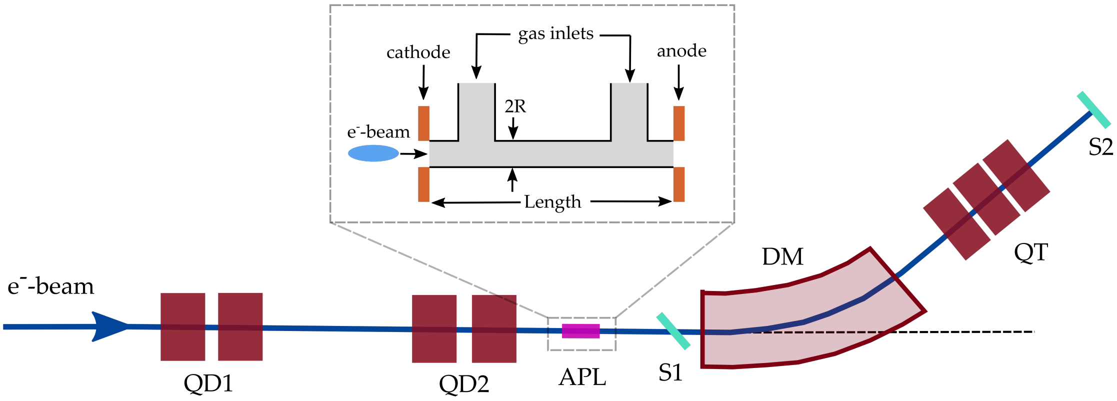

Figure 18: Schematic of the accelerator beamline at MaMi-B. QD1: first quadrupole duplet; QD2: second quadrupole duplet; APL: active plasma lens; S1: screen used in the offset measurements; DM: dipole magnet; QT: quadrupole triplet used in the emittance measurements; S2: screen used in the emittance measurements.

The *CLEAR Plasma Lens Experiment* is a collaborative experiment at the CERN Linear Electron Accelerator for Research (CLEAR, cf. Fig. 19) with a similar scope to the *Mainz Microtron Plasma Lens Experiment* [32]. It is a collaboration between the University of Oslo (responsible for the experimental design and scope), University of Oxford (responsible for supplying the discharge unit in the form of a *Compact Marx Bank*), and DESY (responsible for supplying the capillary including holder, the gas supply connection to the holder, and electrode design). All of the parts DESY supplied were developed in the scope of this work and can be seen in Fig. 20.

The design of the APL used in this experiment is similar to the one used in Mainz. The sapphire plates used to form the capillary are drilled with round drill bits of the desired diameter. The drilled channel is one radius deep so that two plates form a round channel. The gas inlets are fed through the back of one plate and through the plastic holder so that a long gas column is formed in the holder. This prevents breakdown through the gas supply system. A successful breakdown can be seen in Fig. 21. An important difference between the APL setups used at MaMi-B and CLEAR is the fact that the inlet channels extend further than the capillary and are drilled deeper into the sapphire than the radius of the capillary. This design was chosen to ensure a high degree of azimuthal symmetry. Additionally, in the CLEAR experiment different gas species with different values of σ_0 and κ_0 in Eq. (71) were used. The thermal steady state forms differently for different gas species, favoring heavier elements because of their lower thermal conductivity. A lower thermal conductivity leads to a longer time window in which a uniform current density is present, enabling emittance preserving focusing in APLs (cf. Sec.1.2.1).

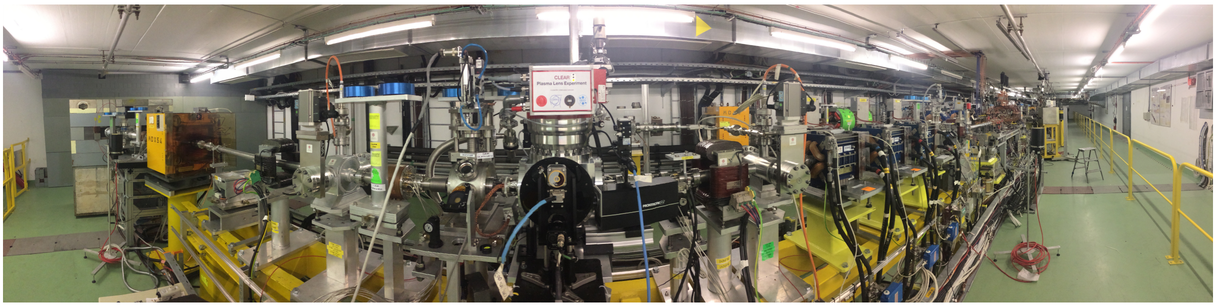

Figure 19: Image of the CLEAR beamline used for the APL experiments. The central chamber contains the APL and is placed on a mover.

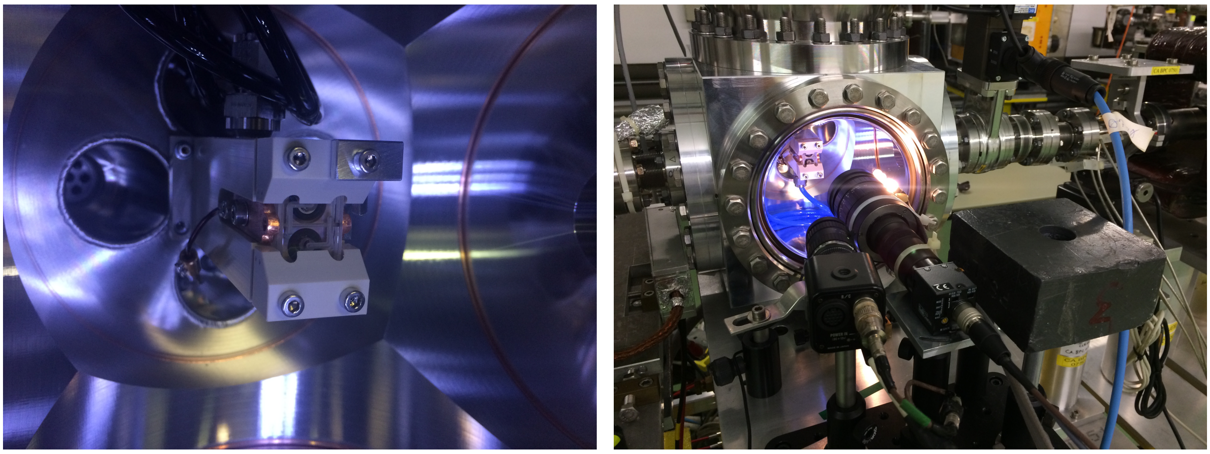

Figure 20: Images of the CLEAR plasma lens setup. The sapphire plates are the central part of the setup, wedged between copper electrodes. The left image shows a close-up image of the plasma lens. The right image shows the vacuum chamber with a side-view window of the plasma lens.

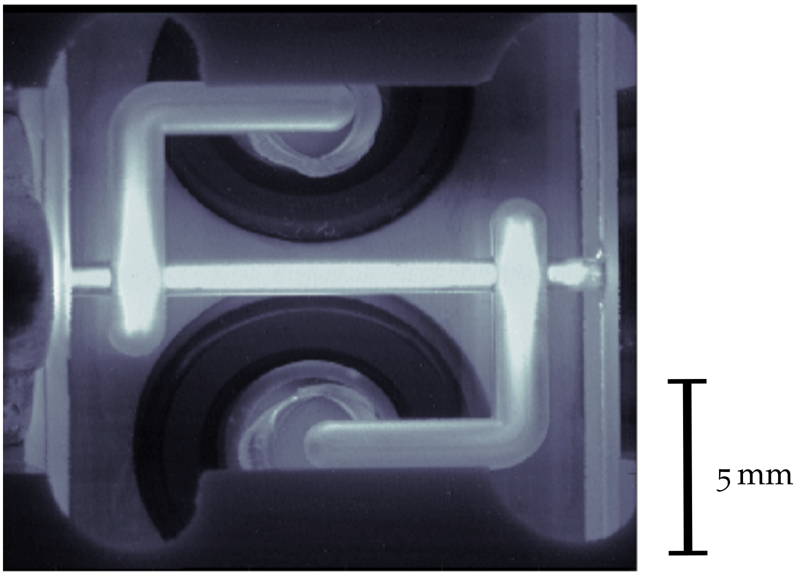

Figure 21: Image of the sapphire design that ensures breakdown occurs only through the central capillary by separating the gas inlets. The visible light is from plasma recombination.

3

RESULTS

This chapter describes the results obtained in the experimental campaigns designed to probe the field quality of APLs. First, the results from the *Mainz Plasma Lens Experiment* campaigns are given which were the main campaigns undertaken in the scope for this work. Results from the collaborative experimental campaign at CERN, the *CLEAR Plasma Lens Experiment*, will also be briefly described and have been published in [46].

3.1 MAINZ PLASMA LENS EXPERIMENT

This section illustrates the results of the Mainz Plasma Lens Experiment described in chapter 2 and performed at MaMi-B. First the results obtained by varying the temporal delay between the arrival of the electron bunch and the discharge of the plasma column using the technique from Sec 2.1.2 are described. The results shed a light on the stability and shot-to-shot fluctuations of the APL setup used in the campaigns. In the following, the results of offset scans explained in Sec. 2.1.5 are shown. These give an insight to the magnetic field behavior in the lens as a function of radial position. The third section describes the results of emittance measurements using quadrupole scans (cf. Sec. 2.1.6). The emittance evolution of beams passing APLs is a crucial figure of merit for their applicability in plasma accelerators. During all campaigns and measurements, the APL diameter was 1 mm.

3.1.1 *Shot-to-shot fluctuations and temporal stability measurements*

During all campaigns, MaMi was operated in the so-called *diagnostic bunch mode* described in Appendix B which delivers 10 ns long bunches. This is the shortest bunch length available at MaMi. For the purpose of probing an APL for its capability of capturing beams from plasma accelerators, bunches as short as a few femtoseconds would be ideal. Owing to the nature of the discharge current, which is stable over a period of ~ 200 ns, however, these relatively long bunches did not negatively impact the measurements, so long as the bunch experienced a constant focusing strength over its entire length. The arrival times of the electron bunch with respect to the discharge current are shown in Fig. 23.

As a first test, the timing between discharge current and electron bunch arrival was varied. For this, the beam diagnostic was set up as described in Sec. 2.1.5. The distance between APL center and screen varied between the campaigns from 17 cm to 23.5 cm. The beam spot was recorded and its size changed significantly when temporal overlap of the discharge current and the electron beam was achieved. Also, the shot-to-shot stability of the beam size decreased significantly when the electron bunch was on or near the discharge current ramps - this is

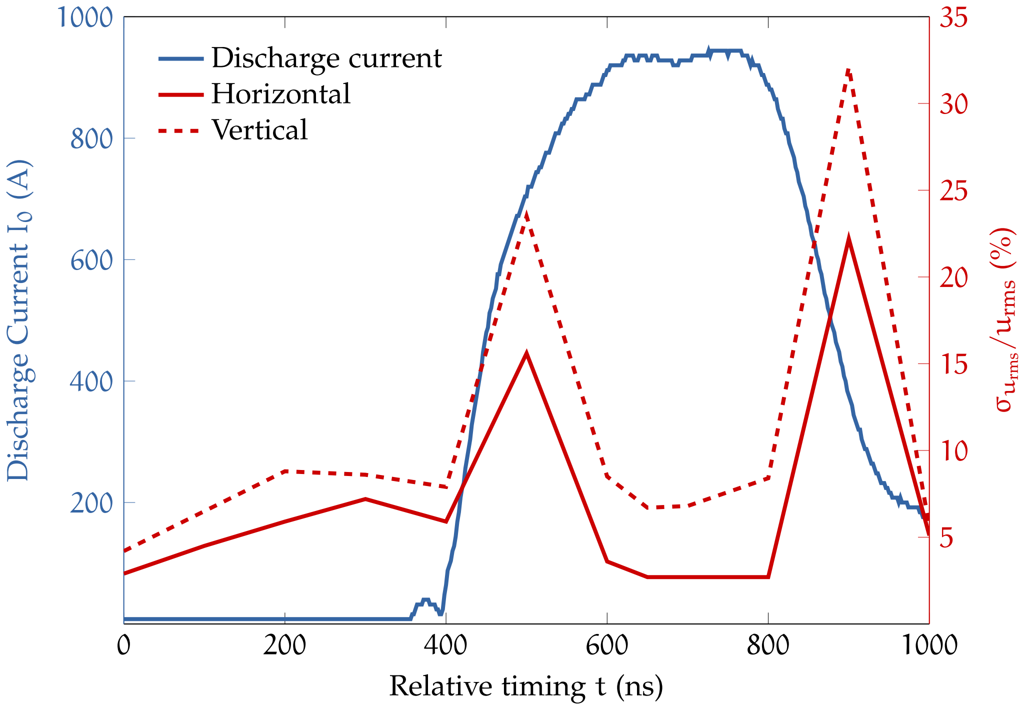

Figure 22: Dependence of the rms beam size stability $\sigma_{u_{rms}}$ relative to the mean beam size u_{rms} on the timing between discharge current and electron arrival time.

Table 3: rms beam size for different delay settings between electron bunch and discharge. Error also given in percent of the respective beam size. The electron bunch was on top of the discharge current plateau between 600 ns and 800 ns. This data was taken with a 50 ns rms timing jitter of the electron bunch present.

Relative timing (ns)	x_{rms} (μm)	$\sigma_{x_{rms}}/x_{rms}$ (%)	y_{rms} (μm)	$\sigma_{y_{rms}}/y_{rms}$ (%)
0	75.9 ± 2.2	2.9	150.3 ± 6.4	4.2
100	73.2 ± 3.3	4.5	139.3 ± 9.1	6.5
200	68 ± 4	5.9	126.6 ± 11.1	8.8
300	74 ± 5.3	7.2	138.6 ± 11.9	8.6
400	75.8 ± 4.5	5.9	140.7 ± 11	7.9
500	60.5 ± 9.4	15.6	104.1 ± 24.5	23.5
600	50.5 ± 1.8	3.6	75.6 ± 6.4	8.5
650	49.3 ± 1.3	2.7	71.3 ± 4.8	6.7
700	49 ± 1.3	2.7	68.3 ± 4.6	6.8
800	49 ± 18	2.7	69.3 ± 5.8	8.4
900	61.8 ± 13.7	22.2	107.4 ± 34.5	32.1
1000	82.8 ± 4.2	5.1	155.8 ± 8.7	5.6

Table 4: Stability analysis of beam COM and rms beam size for different timings between discharge and electron bunch. Error also given in percent of the respective beam size. The timings correspond to the ones shown in Fig. 23.

Current (A)	Delay (ns)	$\sigma_{\langle x\rangle}$		$\sigma_{\langle y\rangle}$		$\sigma_{x_{rms}}$		$\sigma_{y_{rms}}$	
0	-	17 µm	19 %	23 µm	22 %	1.4 µm	1.6 %	5.1 µm	5 %
404	0	14 µm	20 %	13 µm	22 %	1.3 µm	1.9 %	2.3 µm	3.8 %
404	160	14 µm	20 %	11 µm	19 %	1.5 µm	2 %	2.3 µm	3.8 %
404	240	14 µm	20 %	13 µm	20 %	1.4 µm	2 %	2.9 µm	4.3 %

clearly visible in Fig. 22. The instability was worst during the first campaign where a timing jitter of the electron bunch arrival on the order of 50 ns rms was present. This jitter was removed in the later campaigns. Tab. 3 shows the results of a timing scan during the first campaign.

During the third campaign, in which there was no electron arrival-time jitter present, measurements for different time delays were also performed. The timing of these measurements can be found in Fig. 23. Most scans were performed with a middle timing (160 ns delay in Fig. 23). The stability of the APL for the three settings is shown in Tab. 4. It can be seen that the APL was very stable, in fact so much so that no clear evidence of a gradient jitter could be found. No measurements were performed investigating the behavior on the current ramps during the third campaign.

In order to assess the shot-to-shot stability of the APL, the fluctuations of the beam position $\langle x\rangle$ with and without the APL were analyzed. To probe for the maximum effect, the APL was offset in the x-axis by 350 µm. In this configuration, fluctuations of the focusing strength are translated into fluctuations of the beam position. For this measurement, 100 consecutive shots were recorded. The y-axis of each camera image was summed up to create an intensity profile for the x-axis. The integrated lines are shown next to one another in Fig. 24 for the results of the measurements using the APL with 350 µm offset. In this way, the relevant fluctuations are made visible while showing all 100 shots in one plot. Fig. 25 is of the same form while showing the results without an APL in the beamline. It is immediately obvious that the APL did not introduce any additional fluctuations which is a very promising result for future applications of the APL.

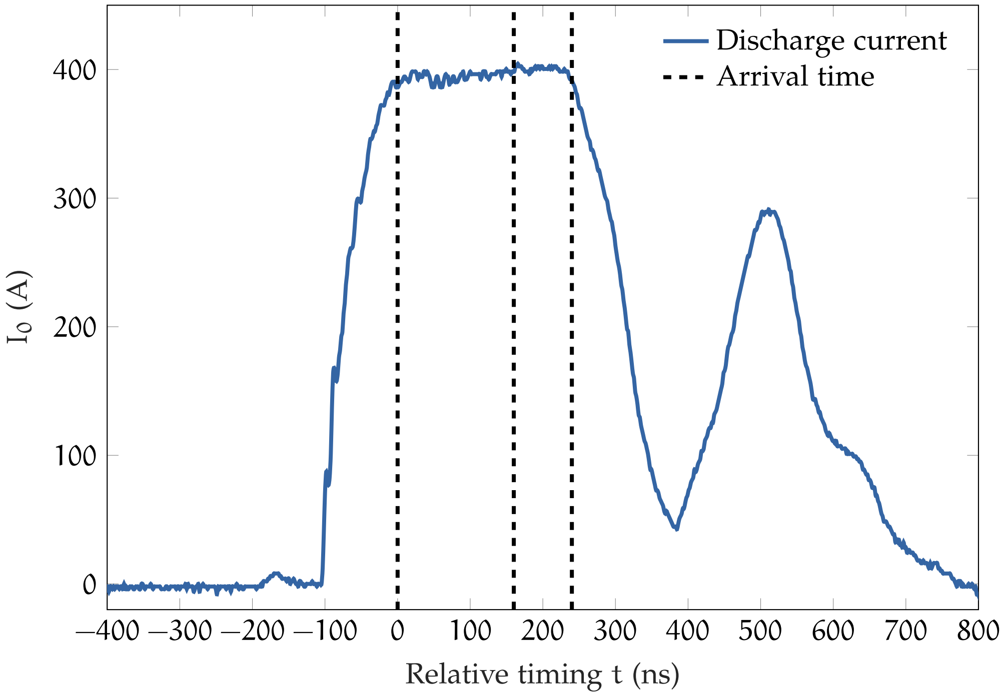

Figure 23: Discharge current and electron arrival time for the three different settings used during the campaign. The delay times correspond to 0, 160, and 240 ns.

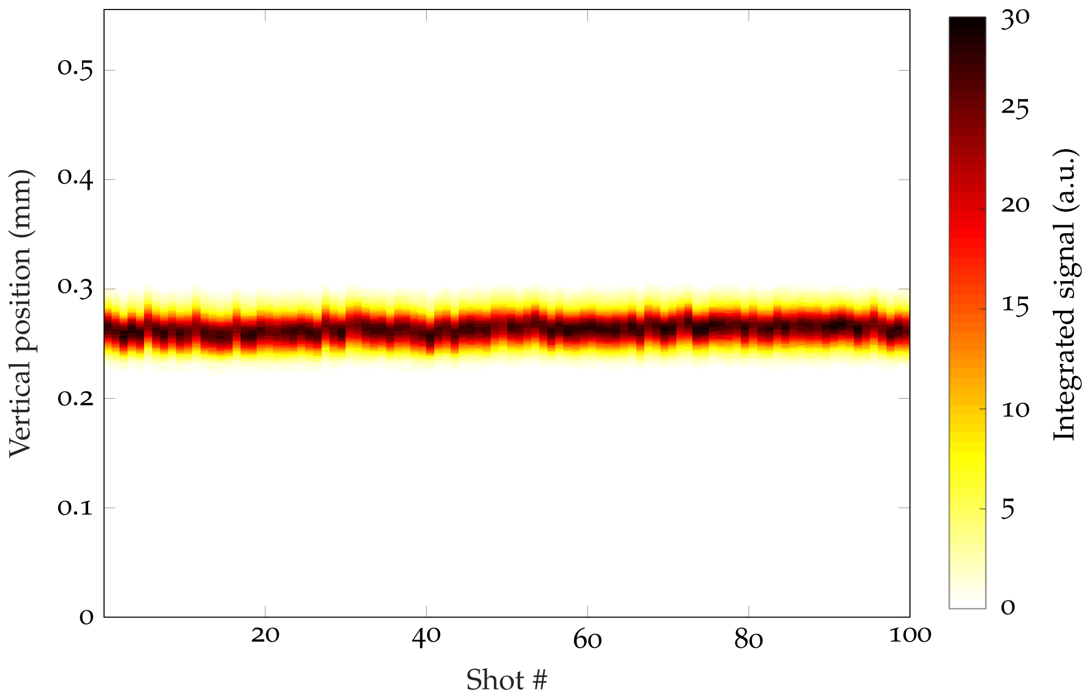

Figure 24: Vertically projected camera signal for 100 consecutive shots and 350 µm APL offset. The shot-to-shot fluctuation of the beam position was not affected by the APL in a statistically significant way.

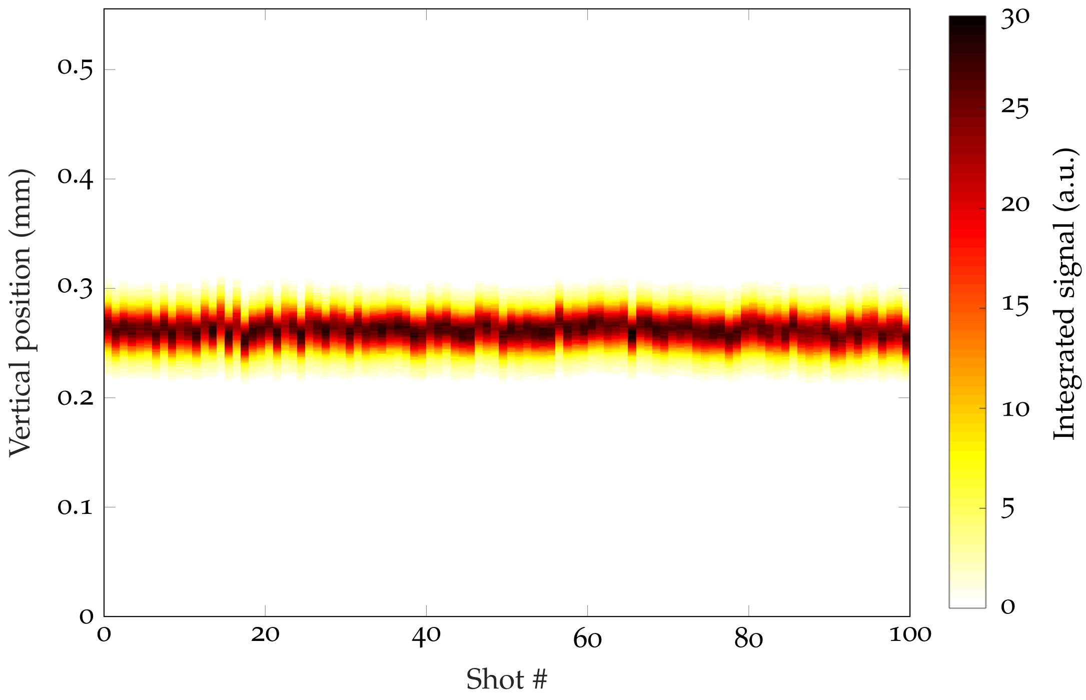

Figure 25: Vertically projected camera signal for 100 consecutive shots with no APL in the beamline.

3.1.2 *Direct magnetic field measurement*

A direct measurement of the magnetic field in the APL was achieved by introducing a transverse offset r_0 to the APL and measuring the shift of the spot on the LYSO screen $\sim 20\,\mathrm{cm}$ downstream. The shift in beam position $\Delta\langle x\rangle$ is introduced by the resulting dipole kick as described in Sec. 2.1.5. According to Eq. 94, there are several factors influencing $\Delta\langle x\rangle$ apart from $B_\phi(r_0)$. For one, $\Delta\langle x\rangle$ is linearly dependent on the effective length of the APL L. Owing to fringe fields forming at the exits of the capillary, the effective magnetic length $L = L_{cap} + 2 \cdot L_{fringe}$ of the APL extends beyond the sapphire capillary itself. Estimating the effective fringe-field length, L_{fringe} is an important part of the data analysis for the offset measurements, especially for shorter capillaries in which a given fringe-field length will have a higher relative impact. The results of simulations employed to estimate this effect are provided in Sec. 4.2. The simulations predict $L_{fringe} = 0.25\,\mathrm{mm}$. This value is used in the analysis of Figures 27 to add a systematic error which accounts for a range of $L_{fringe} = 0 - 0.5\,\mathrm{mm}$. This error is also provided separately in in Tab. 5. The capillary length was 7 mm for the presented results. The distance d was measured with a precision of $\sim 0.5\,\mathrm{mm}$, this uncertainty is taken into account and is given in the statistical error of the derived value. For the purpose of capturing a beam with the lens, the integrated magnetic field $\int_0^L B_\phi \, dz$ is more important than its actual value. The beam offset measurements described in this section are a direct measurement of this quantity, as can be seen in Eq. (94). Due to the nature of MaMi-B, the error on p is very small: on the order of 10^{-5}. Thus this error is disregarded. The offset r_0 is introduced using motorized translation stages with encoders which results in an accuracy at the 1% level.

For the direct field measurements, the electron beam was focused into the plasma lens to avoid clipping of the beam on the sapphire. This resulted in a maximum offset without charge loss of 350 µm. Fig. 26 shows the integrated light intensity on the screen, which is proportional to the charge for the 7 mm long APL. In the case of 188 A and 364 A, the maximum negative offset (-350 µm) was omitted, while for 740 A the focusing was strong enough to guide the beam through the APL without clipping. As described in Section 1.2.1, a nonuniform current density leading to nonlinear focusing fields will form inside the capillary. This nonlinearity is only visible in the outer region of the APL, where r is close to R. For relatively low nonlinearity, or in terms of the $J \sim T^{3/2}$-model, uniform temperature, a deviation from a linear fit cannot be resolved from the scan. However the ratio of the core magnetic field gradient g_{core} and the uniform case gradient g_{ideal} provides the information of the nonlinearity via $g_{core}/g_{ideal} = u(0)^{3/7}/2m_I = \Delta g$ - see Eq. (80). The results of the offset scans can be found in Fig. 27. It shows the results for three of the four currents used in the experiment. The missing data set for $I_0 = 368\,\mathrm{A}$ is almost identical to the $I_0 = 364\,\mathrm{A}$ data set and is not shown for the sake of clarity. The fitted gradient for $I_0 = 368\,\mathrm{A}$ is $g = 441 \pm 5\,\mathrm{T/m}$ with an additional uncertainty of $\sigma_{\Delta g,\mathrm{Fringe}} = 30\,\mathrm{T/m}$. The gradient increase factors for different currents under the assumption of $L_{fringe} = 0.25\,\mathrm{mm}$ are shown in Tab. 5.

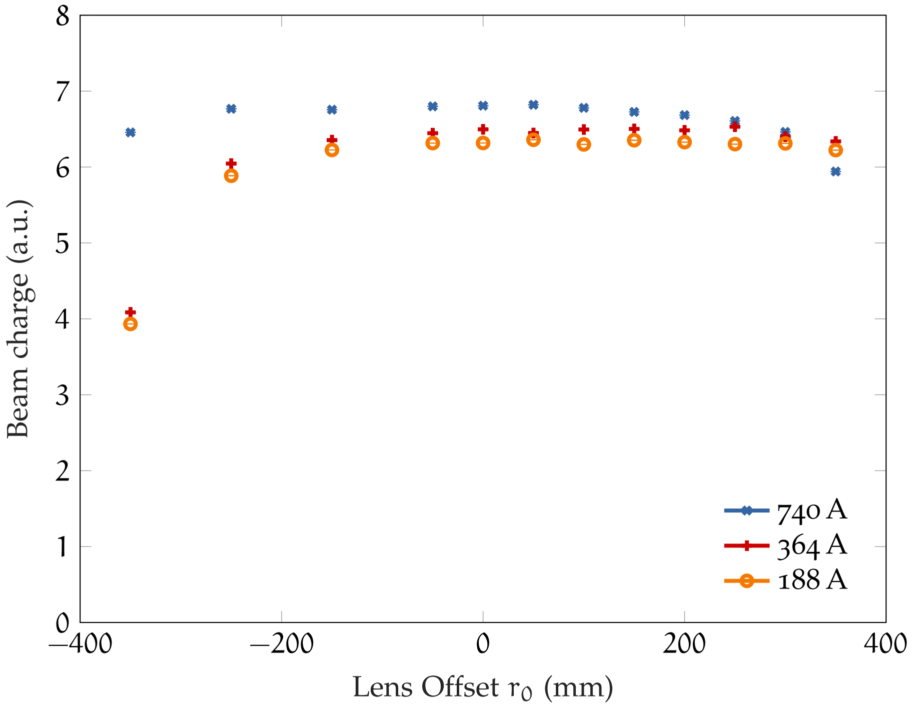

Figure 26: Integrated charge for different APL offsets. Significant charge loss is seen for -350 µm offset and 188 A as well as 364 A current. For the 740 A scan, the plasma lens was strong enough to focus the beam before it clipped on the wall.

Table 5: Gradient increase Δg for offset scans at the same discharge timing. The additional error $\sigma_{\Delta g,\mathrm{Fringe}}$ accounts for the uncertainty of the fringe-field length.

Current (A)	Δg	$\sigma_{\Delta g,\mathrm{Fringe}}$
188	1.58 ± 0.07	0.11
364	1.47 ± 0.02	0.10
368	1.50 ± 0.02	0.10
740	1.37 ± 0.01	0.09

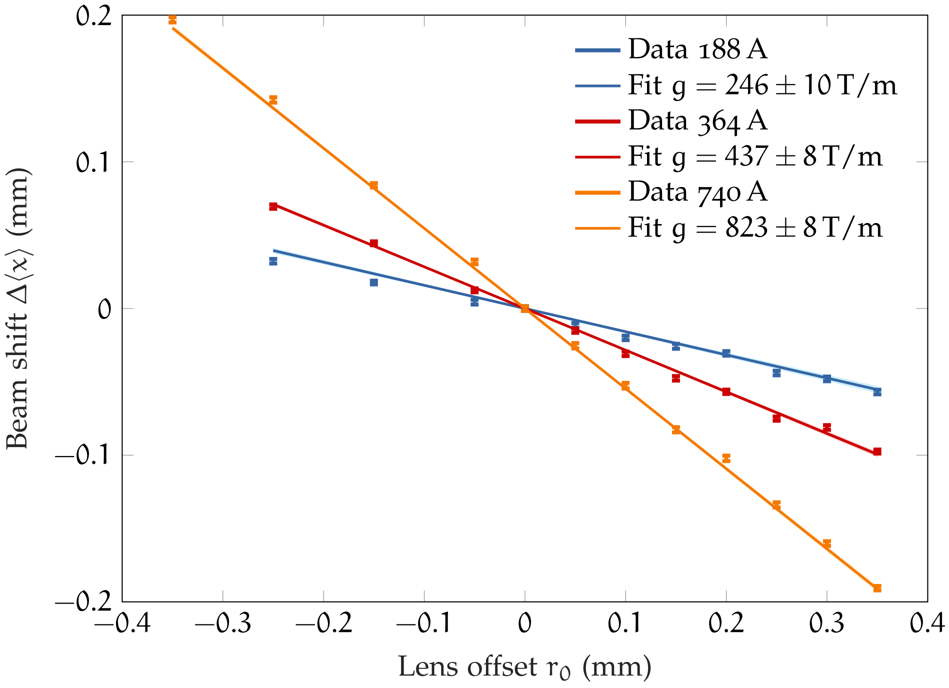

Figure 27: Measured beam position as a function of the APL offset. The error bars indicate the standard error of the mean (SEM) of the COM for 100 shots. The lines corresponds to a linear fit with the 95% confidence interval shown in light colors. The additional systematic uncertainty from fringe fields can be found in Tab. 5.

In addition to scans using a fixed current and scanning the transverse position of the lens, scans using a fixed position and a varying current were performed. Since the APL gradient increases linearly with current, the dipole kick the beam experiences at a fixed offset also increases linearly with current. So these scans are more likely to unveil current dependent anomalies.

Fig. 28 shows the results of a scan using the maximum realizable offset of 300 µm. The results show a deviation for higher currents towards a greater beam shift. This indicates that the gradient increase factor Δg increases with the current. Since the core gradient increase factor Δg is a measure of the nonlinearity through $\Delta g = u(0)^{3/7}/2m_I$ and Eq. (80), the results in Tab. 5 may provide a helpful guide for finding the APL setup with least nonlinearity. It is, however, noteworthy that the different scan approaches, offset and current, give different results for the lower current regime. Further scans are necessary in order to reliably probe the effects.

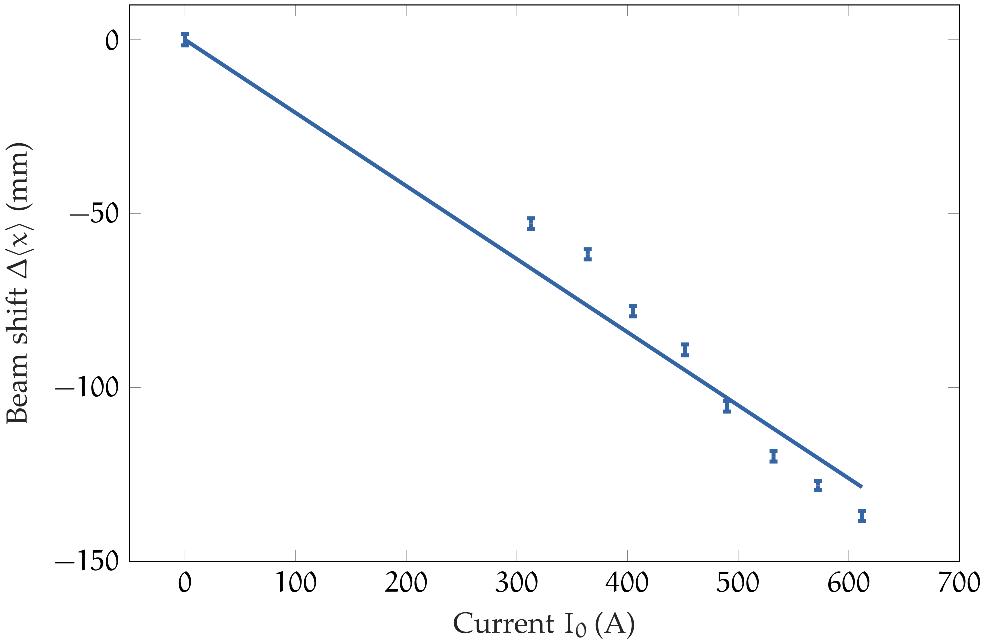

Figure 28: Measured beam position as a function of the APL current. The error bars indicate the standard error of the mean (SEM) of the COM for 100 shots. The transverse APL offset was 300 µm.

3.1.3 *Emittance measurements*

During the third campaign at MaMi-B, quadrupole scans were performed as discussed in section 2.1.6. The same capillary was used as in the offset scans - 7 mm long with a diameter of 1 mm. The recorded beam spots on the LYSO screen were filtered with a background subtraction filter yielding images as seen in Fig. 29. The beam size analysis was achieved by projecting the image onto the vertical axis - see in Fig. 30 - and calculating the rms width of the peak using Eq. (28) and Eq. (27).

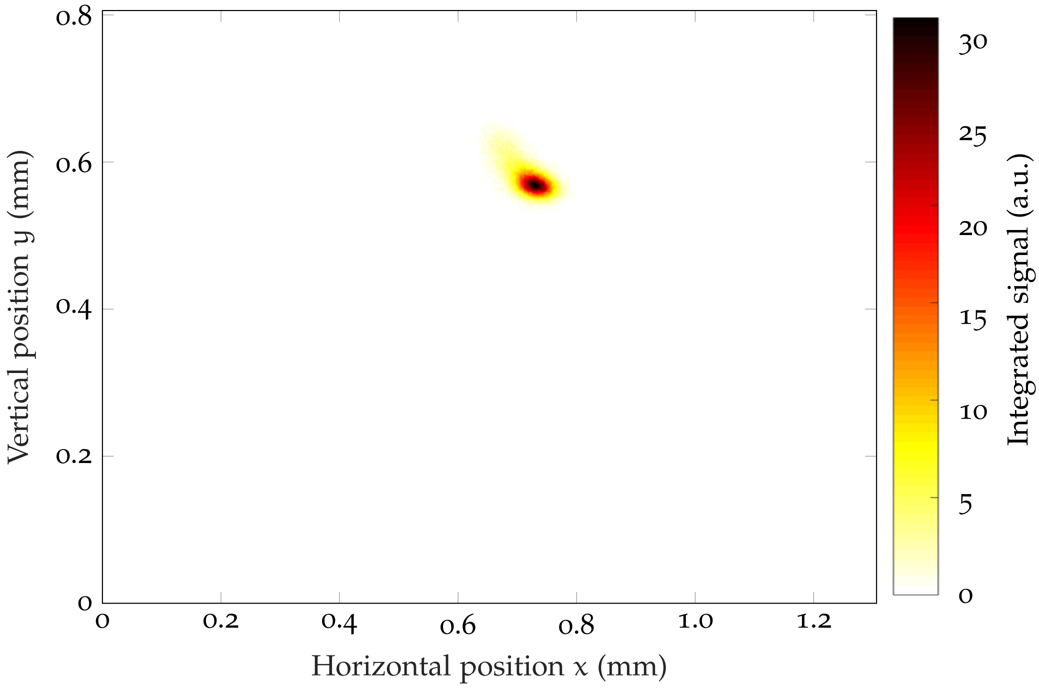

Figure 29: Typical image of the beam spot after background subtraction.

One way of making sure the emittance fit from Eq. (34) represents the beam parameters as well as possible is to take several measurements close to the QM setting where the beam size is smallest - the waist. A typical beam spot in the waist is shown in Fig. 31 with projections in Fig. 32. The fact that there is no 'rotation' of the beam from Fig. 29 to 31 illustrates that there is no $x-y$-coupling in the scan. However, the fact that the beam COM moved when the QM strength was changed points toward the fact that the beam did not traverse the QM through the center. The effect was, however, minor and does not affect the quality of the scans in this case.

Each scan involved at least 8 different QM current settings. For each of those settings 100 images were recorded, filtered, and analyzed as explained above. The mean rms width and standard error for each QM setting were used to determine the emittance using Eq. (34) and Eq. (35). In order to avoid errors regarding the transfer matrix elements R_{ij}, the beamline dimensions as well as the response of the QMs to applied current were measured. The results of the QM measurements can be found in Appendix B.

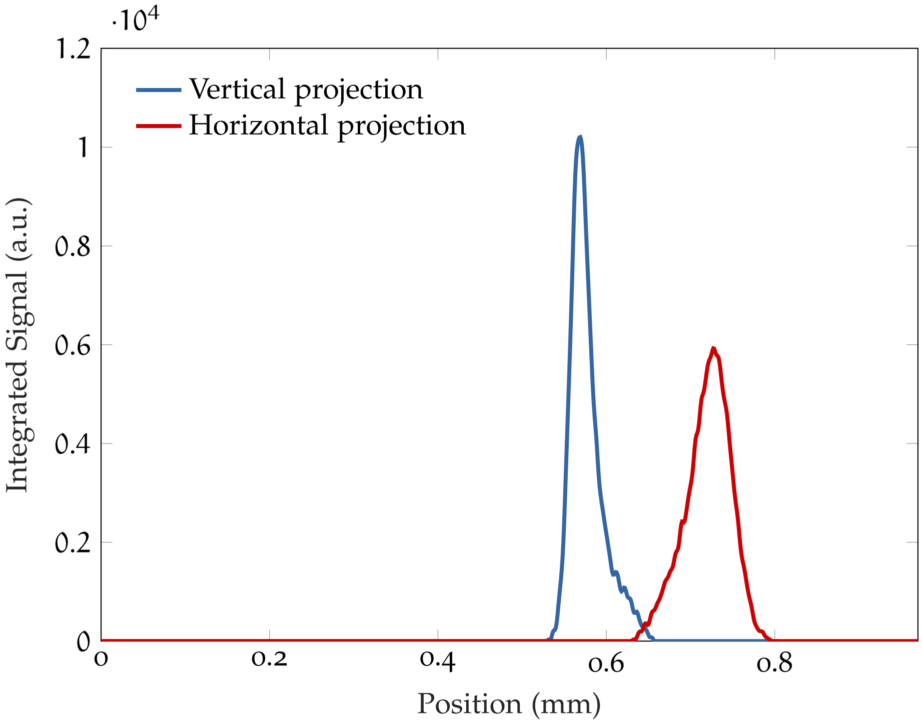

Figure 30: Projection of the beam spot from Fig. 29 onto the two axes.

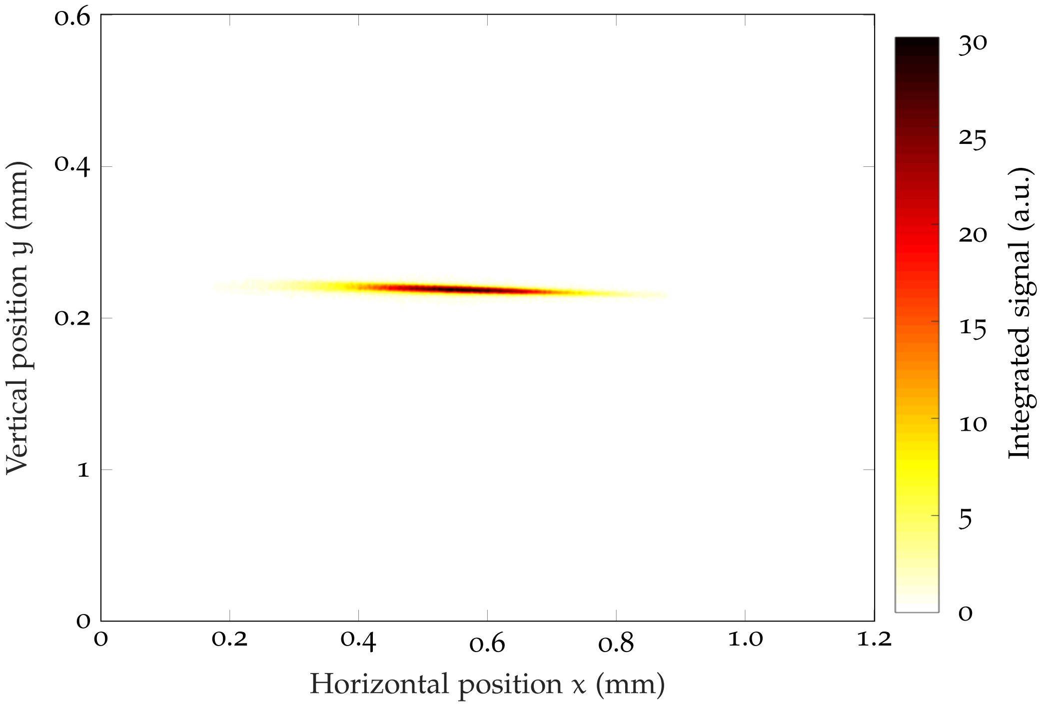

Figure 31: Camera image of the beam spot with minimum vertical size after background subtraction.

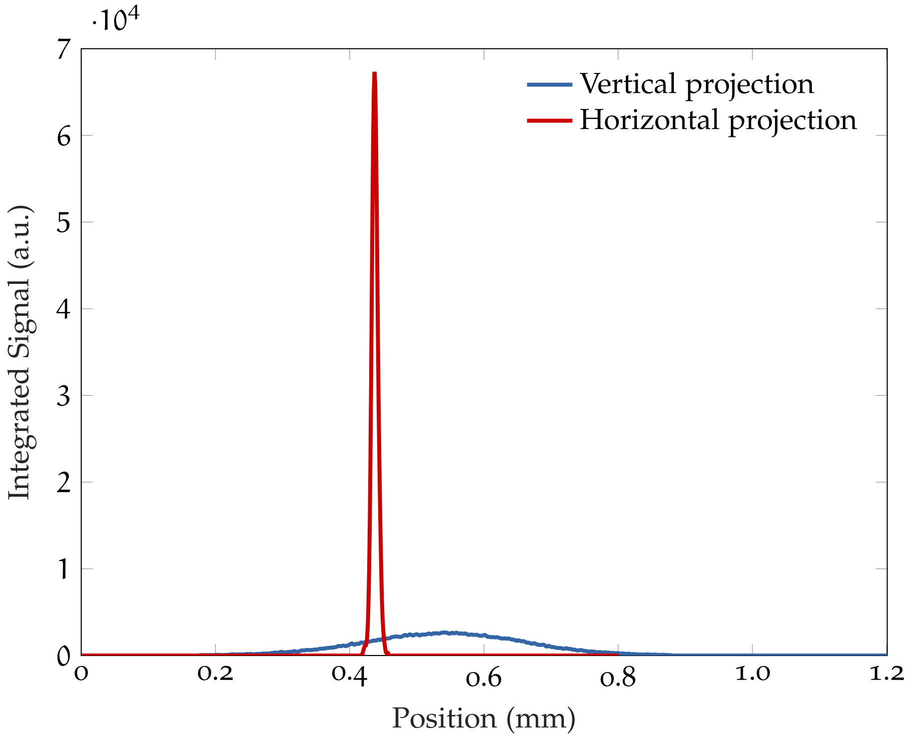

Figure 32: Projection of the beam spot from Fig. 31 onto the two axes.

One crucial parameter to monitor is the integrated signal on the screen which is an indicator of charge loss. Any charge loss in between the APL and the screen may result in an emittance decrease of the remaining beam since particles with the greatest offset from the reference orbit are the ones that are most likely to be lost. The scan using the small beam size with $I_0 = 188\,\mathrm{A}$ APL current showed charge loss and is therefore disregarded in the following.

Fig. 33 shows the results of the quadrupole scans using the $L_{cap} = 7\,\mathrm{mm}$ long APL. The data points are the mean values of the 100 shots that were recorded for each setting with the error bars indicating the standard error of the mean. The lines correspond to the respective fits using Eq (34). The emittances that these fits correspond to can be found in Tab. 6.

The emittance measurements are essentially measurements of the beam matrix as described in Sec. 1.1.4. So with the entire beamline up to the first beamline QM known, it is possible to follow the beam parameter backwards through the beamline. The beam size according to this backtracking along the beamline up to the first screen used in the offset measurements is shown in Fig. 34 for both QM settings. The measured beam sizes on the first screen are in good agreement with these backtracking results - cf. Sec. 2.1.6. This is a proof of the high reliability of the emittance measurements.

3.1.4 *Additional results*

Apart from the 7 mm long capillary, a 15 mm long version was used, the results of which will be presented in this section. They show a systematic deviation from both the 7 mm capillary

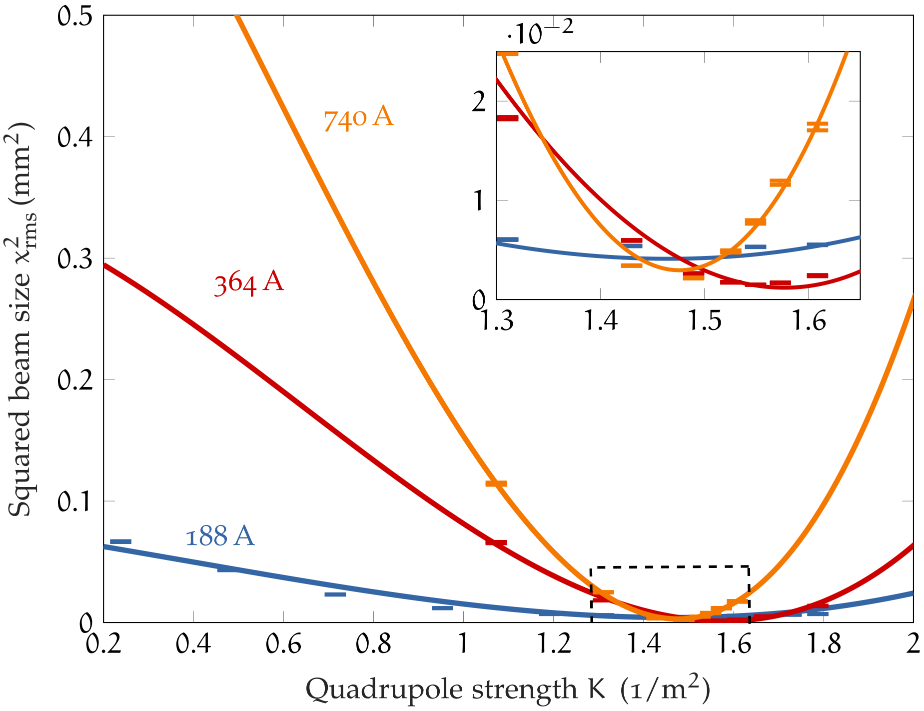

Figure 33: Quadrupole scan results with 7 mm long APL operated at three different currents. The corresponding emittances can be found in Tab. 6.

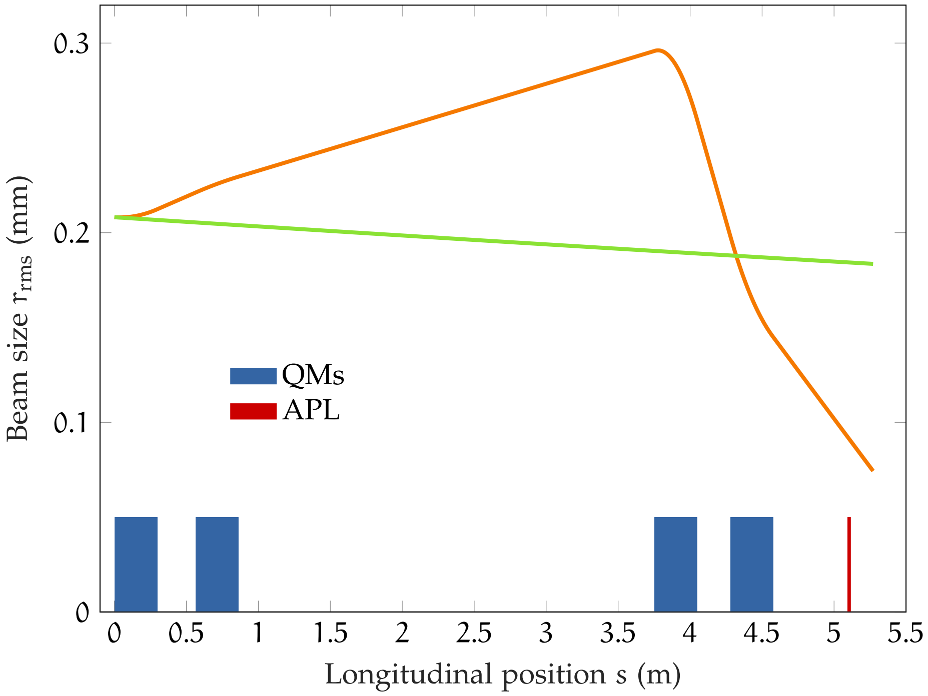

Figure 34: Vertical beam sizes r_{rms} along the beamline in front of the APL and up to the screen used in the offset measurement for the two QM settings used during the campaign. The beam size with all QMs off is shown in green, the one with overall focusing on the screen in orange.

setup as well as the $J \sim T^{3/2}$-model. After an overview of the most relevant results, this section will provide a possible explanation on the origin of this deviation.

It has to be noted that the 15 mm setup was as stable as the 7 mm setup and during the experimental campaign there was no immediate evidence of any error. The capillary was aligned using the same technique as the 7 mm version (cf. Sec. 2.1.4). Subsequently, direct field measurements were performed with it. These measurements were, however, performed at a fixed APL current of $I_0 = 404\,\mathrm{A}$ and with varying electron-arrival-time delay. Figures 35 - 37 show the results of this temporally resolved gradient measurement. These measurements were initially used to find the optimum delay between the discharge and the electron beam. Fig. 35 shows the results of a gradient scan performed with a delay chosen in such a way that the electron beam arrived at the earliest possible point of the stable current plateau. This is defined as $0\,\mathrm{ns}$ delay. The result shows that the core gradient for this timing was less than what is expected for the applied current. The gradient of $g = 252 \pm 5\,\mathrm{T/m}$ corresponds to a gradient increase factor of $\Delta g = 0.78 \pm 0.02$. This effect is also visible in the simulation results in Sec. 4.1 in Fig. 43. During the earliest phase of the discharge, the conductivity appears to be highest near the capillary wall and lowest in the center of the capillary leading to a higher current density near the wall. This leads to a lower focusing gradient in the center. Fig. 36 shows the results of the offset measurement for a delay of 160 ns which was chosen because it was well in the middle of the most stable regime. Fig. 37 shows the result for the greatest delay (240 ns) which resulted in stable focusing. The gradients of $g = 342 \pm 22\,\mathrm{T/m}$ (160 ns) and $g = 336 \pm 2\,\mathrm{T/m}$ (240 ns) correspond to a gradient increase factors of $\Delta g = 1.06 \pm 0.07$ and $\Delta g = 1.04 \pm 0.01$ respectively, which is identical within the margin of error. In contrast to the 7 mm capillary (cf. Fig. 28), the results of fixed offset scans using the 15 mm APL in Fig. 38 show an almost perfectly linear behavior. While the 7 mm setup has the predicted gradient increase factor of $\Delta g \sim 1.4$ at higher currents, the 15 mm setup never exceeds $\Delta g = 1.15$. This behavior is in agreement with the gradient scan using a varying offset.

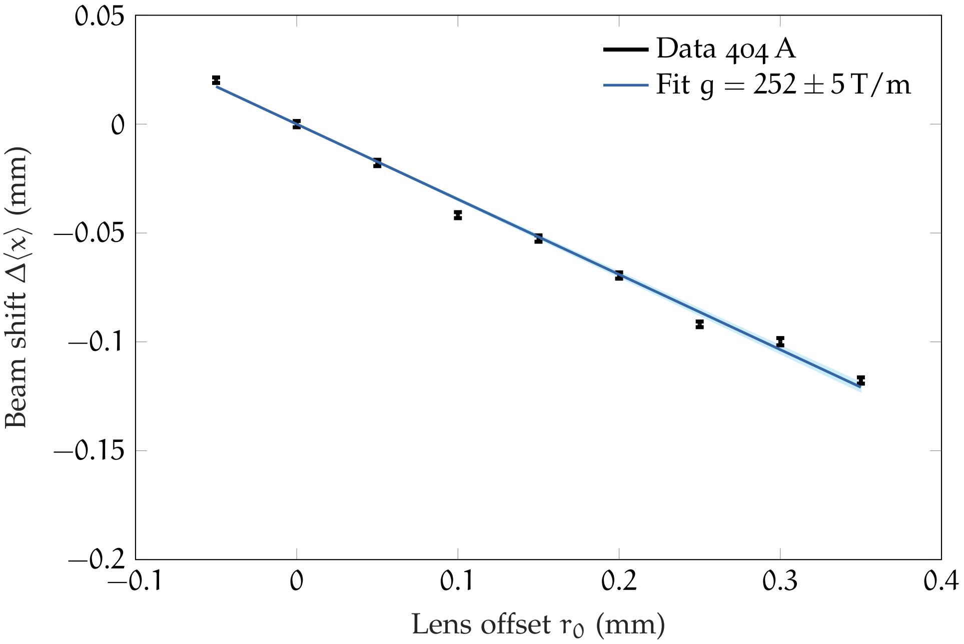

Figure 35: Measured beam shift as a function of the APL offset for a $L_{\text{cap}} = 15\,\text{mm}$ long capillary and 0 ns arrival time delay. The error bars indicate the standard error of the mean (SEM) of the COM for 100 shots. The blue line corresponds to a linear fit with the 95% confidence interval shown in light blue.

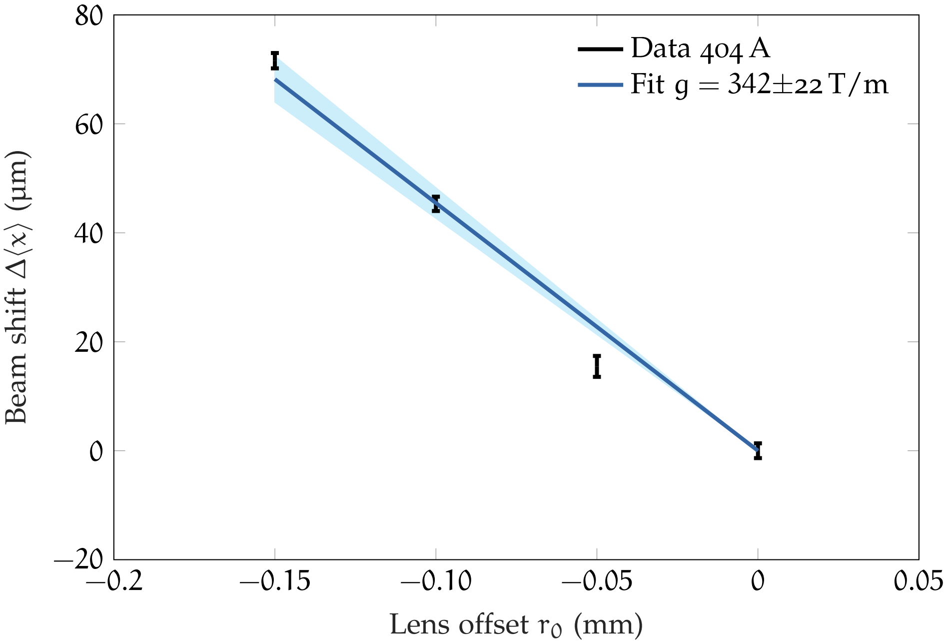

Figure 36: Measured beam shift as a function of the APL offset for a $L_{\text{cap}} = 15\,\text{mm}$ long capillary and 160 ns arrival time delay. The error bars indicate the standard error of the mean (SEM) of the COM for 100 shots. The blue line corresponds to a linear fit with the 95% confidence interval shown in light blue.

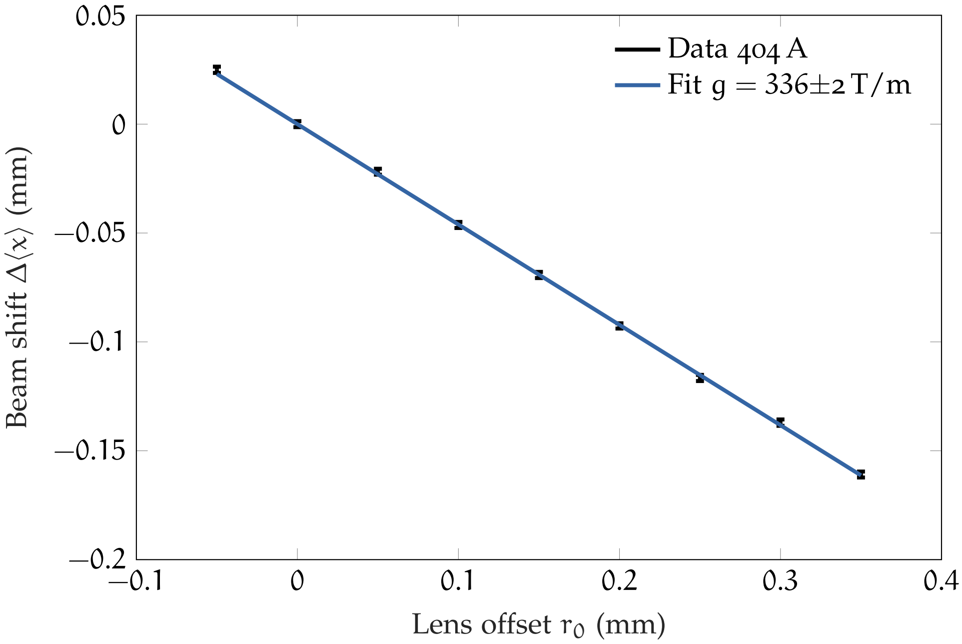

Figure 37: Measured beam shift as a function of the APL offset for a $L_{cap} = 15\,\text{mm}$ long capillary and 240 ns arrival time delay. The error bars indicate the standard error of the mean (SEM) of the COM for 100 shots. The blue line corresponds to a linear fit with the 95% confidence interval shown in light blue.

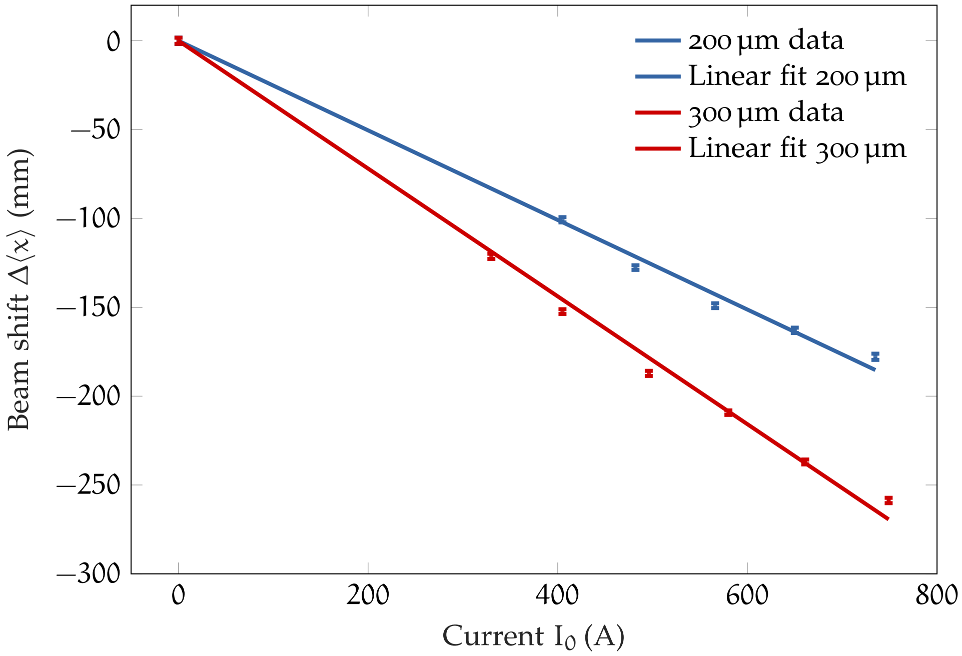

Figure 38: Measured beam position as a function of the 15 mm long APL current. Error bars for the standard error of the mean (SEM) of the COM for 100 shots are shown. The transverse APL offset was 200 µm for the blue data and 300 µm for the red data.

The 15 mm capillary setup was also used for emittance measurements. To make a meaningful comparison between the emittance degradation of different APL setups with varying length, the integrated magnetic-field gradient is the most sensible parameter. This is similar to normalizing with respect to length and helps to highlight the effects that stem from field nonlinearity. The integrated gradient can be calculated using the direct gradient measurements and the length including the fringe-field estimations. The results are listed in Tab.6, which compares the emittance degradation by the APL, ϵ_{APL}, per integrated gradient for a given focusing power. The ϵ_{APL} is defined as follows:

$$\epsilon_{\mathrm{APL}}^2 = \epsilon_f^2 - \epsilon_i^2, \tag{95}$$

in which ϵ_i is the initial emittance (without APL) and ϵ_f is the final emittance (after passage through the APL). A comparison between the two setups with the same electron arrival time(160 ns delay) is shown in Fig. 39. The results for the 7 mm setup show a strong correlation of the emittance growth with the focusing strength. This behavior is as expected and studied in detail in Sec. 4.3. Additionally, the results align with the findings of the direct magnetic-field measurements from Sec. 3.1.2 when the $J \sim T^{3/2}$-model is used. The 15 mm-long setup has less nonlinearity and therefore introduces less emittance degradation. This finding aligns with the gradient measurements with this setup, since both results point to a more linear behavior.

Taking all of the results for the 15 mm capillary setup mentioned above into account, one likely explanation is the presence of a heavier gas species. Following the argument made in Sec. 1.2.1, it would lead to a slower formation of the thermal steady state. The contamination most likely consisted of air that was either trapped in the buffer volume or a leakage in the gas supply. Since air consists of heavier gas species, the effect would be similar to the one described in the following section about the *CLEAR Plasma Lens Experiment*, where an APL setup using a light gas species (Helium) and a heavier gas species (Argon) were compared. The change to a heavier gas species led to a more linear magnetic field and emittance preservation. The explanation about the nature of the experimental error can not be confirmed with certainty in retrospect.

Table 6: Measured emittance with different APL configurations. The upper part of the table shows the results for the 7 mm long APL and different APL currents. The lower part shows the results for the 15 mm long APL.

Lens current (A)	Integrated gradient (T)	ϵ_n (mm mrad)
0	0	1.37 ± 0.01
188	1.8 ± 0.1	2.2 ± 0.1
364	3.3 ± 0.1	3.7 ± 0.1
368	3.3 ± 0.1	3.9 ± 0.1
740	6.2 ± 0.1	8.2 ± 0.1
Lens current (A)	Integrated gradient (T)	ϵ_n (mm mrad)
404	5.3 ± 0.3	4.6 ± 0.1

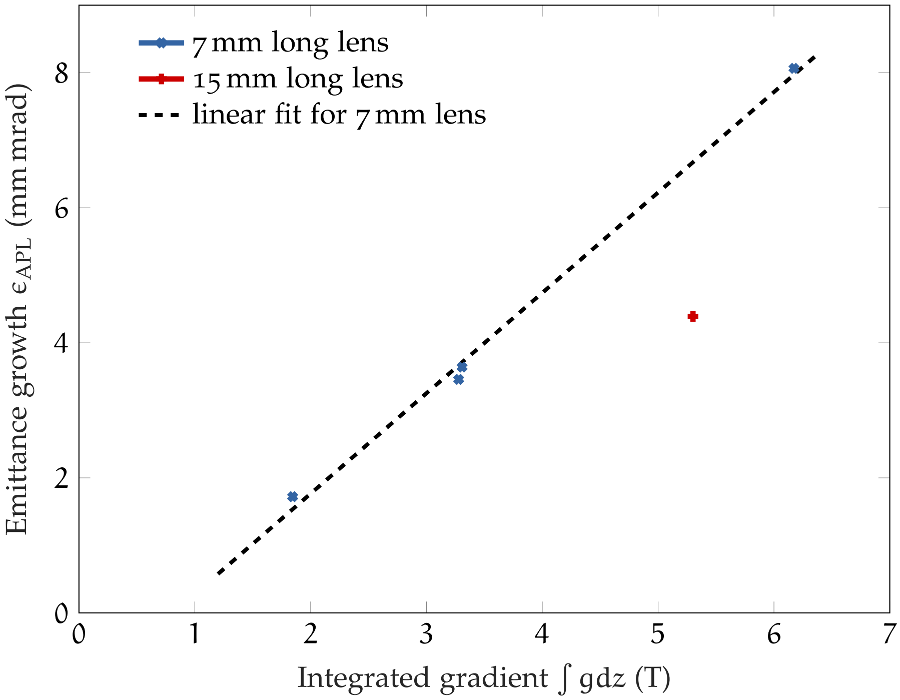

Figure 39: Introduced emittance growth by the APL depending on integrated gradient for the two APL setups. All scans were performed at the same timing.

The results of the *CLEAR Plasma Lens Experiment* have been published in [46]. In this experiment, the effect of using a heavier gas species - Argon - in an APL was studied. As described in Sec. 2.2, using this heavier gas species can be advantageous because of the slower electron-ion heat transfer and reduced thermal conductivity of heavier species. The effect this has on the formation of the thermal steady state that is described in the $J \sim T^{3/2}$-model is explained in Sec. 1.2.1. In light gas species such as Hydrogen or Helium, the equilibrium forms on the same timescale as the current ramp and it can be assumed that the system has reached a steady state. However, since the electron-ion heat transfer as well as the ion thermal conductivity scales inversely proportional with ion mass, this might not be the case for heavier gas species. The discharge current may reach its peak before the steady state is formed. The experiment confirmed this by measuring the beam offset for different lens offsets as described in Sec. 2.1.5 for Helium and Argon. The Helium showed a Δg of 1.34, which is consistent with the findings of the Mainz Plasma Lens Experiment. For the Argon case there was no clear evidence of a nonlinearity ($\Delta g = 1$ within the margin of error).

Additionally, emittance measurements using the quadrupole-scan method were performed. The results also confirmed that the Argon setup conserved the emittance of the beam. The emittance growth was kept below 0.25 mm mrad with a confidence level of 90% while using a gradient of 346 T/m.

These results are very promising since they show a way for APLs to become an alternative to QMs for capturing highly divergent beams. With minimal emittance degradation in each lens, an APL-based beamline as described in [24] becomes feasible. This is an important step towards reducing the high divergence and energy spread of beams for example from PWFAs and making them useful for applications.

The results from the CLEAR Plasma Lens Experiment show a very promising development in the direction of emittance preservation in APLs. Using heavier gas species in the APL in order to lower the electron-ion heat transfer and thermal conductivity and creating a smoother temperature profile, an aberration-free focusing could be achieved, leading to emittance preservation.

The experimental campaigns performed for this work at the Mainz Microtron showed the excellent shot-to-shot stability achievable in APLs. Additionally, the tunability of the APL up to a very high focusing strength of 1 kT/m was shown, which is a significant advantage over the next strongest alternative - permanent quadrupole magnets. These quadrupoles can achieve focusing gradients on the same order of magnitude ($\simeq 500\,\mathrm{T/m}$ [47]) but cannot be easily tuned in strength. Therefore these magnets have to be precisely moved in the longitudinal direction in order to tune the overall focusing strength of a duplet or triplet. As with electromagnetic quadrupoles, they also focus only in one dimension and defocus in the other. Tuning the APL's strength was achieved by simply varying the discharge voltage.

The emittance measurements performed during the Mainz Microtron campaign were in excellent agreement with the $J \sim T^{3/2}$-model when using the magnetic field measurements as a gauge for the nonlinearity. This shows that controlling the temperature distribution inside the APL channel is vital for developing an emittance-preserving APL for use in an accelerator beamline.

Additional results obtained with an APL that likely had air contamination showed a more linear, emittance preserving behavior. This behavior was also seen in the CLEAR Plasma Lens Experiment which used heavier gas species.

4

SIMULATIONS

This section discusses the simulations performed to provide an understanding of the processes involved in the plasma discharge as well as the interaction of the electron beam with the magnetic field of the APL. The first Section focuses on MHD simulations performed in collaboration with the Keldysh Institute of Applied Mathematics, Moscow. They provide an insight into the radial and temporal dependence of the magnetic field in the APL. The second section discusses the results of a combination of computational fluid-dynamics (CFD) and electric and magnetic-field simulations. They were performed to estimate the effect that the fringe fields at the end of the capillary have on the magnetic-field length. In the third section the previously discussed results are used in particle tracking simulations to estimate the effect the magnetic-field nonlinearity and fringe fields have on a passing electron beam. The last section focuses on the use of an APL in combination with PWFAs exploited at FLASHForward. It specifically discusses design choices for the plasma source to enable emittance-preserving release and capture of the beam using numerical simulations of the focusing inside the plasma accelerator.

4.1 MAGNETOHYDRODYNAMIC SIMULATIONS

Magnetohydrodynamic (MHD) simulations are used to study the behavior of electrically conducting fluids. The field of MHD has been initiated in [48]. It combines fluid dynamics through the Navier-Stokes equations and electromagnetism through Maxwell's equations. In [26] MHD simulations for the purpose of studying laser guiding in capillary discharge, waveguides were compared to the $J \sim T^{3/2}$-model (cf. Sec. 1.2.1). This model has been compared to measurements and used to predict the guiding efficiency in [49, 50]. In [19, 20] they were used to estimate magnetic-field nonlinearities in APLs. All of the above studies found that the simpler $J \sim T^{3/2}$-model of the form of Eq. (80) can predict the magnetic field behavior in a capillary discharge in the steady state given the boundary conditions.

A collaboration with the Keldysh Institute for Applied Mathematics in Moscow, Russia, and the Lawrence Berkeley National Laboratory in Berkeley, CA, USA - was established to carry out this work. Pavel Sasorov from the Keldysh Institute supplied MHD simulation results for the setup used in the experimental campaigns. This section highlights the results obtained in the 1D-MHD results shown in Fig. 42.

Fig. 40 shows the current profile for that 188 A plateau amplitude that was used as an input for the MHD simulations. The capillary radius was set to 0.5 mm and the initial hydrogen pressure was set to 400 Pa. In these simulations, the electron temperature at the wall was fixed at $T* = 0.5$ eV. This boundary condition has an influence on the overall magnetic field

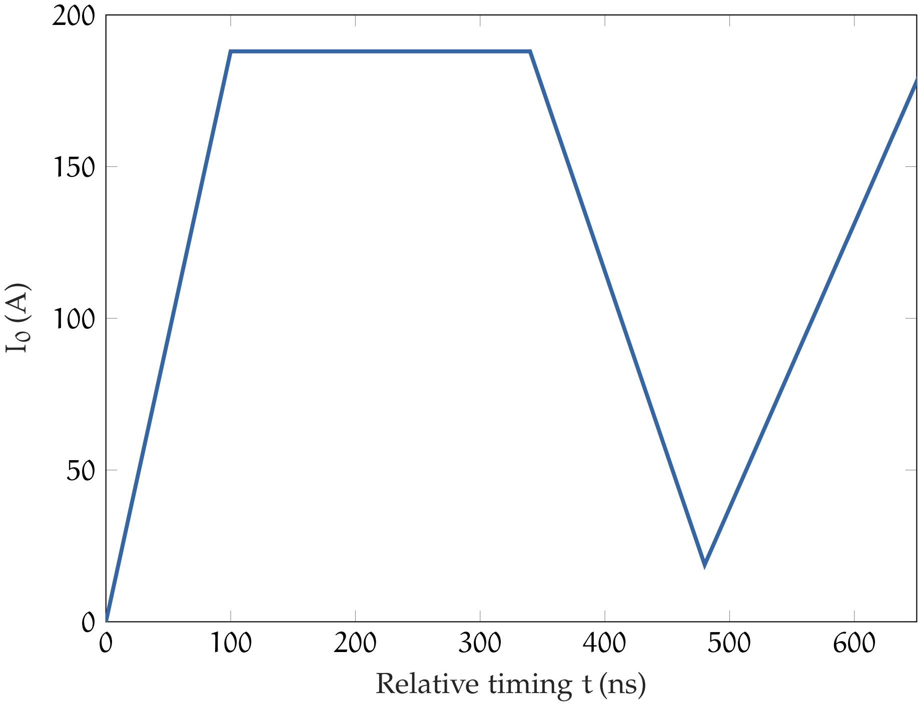

Figure 40: Current profile used as an input for the MHD simulation. The profile has a plateau of 188 A over 200 ns like the one used during the experiments.

behavior in the capillary. It has been studied theoretically with a model for the heat transfer to the capillary wall in [27]. Additionally, there is an upper limit to the wall temperature based on the fact that the sapphire did not melt during operation, which happens for higher currents and/or smaller capillary radii. The resulting electron temperature and density behavior can be found in Fig. 41. The results shown are for a relative timing of 200 ns in Fig. 40. This is the same timing as the middle timing used in most experiments - see Sec. 3.1.1. The resulting magnetic field strength for an input current of $I_0 = 368\,\text{A}$ can be found in Fig. 42. The results for the three currents $I_0 = 188\,\text{A}$, $368\,\text{A}$, and $740\,\text{A}$ were fitted with the $J \sim T^{3/2}$-model and their respective $u(0)$ are within their fitting uncertainty, which shows that the magnetic field behavior depends only weakly on the current for the regime between 188 A and 740 A. The fact that the $J \sim T^{3/2}$-model does not meet the ideal case and MHD at the wall is expected (cf. Sec. 1.2.1), since the model is tailored to the region around $r = 0$. The temporal dependence of the gradient increase factor Δg varies with the current, as shown for the three currents in Fig. 43. This shows that, for higher total currents, the steady state is reached earlier. The simulation results show that for the hydrogen APL, the steady state is reached almost immediately after the current ramp has reached its maximum. This means that the hydrogen based APL cannot effectively be used in the non-steady-state regime. As was described in Sec. 3.1.2, there was a strong dependence of the gradient increase factor on the current for the 7 mm long lens. The gradient-increase factor dipping below 1 at early times can also be seen. This was also seen experimentally in the temporally resolved measurements with the 15 mm capillary setup (cf. Sec. 3.1.4).

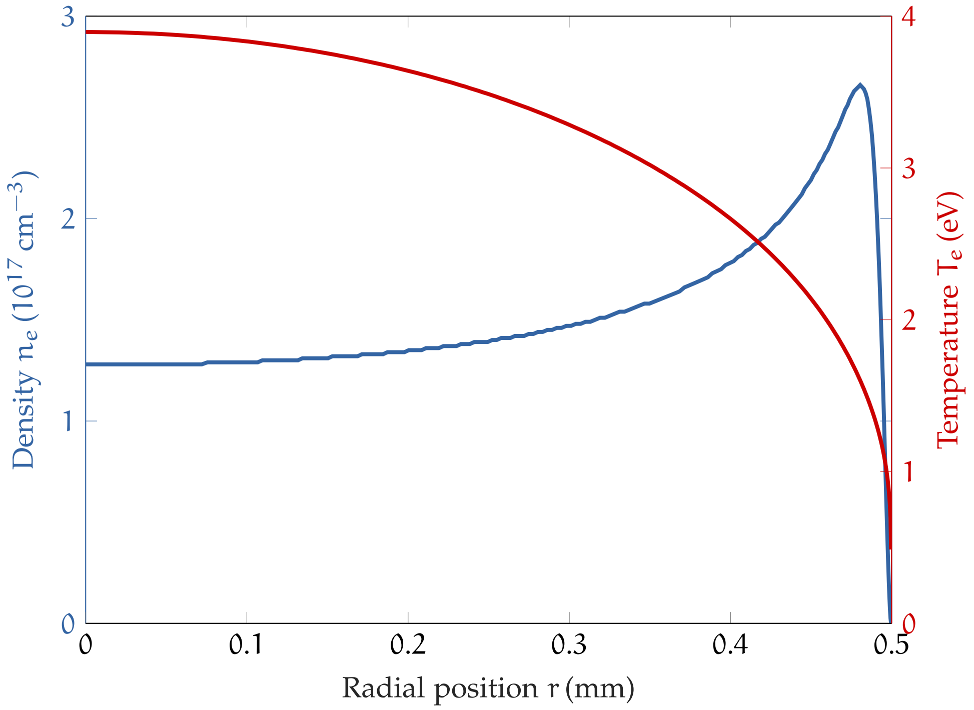

Figure 41: Radial dependence of electron temperature T_e and density n_e at 200 ns relative timing in Fig. 40.

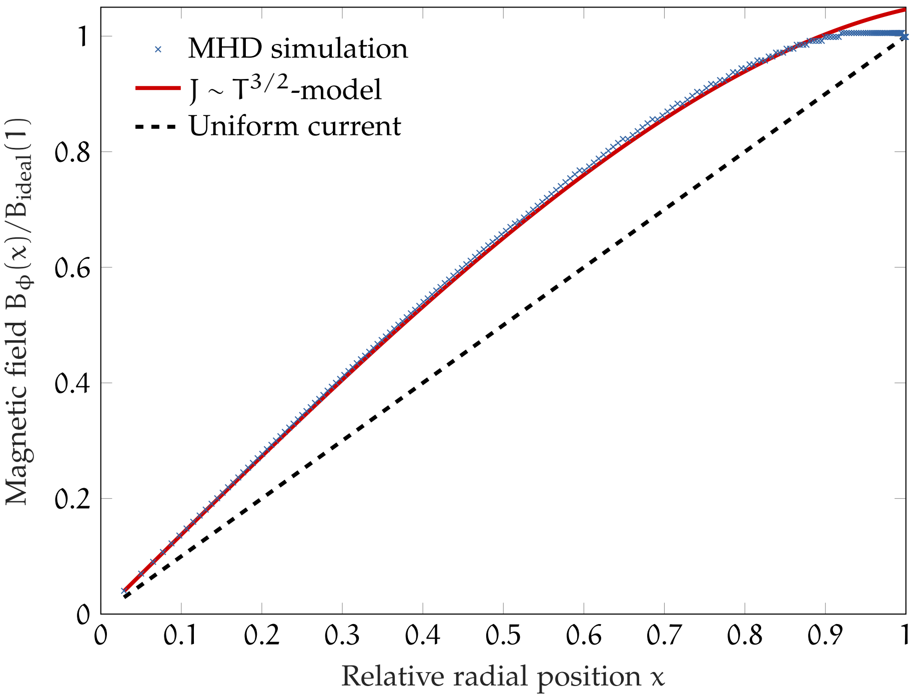

Figure 42: MHD simulation results for a $R = 0.5$ mm gas column of hydrogen with $n_0 = 10^{17}$ cm^{-3} and $I_0 = 368$ A. The $J \sim T^{3/2}$-model is of the form of Eq. (80) with the same boundary at the wall as the MHD simulation: $T^* = 0.5$ eV. The dashed line shows the field behavior for the uniform current density case B_{ideal}.

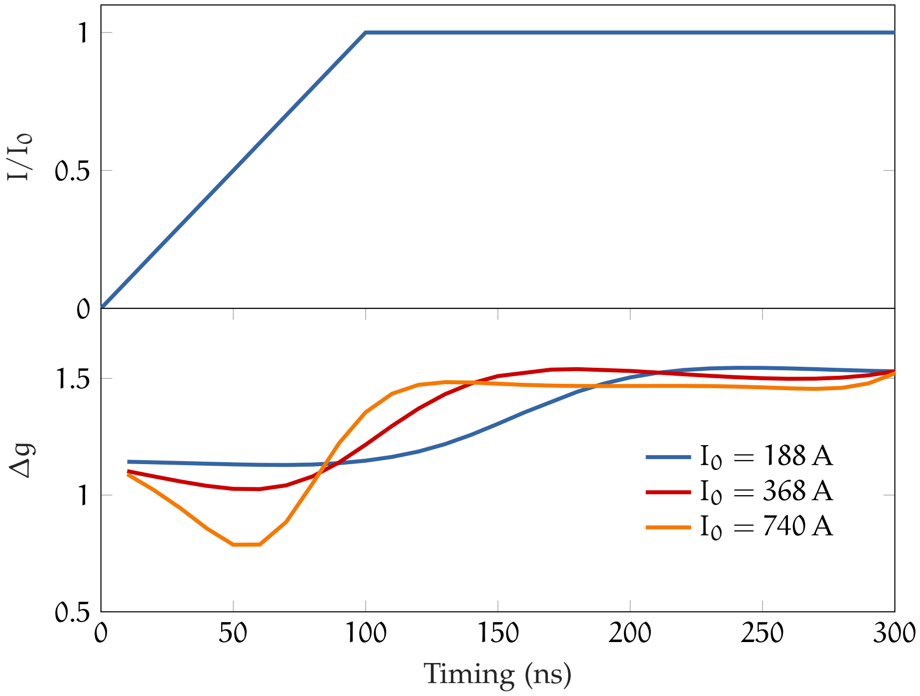

Figure 43: Temporal evolution of the gradient increase factor Δg according to MHD simulations for the three currents $I_0 = 188\,\mathrm{A}$, $368\,\mathrm{A}$, and $740\,\mathrm{A}$. The temporal evolution of the discharge current is shown on top.

4.2 FRINGE FIELD ESTIMATION

Computational fluid dynamics (CFD) simulations were used to estimate the gas density profile in the capillary. This gas density profile was converted into a conductivity profile by assuming full ionization and using the Spitzer model for plasma conductivity from Eq. (65). Here the assumption of a homogeneously heated plasma was employed. This means that a linear magnetic field gradient is expected in the middle part of the capillary between the inlets. The simulation software COMSOL* was used to combine the CFD simulation results with electric and magnetic field simulations in a plasma conductor. Fig. 44 shows the geometry created in COMSOL with finite elements used in the simulations visible on the surface.

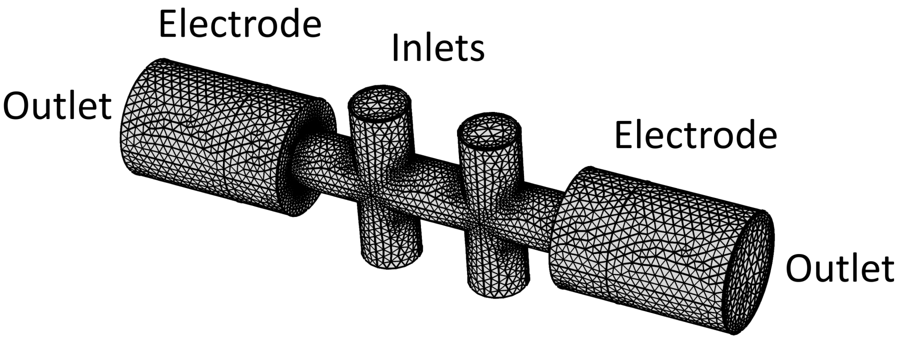

Figure 44: Geometry used in COMSOL simulations aimed at estimating fringe field length L_{fringe} and their effect on the emittance of a passing beam.

Fig. 45 shows the longitudinal magnetic field ramp from the COMSOL simulations. The longitudinal ramp in the fringe fields was modeled after

$$B(z_{\mathrm{edge}}) = B_0/(1 + \exp(4z_{\mathrm{edge}}/\sigma_{\mathrm{ramp}})), \tag{96}$$

where z_{edge} is the distance from the capillary end and σ_{ramp} is the ramp taper parameter, as commonly used in conventional magnet optics. The model agrees well with the simulation results. This model is used in particle tracking simulations that are described in the following Section.

---

* COMSOL Multiphysics Reference Manual, version 5.3a, COMSOL, Inc, www.comsol.com

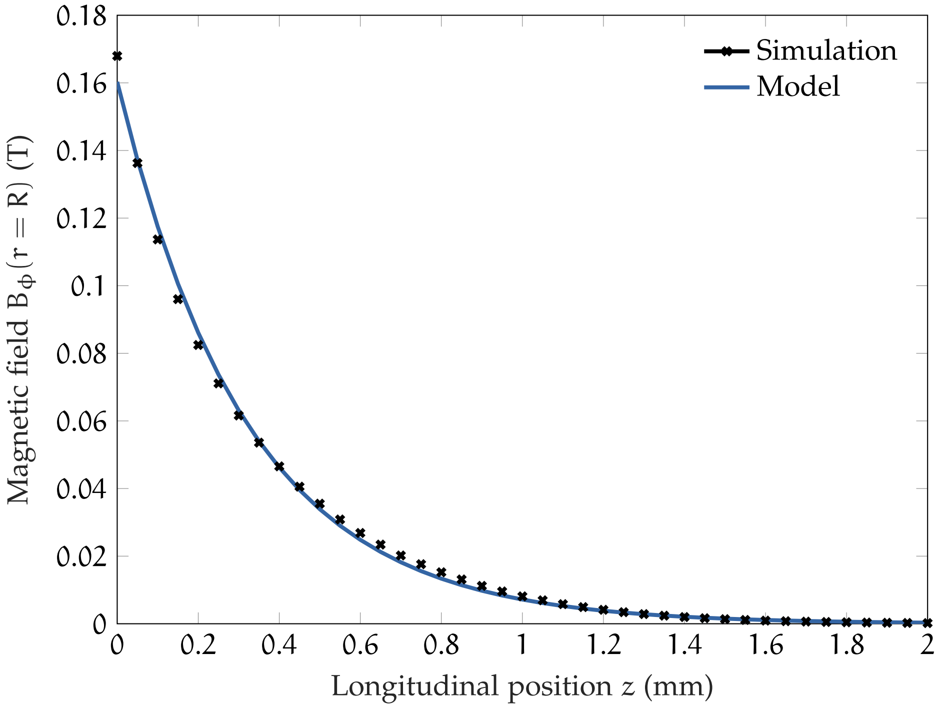

Figure 45: Results from the COMSOL simulations in comparison with the model from Eq. (96) with $\sigma_{\mathrm{ramp}} = 1.3\,\mathrm{mm}$.

The passage of electrons through the APL was simulated using the particle tracking algorithm ASTRA [51]. In ASTRA, a model of the azimuthal magnetic field in an APL is included which is based on

$$B_\phi(r) = \frac{\mu_0}{2} J(r) \cdot r \tag{97}$$

and a current density of the form of

$$J(r) = a_1 + a_3 r^2 + a_5 r^4. \tag{98}$$

In this model the $J \sim T^{3/2}$-model introduced in Sec. 1.2.1 can be realized by using the coefficients from Eq. 79. Additionally, a model of the fringe fields is used which assumes a longitudinal drop-off of the field like

$$B(\Delta z) = B_0 \frac{1}{1 + \exp(4\Delta z/\sigma_{\mathrm{ramp}})}. \tag{99}$$

This is in good agreement with the fringe field behavior from Sec. 4.2. In order to assess the influence the fringe fields have on the emittance of a traversing electron beam, an ideal APL with fringe fields was used. The emittance degradation in this case was negligible.

For the simulations using a nonlinear APL, the beam was modeled after the MaMi-B beam. It is transversally Gaussian with minimal divergence and the beam size measured at the position of the APL. The nonlinear behavior was taken from Tab. 5 and the respective $J \sim T^{3/2}$-model. Fig. 46 shows the phase-space density before (top) and after (bottom) an APL of $L = 7.5\,\mathrm{mm}$. The first obvious difference is the rotation of the phase space due to the focusing of the APL. The emittance degradation can be seen in the lagging behind of the particles starting out with higher vertical position with respect to the central part of the beam. The rotation velocity is dependent on the focusing force. In the nonlinear APL, the focusing force depends on the radial position with smaller focusing strength farther out, thus the lag.

In order to make the simulation results and the emittance measurements from Sec. 3.1.3 comparable, the measured emittance is assumed to be the 95% charge emittance. The input particle distribution is chosen such that the 95% charge emittance matches $\epsilon_n = 1.37\,\mathrm{mm\,mrad}$. This is done because the measurements are likely to not measure 100% of the charge of the beam. This is in part due to the limitation of the optical setup used in the experiment with regards to charge sensitivity. The wings of the measured beam spots may vanish in the noise and thus will be disregarded in the rms calculation of the beam. Fig. 47 shows a projection of

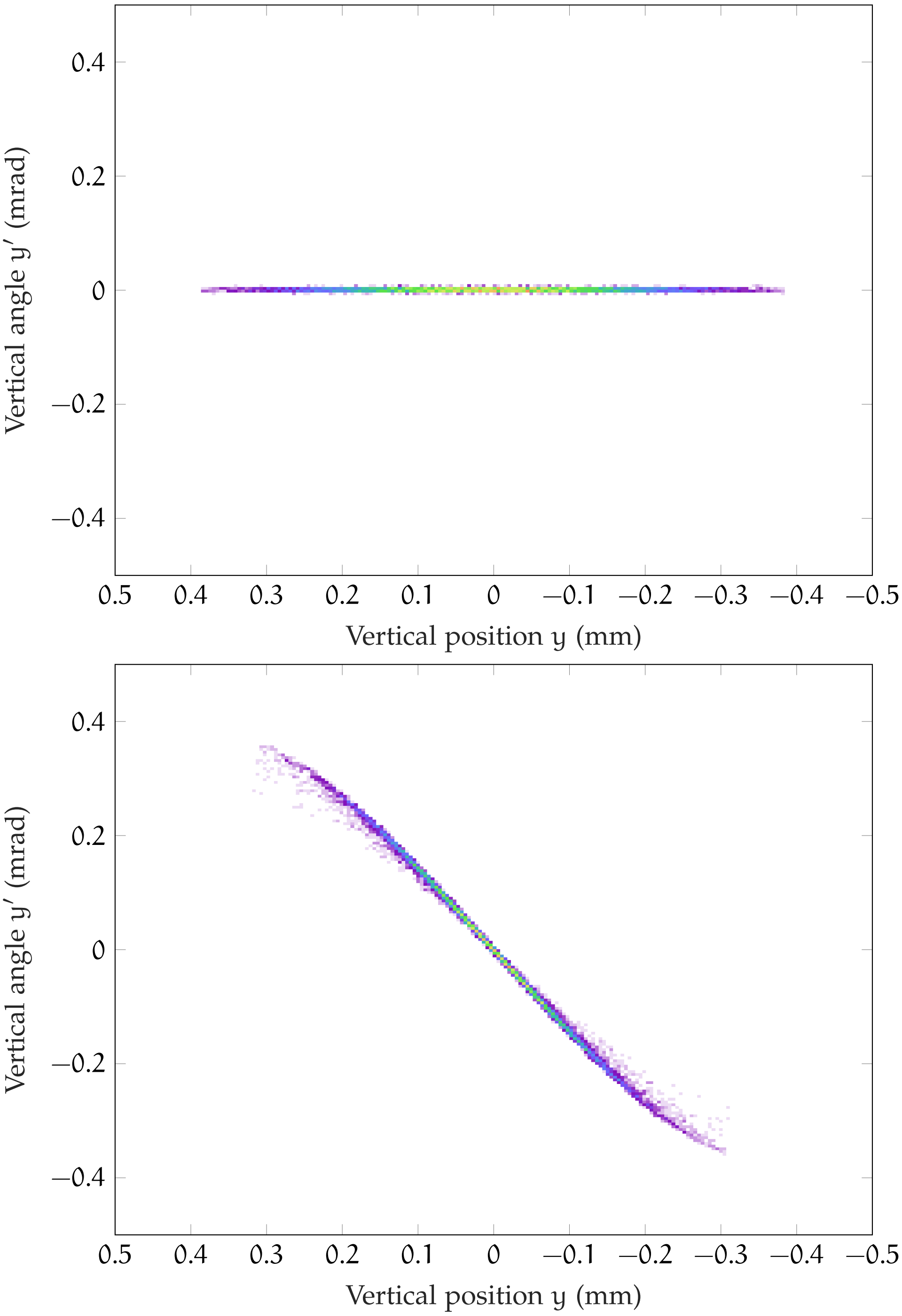

Figure 46: Particle-tracking simulation results for the transverse phase space. The top plot shows the phase-space density at the beginning of the simulation. The bottom plot shows the phase-space density after the APL.

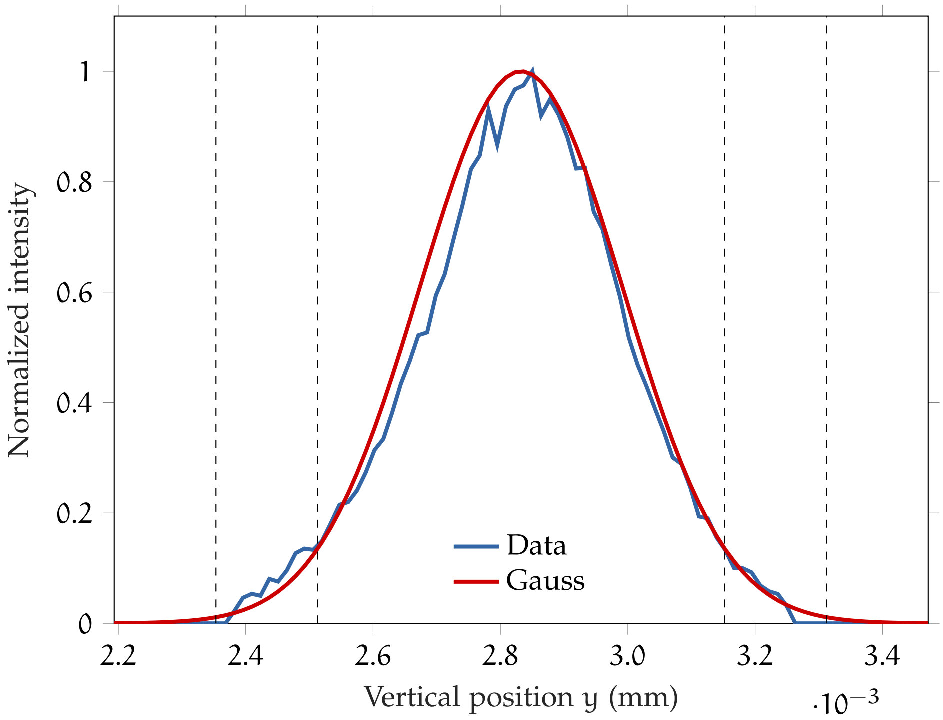

Figure 47: Projection of the measured beam spot 25 cm behind the APL without discharge current and a normal distribution (Gauss) with the same width and mean values. The four vertical lines represent the two and three σ-width.

the beam 25 cm after the APL with no discharge current and hence no focusing. The normal distribution (Gauss) also shown has the same mean and width as the particle distribution. The beam at this position is well presented by a normal distribution. Fig 48 shows a projection of a measured beam spot after being focused by the APL and captured and refocused by the QM triplet (see Appendix B) and a normal distribution with the same width and mean values. The two projections shows the narrowest beam size in the scan. The beam is focused and has significant charge in the wings of the distribution, leading to a higher rms width than the normal distribution when comparing their full width at half maximum (FWHM). This may be due to the effect seen in Fig. 46.

Fig. 49 shows the simulation results for an effective magnetic-field length $L = 7.5\,\text{mm}$ and $I_0 = 368\,\text{A}$. The field was modeled after the $J \sim T^{3/2}$-model with a cold-wall boundary condition. Tab. 7 provides the results for the currents and lengths used in the Mainz campaigns. For the cases with a lower gradient-increase factor than for the cold-wall case, the $J \sim T^{3/2}$-model was fitted accordingly. This is especially relevant for the 15 mm case. The predicted values from the offset scans agree well with the measured results, indicating that the $J \sim T^{3/2}$- and the fringe field model accurately describe the magnetic field behavior in the APL.

In order to evaluate the emittance-measurement results, a comparison to the theoretical prediction of the emittance growth is given in this section. The theoretical model described in Sec. 1.2.1 as well as the MHD simulations results in 4.1 provide the dependence of the

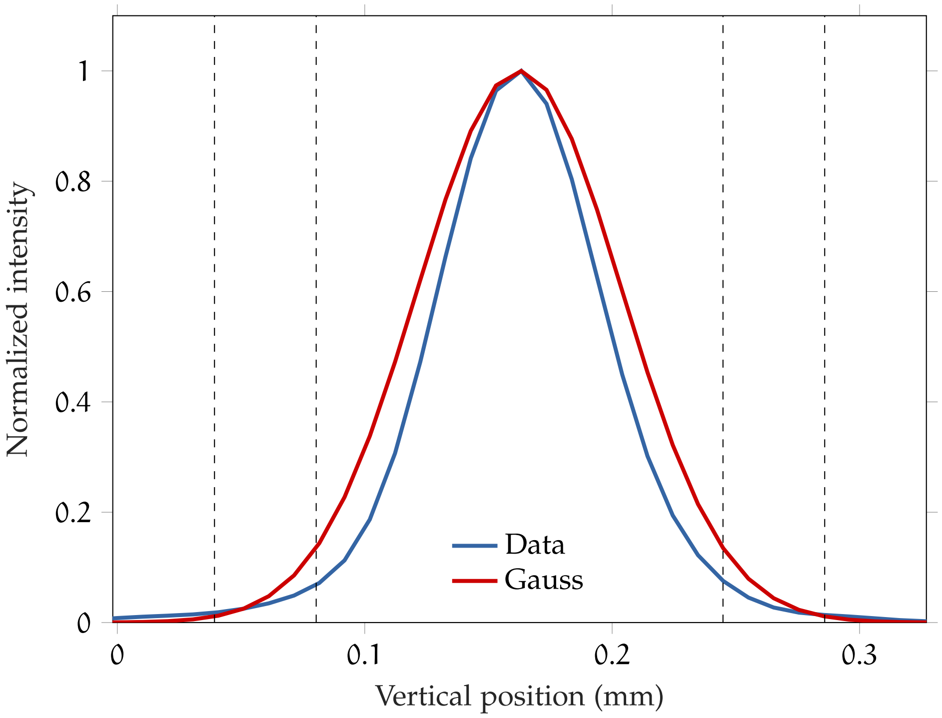

Figure 48: Projection of the measured beam spot and a normal distribution (Gauss) with the same width and mean values. The four vertical lines represent the two and three σ-width.

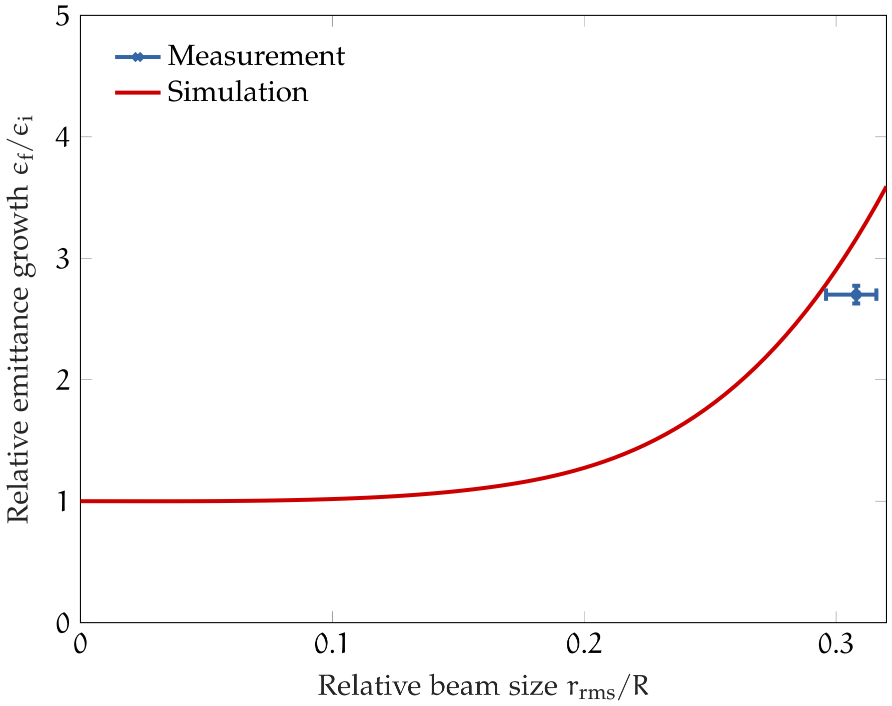

Figure 49: Particle-tracking simulation results for relative emittance degradation in dependence of incoming rms beam size for an APL with $I_0 = 368$ A. The measured emittance degradation is also shown.

Table 7: Comparison of MHD and particle tracking simulations to measurement results. Top part shows the measurements for the 7 mm, the bottom part for the 15 mm long APL.

	Δg			g_{core} (T/m)		ϵ (mm mrad)	
I_0 [A]	MHD	$J \sim T^{3/2}$	Meas.	Sim.	Meas.	Sim.	Meas.
188	1.379	1.48	1.58 ± 0.07	216	246 ± 10	2.6	2.2 ± 0.1
364		1.47	1.47 ± 0.02		437 ± 8	4.6	3.7 ± 0.1
368	1.381	1.48	1.50 ± 0.02	423	441 ± 5	7.8	3.9 ± 0.1
740	1.404	1.37	1.37 ± 0.01	855	823 ± 8	9.0	8.2 ± 0.1
404	1.382	1.04	1.04 ± 0.01	445	336 ± 2	3.9	4.6 ± 0.1

magnetic field on the radius. With this field behavior an analytic estimate for the emittance evolution can be derived through Eq. (57).

In the endeavor of preserving the high quality of plasma-accelerated beams, there is another powerful method apart from rapid capturing, the adiabatic release. Since both methods work completely independent from one another, they can be combined to maximize their effectiveness. In adiabatic release, the section of the plasma that transitions into vacuum is tailored in a way that allows for the emittance to be preserved during the release while mitigating chromatic emittance growth in the drift behind it (cf. Sec. 1.1.6). As described in Sec. 1.1.6, the chromatic emittance growth is dominated by the divergence u'_{rms} of the beam. The adiabatic release uses the focusing properties of the blowout plasma channel described in Sec. 1.2.2 to lower u'_{rms} and increase the beam size u_{rms} while keeping the beam matched. In the blowout regime, the focusing force is proportional to the plasma density. Tailoring the design of the plasma source can enable this transformation to be adiabatic, in this case meaning without emittance increase. A downramp in plasma density on a scale longer than the beta-function ensures adiabatic release [14, 36].

This section presents the results of numerical simulations aimed at designing a gas cell suitable for an adiabatic release scheme at FLASHForward [52], the beam-driven plasma accelerator experiment at DESY . The CFD software Open∇FOAM ® [53] was used to simulate gas flow into capillary targets designed in computer-aided design (CAD) software. Full ionization was assumed to translate the gas density n_0 into the plasma density n_e. The results were evaluated with the help of a numerical model that probes a plasma density profile for the quality of its plasma-to-vacuum transition in terms of adiabatic release of electrons. The studies consider only matched beams as described in Sec.1.2.2, where $\beta_{\mathrm{matched}} = \sqrt{2\gamma}/k_p$, with the plasma wavenumber k_p as defined in Eq. (84). The beam extraction is investigated by means of an ordinary differential equation (ODE) for monoenergetic beams in an ideal system, where Eq. (92) defines the focusing parameter. This implies that the change in plasma density happens on a length scale much longer than the plasma wavelength. The single-particle equation of motion is given by Eq. (93), where the focusing parameter $K = K(s)$ depends only on the longitudinal position.

This model can be used to solve the ODE numerically for given parameters of the electron beam and the plasma density evolution. A numerical study with a beam matched to the plasma, which translates to a beta-function of $\beta = 1.3\,\mathrm{mm}$, a normalized emittance of $\epsilon = 500\,\mathrm{nm\,rad}$, energy of $E = 1.5\,\mathrm{GeV}$, and an energy spread of 1% was performed for a cut-off profile, a plasma source design with a rapid decrease in density, and a design tailored for adiabatic release. The results can be found in Fig. 50. The longitudinal position $s = 0\,\mathrm{mm}$ represents the capillary end. Here, by definition a rapid drop in density takes place owing to the absence of any confinement of the gas. The cut-off case is a theoretical worst-case scenario which is used to show the degree by which a tailored case can decrease the release divergence. In the cut-off case, the beam is released with high divergence of 360 µrad, leading to severe emittance growth in the drift section according to Eq. (62).

A typical design for continuous flow plasma sources is shown in Fig. 12. Such a design is well suited for APLs since the high-density region is close to the electrodes, enabling easy gas discharge. For plasma acceleration, however, this rapid density ramp is problematic. Targets with the gas inlets close to the entrance and exit are not suitable for adiabatic release and therefore do not significantly decrease the divergence. The tailored design is realized by increasing the distance between inlet and exit longer than the local beta-function. In the case at hand, this increases the beta-function to $\beta = 13.8\,\mathrm{mm}$ and decreases the divergence from 360 µrad to 110 µrad. This is beneficial in more than one way. On the one hand it decreases the chromatic emittance growth in the drift behind the source. On the other hand it makes capturing easier. The beam size in the first focusing optic is dominated by the divergence at the release owing to the small release beam size ($\sim 1\,\mu\mathrm{m}$). The APL also has to be placed a minimal distance (on the order of a few centimeters) behind the plasma source due to the danger of a faulty discharge into the plasma source and potentially high peak power laser remnants disturbing the APL in the case of LWFAs, increasing the beam size further for high divergence beams. A smaller beam size is less sensitive to the negative impact of nonlinear field behavior on the emittance.

When designing the plasma source for a plasma accelerator, this release section has to be taken into account in the length of the overall target. The adiabatic release relies on wakefields in the blowout regime being present until the end of the capillary. If a target was designed for maximum energy gain, thus depleting the driver, the wakefield will vanish or become linear/quasi-linear before the end of the capillary. This has to be avoided, necessitating a trade-off between maximum energy gain and quality preservation.

A theoretically ideal ramp shape for adiabatic release was introduced in [36]. This ramp shape is very hard to realize experimentally, however. Since slightly longer ramps do not impact the adiabatic release negatively, a more experimentally realistic shape was chosen for the FLASHForward simulations. A length-parameter study was employed to find the ramp yielding adiabatic release with minimal length.

A study devoted to the capturing of the above defined beam is shown in Fig. 51. Here, an APL is placed 10 cm downstream of the plasma source. It is designed to capture the beam after its release for the rapid and adiabatic release scenarios with a radius of $R = 0.5\,\mathrm{mm}$ and a length of $L_{\mathrm{cap}} = 5\,\mathrm{cm}$. For the adiabatic release scenario, the APL current is $I_0 = 600\,\mathrm{A}$, while for the rapid release it needs a current of $I_0 = 800\,\mathrm{A}$. The corresponding core gradients are $g = 620\,\mathrm{T/m}$ and $g = 828\,\mathrm{T/m}$ respectively. The emittance growth during the drift section is modeled after Eq. (62), while the emittance growth in the APL is derived through Eq. (57). This study is employed in order to assess the importance of a combined approach with adiabatic release and rapid APL capturing.

With neither adiabatic release nor capturing, the emittance grows to 25.2 mm mrad at a distance of 50 cm after the plasma accelerator release, which is an increase of 24.7 mm mrad. Capturing without adiabatic release reduces the growth to 3.0 mm mrad, which is already a significant improvement but still constitutes a five-fold emittance increase. When the adiabatic release alone is employed, the emittance only grows to 2.5 mm mrad even without APL capturing, which is better than the rapid release with capturing (3.0 mm mrad, see above). This highlights the importance of a controlled release. However, this emittance growth is still relatively high when compared to the combined approach. With both mechanisms employed, the emittance reaches 0.62 mm mrad at a point 50 cm after release, which is an increase of 0.12 mm mrad or a 206-fold decrease of emittance growth when compared to the case with none of the two techniques employed. The very low emittance growth introduced by the (nonlinear) APL is explained by the small beam size $r_{\mathrm{rms}}/R < 0.1$ inside it. The study shows that only through a combined approach of adiabatic release and early, azimuthally symmetric capturing, can the initially low emittance be preserved.

With a combined approach, care has to be taken when designing the APL since the beam size might become small enough so wakefields in the APL could start to impact the beam by driving a wakefield in the APL's plasma. A detailed analysis of the impact of wakefields in APLs can be found in [31].

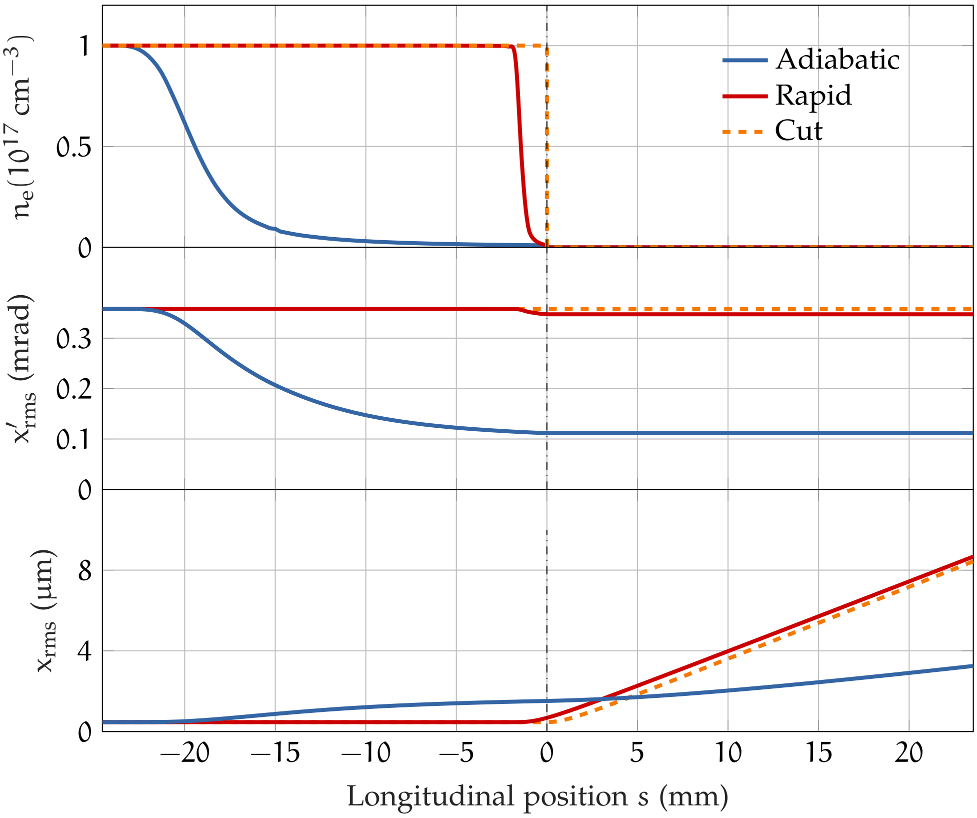

Figure 50: Evolution of divergence and beam size for different release scenarios. The emittance evolution of rapid and adiabatic release cases can be found in Fig. 51.

4.4.1 *Conclusions*

In this section, different types of simulation approaches are used to study the magnetic field inside an APL, as well as the interaction of a beam with such a field and finally the behavior

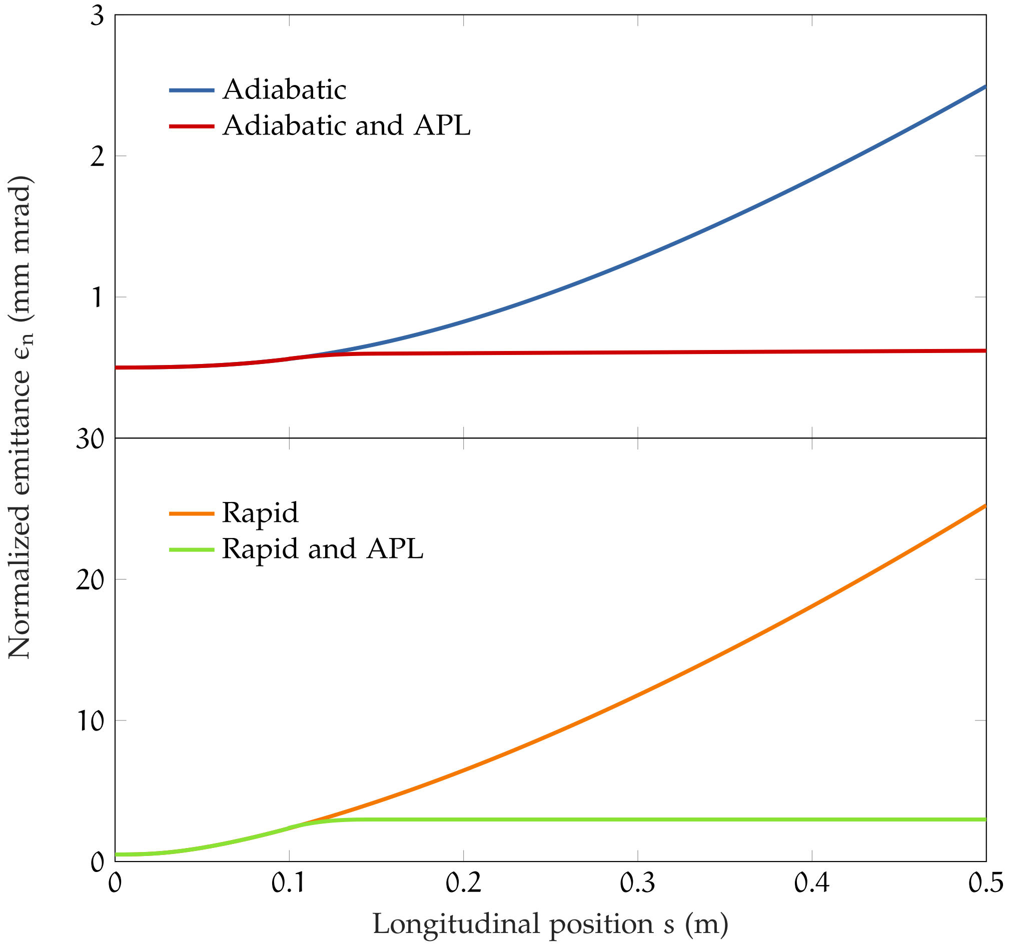

Figure 51: Evolution of the normalized emittance after release from the plasma for the adiabatic (top) and the rapid (bottom) release scenario with and without an APL used for capturing 10 cm after the release.

of a beam during release from a plasma accelerator. The introduced techniques are subsequently used to study a realistic experimental setup at DESY. The study shows the significant difference in emittance preservation that can be achieved when a setup is used that uses both a tailored release of the beam from the plasma accelerator as well as rapid capturing with an APL. The increase in emittance that can be achieved is shown to be two orders of magnitude lower for the combined approach when compared to a setup without any of the introduced techniques used.

5

SUMMARY AND OUTLOOK

An active plasma lens setup has been developed and tested. To characterize it, the plasma lens was used in the beamline of a conventional electron accelerator – the Mainz Microtron. Two different lengths were realized, 7 mm, and 15 mm, each with a diameter of 1 mm. This is the first time a combination of direct magnetic field measurements using offset scans and emittance measurements have been performed for a plasma lens.

The results of the direct magnetic-field measurements show excellent shot-to-shot stability on the sub-percent level. The magnetic field gradient ranged from 200 T/m to 1000 T/m, exceeding state-of-the-art electromagnetic QMs by a factor of 6. The setup allowed for tuning of the magnetic-field gradient by the press of a button, making it very flexible. The measured gradients are systematically higher than those expected from an ideal plasma lens, which is in agreement with the theory of capillary-discharge plasma. The increased gradients stem from the theoretically predicted nonlinear magnetic-field behavior in the APL.

Emittance measurements performed with the plasma lens in the beamline show emittance degradation due to the nonlinearity of the magnetic field. The measured emittance degradation agrees well with predictions made from particle-tracking simulations through the magnetic field derived from the field-gradient measurements. The measured emittance degradation ranges from $\sim 2 - 8$ mm mrad depending on the focusing strength used. This value may however be drastically reduced by using a smaller beam size in the APL. Using the above mentioned particle-tracking method, it is predicted that the 95%-charge emittance growth can be reduced to the 100 nm rad level by using beams with an rms beam size of 20% of the capillary radius R. This is a significant finding since it cuts down the overall emittance degradation in a plasma based accelerator beamline by an order of magnitude.

Lastly, the results of a study performed for the beam-driven plasma accelerator at FLASHForward stresses the importance of a combined approach of plasma-source design, including an adiabatic release section and a fast capturing mechanism. It shows that after just 50 cm of drift space, the emittance is degraded by a factor of 50 if no effort is put into the preservation. With the combined approach developed in this thesis, the overall increase is reduced to just 24%, keeping the normalized emittance smaller than 1 mm mrad.

Future studies should focus on combining plasma-based acceleration schemes with heavy-gas APLs for capturing to make measurements of preserved emittances of plassma accelerated beams possible. Subsequently, a tuning of the plasma cell of the accelerator should be employed to ensure adiabatic release, and preserve the emittance in the accelerator-capture beamline. This will pave the way towards successful applications of plasma accelerators.

APPENDICES

APPENDIX A - TRANSFER MATRICES OF SOME IMPORTANT BEAMLINE ELEMENTS

The derivation of all beamline elements used in the scope of this work except for APLs can be found in [54]. In all derivations it is assumed that the elements are mounted so that no coupling between the (x, x')- and the (y, y')-plane is introduced.

The transfer matrix of a ***drift space*** - a section of the beamline with no magnetic optics present - is given by

$$\mathbf{R}_O(\rho_u, \alpha) = \begin{pmatrix} 1 & l & 0 & 0 \\ 0 & 1 & 0 & 0 \\ 0 & 0 & 1 & l \\ 0 & 0 & 0 & 1 \end{pmatrix}, \tag{100}$$

in which l is the length of the drift section.

The transfer matrix of a ***sector dipole*** - a magnet with faces perpendicular to the central beam trajectory - is given by

$$\mathbf{R}_S(\rho_u, \alpha) = \begin{pmatrix} \cos(\alpha) & \rho_u \sin(\alpha) & 0 & 0 \\ -\frac{\sin(\alpha)}{\rho_u} & \cos(\alpha) & 0 & 0 \\ 0 & 0 & 1 & \rho_u \alpha \\ 0 & 0 & 0 & 1 \end{pmatrix}, \tag{101}$$

in which α is the deflection angle and ρ_u the bending radius. In addition to this, dispersion is introduced, so a 6x6-matrix would be necessary to fully describe the effect of a sector dipole. Since this part does not play a role in the measurements taken in the scope of this work, we will omit it in the discussion. A dipole magnet with its faces not perpendicular to the central beam trajectory will lead to edge focusing. If the magnet is installed symmetrically with respect to the central beam trajectory, the edge focusing of one of the edges is described by

$$\mathbf{F}(\rho_u, \alpha) = \begin{pmatrix} 1 & 0 & 0 & 0 \\ \frac{\tan(\alpha/2)}{\rho_u} & 1 & 0 & 0 \\ 0 & 0 & 1 & 0 \\ 0 & 0 & -\frac{\tan(\alpha/2)}{\rho_u} & 1 \end{pmatrix}. \tag{102}$$

The transfer matrix for the ***edge-focusing dipole*** then reads

$$\mathbf{R}_D(\rho_u, \alpha) = \mathbf{F}(\rho_u, \alpha) \cdot \mathbf{R}_S(\rho_u, \alpha) \cdot \mathbf{F}(\rho_u, \alpha). \tag{103}$$

The transfer matrix of a QM is given by

$$\mathbf{R}_{QM}(k, l) = \begin{pmatrix} \cosh(l\sqrt{|k|}) & \frac{\sinh(l\sqrt{|k|})}{\sqrt{|k|}} & 0 & 0 \\ \sqrt{|k|}\sinh(l\sqrt{|k|}) & \cosh(l\sqrt{|k|}) & 0 & 0 \\ 0 & 0 & \cos(l\sqrt{|k|}) & \frac{\sin(l\sqrt{|k|})}{\sqrt{|k|}} \\ 0 & 0 & -\sqrt{|k|}\sin(l\sqrt{|k|}) & \cos(l\sqrt{|k|}) \end{pmatrix}, \tag{104}$$

for $k > 0$. Here $k = eg/p$ is the focusing parameter with e, the elemental charge, g, the magnetic field gradient, and p, the particle momentum. Usually the identity $\phi = l\sqrt{|k|}$ is used. For $k < 0$, the transfer matrix reads

$$\mathbf{R}_{QM}(k, l) = \begin{pmatrix} \cos(\phi) & \frac{\sin(\phi)}{\sqrt{|k|}} & 0 & 0 \\ -\sqrt{|k|}\sin(\phi) & \cos(\phi) & 0 & 0 \\ 0 & 0 & \cosh(\phi) & \frac{\sinh(\phi)}{\sqrt{|k|}} \\ 0 & 0 & \sqrt{|k|}\sinh(\phi) & \cosh(\phi) \end{pmatrix}. \tag{105}$$

The transfer matrix of an APL with uniform current density is

$$\mathbf{R}_{\mathrm{APL}}(k,l) = \begin{pmatrix} \cosh(\phi) & \frac{\sinh(\phi)}{\sqrt{|k|}} & 0 & 0 \\ \sqrt{|k|}\sinh(\phi) & \cosh(\phi) & 0 & 0 \\ 0 & 0 & \cosh(\phi) & \frac{\sinh(\phi)}{\sqrt{|k|}} \\ 0 & 0 & \sqrt{|k|}\sinh(\phi) & \cosh(\phi) \end{pmatrix}, \tag{106}$$

for $k > 0$. For $k < 0$ the transfer matrix becomes

$$\mathbf{R}_{\mathrm{APL}}(k,l) = \begin{pmatrix} \cos(\phi) & \frac{\sin(\phi)}{\sqrt{|k|}} & 0 & 0 \\ -\sqrt{|k|}\sin(\phi) & \cos(\phi) & 0 & 0 \\ 0 & 0 & \cos(\phi) & \frac{\sin(\phi)}{\sqrt{|k|}} \\ 0 & 0 & -\sqrt{|k|}\sin(\phi) & \cos(\phi) \end{pmatrix}. \tag{107}$$

The Mainz Microtron (MaMi) consists of 100 keV DC-guns (thermoionic for standard and GaAsP-photocathode for polarized beam), a quasi-cw-linac (chopper, prebuncher and three accelerating sections), three race track microtrons (MaMi A1, A2 and B), and an harmonic double-sided microtron (MaMi-C). In the scope of this work the MaMi-B microtron was the last stage in use. The beamline used for the experiments is mainly used by the X1 group of the *Institut für Kernphysik* at he University of Mainz. MaMi-B is capable of delivering an electron beam of energies between $E = 180 - 855\,\text{MeV}$ (in steps of 15 MeV) with an energy spread of $\sigma_E = 13\,\text{keV}$ at 855 MeV and horizontal and vertical normalized rms design emittances of $\epsilon_{hor} = 13\,\text{mm mrad}$ and $\epsilon_{ver} = 0.84\,\text{mm mrad}$ respectively. It can be operated in a diagnostic bunch mode in which bunch trains of 10 ns length are delivered. These bunch trains have a substructure of 2.45 GHz from the RF-cavities and a DC current of 100 µA. This mode of operation and a repetition rate of 1 Hz was chosen for the APL experiment.

A measurement of the response of the magnetic field to a change in current for the scan quadrupoles was undertaken. The result can be seen in Fig. 52. The linear fit with an R-squared value of $> 95\%$ confirms that the quadrupoles respond linearly to the current applied and are suited for quadrupole scans.

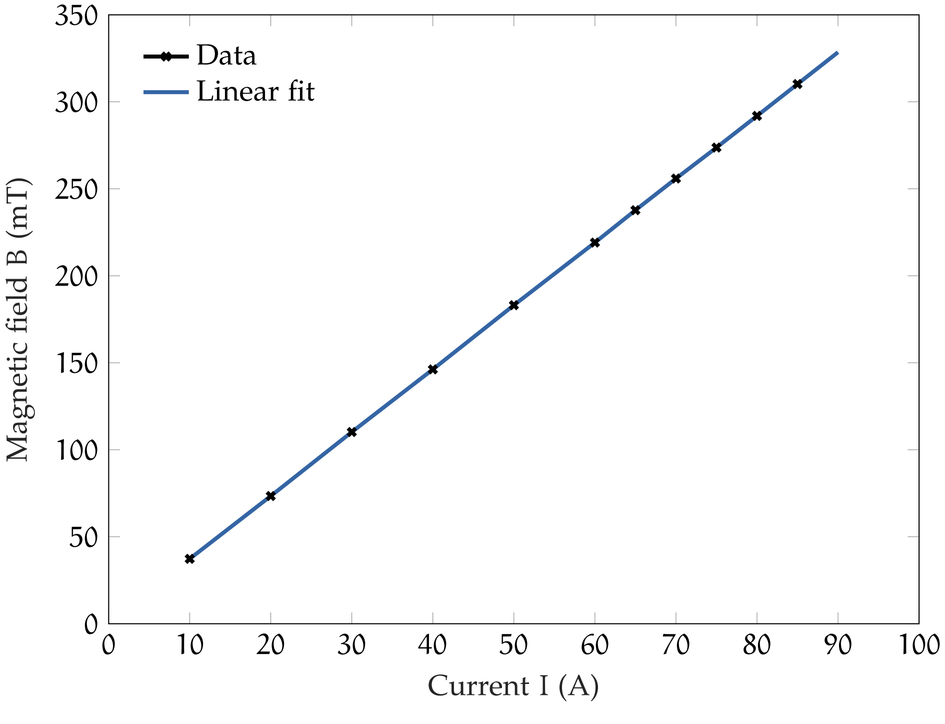

Figure 52: Response of the magnetic field at a fixed but arbitrary location inside the quadrupole to a change in current in the quadrupole coils.

The X1 beamline used for all measurement in the scope of this work can be seen in Fig. 18 in Sec. 2.1.6. The QM dublets in front of the APL were supplied by Bruker. The QM triplet after the APL and the dipole magnet were previously used in a positron system at the uni-

Table 8: Relevant parameters of the quadrupoles used in the MaMi-B beamline.

		Bruker duplets	MPI triplet
Maximum gradient	[T/m]	23.5	6.8
Effective length	[mm]	296	375
Focal length for 855 MeV	[mm]	410	1120
Aperture radius	[mm]	20	70
Maximum current	[A]	50	100

versity of Mainz and were build by MPI. They have been measured and tested in [45]. The relevant features of both types of QMs can be found in Tab. 8. The dipole in the beamline is also refurbished and is a sector dipole with a design bending angle of 30°. It is used as a 44° bending dipole, therefore introducing some edge-focusing - see Appendix A. All scans were performed in vertical direction, avoiding the dispersion introduced by the dipole. Since the energy spread of MaMi-B is on the 10^{-5}-level, very little actual beam size increase was introduced at the screen position by the dispersion. Had there been any wakefield effects, the beam size in horizontal direction would have provided some insight into the nature of these effects. Owing to the very low beam current however, no such effect was seen, as was explained in Sec. 1.2.2.

BIBLIOGRAPHY

[1] S Weinberg. A model of leptons. *Physical review letters*, 19(21):1264, 1967.

[2] U Bonse and M Hart. An x-ray interferometer. *Applied Physics Letters*, 6(8):155–156, 1965.

[3] A Momose et al. Phase–contrast x–ray computed tomography for observing biological soft tissues. *Nature medicine*, 2(4):473–475, 1996.

[4] JC Solem. Imaging biological specimens with high-intensity soft x rays. *JOSA B*, 3(11): 1551–1565, 1986.

[5] R Henderson. The potential and limitations of neutrons, electrons and x-rays for atomic resolution microscopy of unstained biological molecules. *Quarterly reviews of biophysics*, 28(2):171–193, 1995.

[6] AM Kondratenko and EL Saldin. Generating of coherent radiation by a relativistic electron beam in an ondulator. *Part. Accel.*, 10:207–216, 1980.

[7] R Neutze et al. Potential for biomolecular imaging with femtosecond x-ray pulses. *Nature*, 406(6797):752, 2000.

[8] HN Chapman et al. Femtosecond diffractive imaging with a soft-x-ray free-electron laser. *Nature Physics*, 2(12):839, 2006.

[9] S Jr. Humpries. *Charged Particle Beams*. Dover Publications, Inc., 2013.

[10] P Chen et al. Acceleration of electrons by the interaction of a bunched electron beam with a plasma. *Physical review letters*, 54(7):693, 1985.

[11] T Tajima and JM Dawson. Laser electron accelerator. *Physical Review Letters*, 43(4):267, 1979.

[12] R. Weingartner et al. Ultralow emittance electron beams from a laser-wakefield accelerator. *Phys. Rev. ST Accel. Beams*, 2012.

[13] SK Barber, Jeroen van Tilborg, CB Schroeder, Remi Lehe, H-E Tsai, KK Swanson, Sven Steinke, Kei Nakamura, CGR Geddes, Carlo Benedetti, et al. Measured emittance dependence on the injection method in laser plasma accelerators. *Physical review letters*, 119(10): 104801, 2017.

[14] K Flöttmann. Some basic features of the beam emittance. *Physical Review Special Topics-Accelerators and Beams*, 6(3):034202, 2003.

[15] S Steinke et al. Multistage coupling of independent laser-plasma accelerators. *Nature*, 530 (7589):190, 2016.

[16] H Wiedemann. *Particle Accelerator Physics*. Springer, 4th ed. edition, 2015.

[17] WKH Panofsky and WR Baker. A focusing device for the external 350-mev proton beam of the 184-inch cyclotron at berkeley. *Rev. Sci. Instrum.*, 1950.

[18] M Reiser. *Theory and Design of Charged Particle Beams*. John Wiley and Sons, 2008.

[19] J van Tilborg et al. Nonuniform discharge currents in active plasma lenses. *Physical Review Accelerators and Beams*, 20(3):032803, 2017.

[20] J-H Röckemann, L Schaper, SK Barber, NA Bobrova, G Boyle, S Bulanov, N Delbos, K Flöttmann, G Kube, W Lauth, et al. Direct measurement of focusing fields in active plasma lenses. *Physical Review Accelerators and Beams*, 21(12):122801, 2018.

[21] J.K. Lim et al. Adjustable, short focal length permanent-magnet quadrupole based electron beam final focus system. *Phys. Rev. ST Accel. Beams*, 2005.

[22] Richard D'Arcy, S Wesch, A Aschikhin, S Bohlen, C Behrens, MJ Garland, L Goldberg, P Gonzalez, A Knetsch, V Libov, et al. Tunable plasma-based energy dechirper. *Physical review letters*, 122(3):034801, 2019.

[23] M. Migliorati et al. Intrinsic normalized emittance growth in laser-driven electron accelerators. *Phys. Rev. ST Accel. Beams*, 2013.

[24] CA Lindstrøm and E Adli. Design of general apochromatic drift-quadrupole beam lines. *Physical Review Accelerators and Beams*, 19(7):071002, 2016.

[25] J Van Tilborg et al. Active plasma lensing for relativistic laser-plasma-accelerated electron beams. *Physical Review Letters*, 115(18):184802, 2015.

[26] NA Bobrova et al. Simulations of a hydrogen-filled capillary discharge waveguide. *Physical Review E*, 65(1):016407, 2001.

[27] BHP Broks, K Garloff, and JJAM Van der Mullen. Nonlocal-thermal-equilibrium model of a pulsed capillary discharge waveguide. *Physical Review E*, 71(1):016401, 2005.

[28] LC Steinhauer and WD Kimura. Quasistatic capillary discharge plasma model. *Physical Review Secial Topics - Accelerators and Beams*, 9:081301, 2006.

[29] G Bagdasorov et al. Laser beam coupling with capillary discharge plasma for laser wakefield acceleration applications. *Physics of Plasmas*, 24:083109, 2017.

[30] F. Paschen. Über die zum Funkenübergang in Luft, Wasserstoff und Kohlensäure bei verschiedenen Drucken erforderliche Potentialdifferenz. *Annalen der Physik*, 273(5):69–96, 1889.

[31] CA Lindstrøm, , and E Adli. Analytic plasma wakefield limits for active plasma lenses. *arXiv*, 2018. URL `https://arxiv.org/pdf/1802.02750.pdf`.

[32] CA Lindstrøm et al. Overview of the clear plasma lens experiment. *NIM A*, 2018. ISSN 0168-9002. doi: https://doi.org/10.1016/j.nima.2018.01.063. URL `https://www.sciencedirect.com/science/article/pii/S0168900218300809`.

[33] P Chen et al. Plasma-based adiabatic focuser. *Physical Review Letters*, 64(11):1231–1234, 1990.

[34] T Mehrling. *Theoretical and Numerical Studies on the Transport of Transverse Beam Quality in Plasma-Based Accelerators*. PhD thesis, Universität Hamburg, 2014.

[35] JB Rosenzweig, B Breizman, T Katsouleas, and JJ Su. Acceleration and focusing of electrons in two-dimensional nonlinear plasma wake fields. *Physical Review A*, 44(10):R6189, 1991.

[36] K Flöttmann. Adiabatic matching section for plasma accelerated beams. *Physical Review Special Topics-Accelerators and Beams*, 17(5):054402, 2014.

[37] MJ Hogan et al. Ultrarelativistic-positron-beam transport through meter-scale plasmas. *Physical review letters*, 90(20):205002, 2003.

[38] JB Rosenzweig, F Filippi, A Zigler, MP Anania, G Andonian, A Biagioni, E Chiadroni, A Cianchi, A Deng, M Ferrario, et al. Adiabatic plasma lens experiments at sparc. *Nuclear Instruments and Methods in Physics Research Section A: Accelerators, Spectrometers, Detectors and Associated Equipment*, 2018.

[39] M Touati et al. A reduced model for relativistic electron beam transport in solids and dense plasmas. *New Journal of Physics*, 16(7):073014, 2014.

[40] BW Montague and W Schnell. Multiple scattering and synchrotron radiation in the plasma beat-wave accelerator. In *AIP Conference Proceedings*, volume 130, pages 146–155. AIP, 1985.

[41] T Wachler. The mainz microtron facility mami. *Progress in Particle and Nuclear Physics*, 24: 189–203, 1990.

[42] NM Delbos. *High Repetition Rate Laser-Plasma Accelerator: 5 Hz Electron Beam Generation and Advanced Target Design*. PhD thesis, Universität Hamburg, 2017.

[43] R John. Pulse forming network, September 15 1959. US Patent 2,904,706.

[44] L Goldberg. Laser-based discharge ignition for capillary waveguides. Master's thesis, Universität Hamburg, 2013.

[45] F Hagenbuck. *Entwicklung eines neuartigen bildgebenden Verfahrens zur digitalen Subtraktionsradiographie mit Übergangsstrahlung am Mainzer Mikrotron MAMI*. PhD thesis, Universität Mainz, 2001.

[46] CA Lindstrøm, E Adli, G Boyle, R Corsini, AE Dyson, W Farabolini, SM Hooker, M Meisel, J Osterhoff, J-H Röckemann, et al. Emittance preservation in an aberration-free active plasma lens. *Physical Review Letters*, 121(19):194801, 2018.

[47] S Becker et al. Characterization and tuning of ultrahigh gradient permanent magnet quadrupoles. *Physical Review Special Topics-Accelerators and Beams*, 12(10):102801, 2009.

[48] H Alfvén. Existence of electromagnetic-hydrodynamic waves. *Nature*, 150:405–406, 1942.

[49] A Butler, DJ Spence, and SM Hooker. Guiding of high-intensity laser pulses with a hydrogen-filled capillary discharge waveguide. *Physical Review Letters*, 89(18):185003, 2002.

[50] NA Bobrova and et al. Laser-heater assisted plasma channel formation in capillary discharge waveguides. *Physics of Plasmas*, 20(2):020703, 2013.

[51] K Flöttmann. Astra particle tracking code. *www.desy.de/ mpyflo*, 2018.

[52] R D'Arcy, A Aschikhin, S Bohlen, G Boyle, T Brümmer, J Chappell, S Diederichs, B Foster, MJ Garland, L Goldberg, et al. Flashforward: plasma wakefield accelerator science for high-average-power applications. *Philosophical Transactions of the Royal Society A*, 377(2151): 20180392, 2019.

[53] Hrvoje Jasak, Aleksandar Jemcov, Zeljko Tukovic, et al. Openfoam: A c++ library for complex physics simulations. In *International workshop on coupled methods in numerical dynamics*, volume 1000, pages 1–20. IUC Dubrovnik Croatia, 2007.

[54] J Roßbach and P Schmüser. *Basic course on accelerator optics*. DESY internal report M-93-02, 1993. Lecture given at the CERN Accelerator School.

EIDESSTATTLICHE ERKLÄRUNG DER SELBSTSTÄNDIGKEIT

Hiermit versichere ich an Eides statt, die vorliegende Dissertationsschrift selbst verfasst und keine anderen als die angegebenen Hilfsmittel und Quellen benutzt zu haben.

Die Dissertation wurde in der vorgelegten oder einer ähnlichen Form nicht schon einmal in einem früheren Promotionsverfahren angenommen oder als ungenügend beurteilt.

Die eingereichte schriftliche Fassung entspricht der auf dem elektronischen Speichermedium.

Hamburg, den 14.01.2020

Jan-Hendrik Röckemann